CHAPTER 8. RESERVOIR COMMUNICATION

Alan P. Byrnes, Martin K. Dubois, Saibal Bhattacharya, and Robert E. Barba

Fundamental to modeling Hugoton gas production is an understanding of the relative contribution of lithofacies/beds within defined productive intervals and of the nature of communication between intervals. Section 8.1 examines the scaling of petrophysical properties from the core plug to well scale and the validity of using matrix-scale properties equations for predicting well-scale properties. Section 8.2 analyzes the potential influence of thin high-permeability beds on gas production, the influence of vertical permeability on crossflow. Pressure evidence for communication between the Chase and Council Grove at local and regional scales is presented in Section 8.3 and simulations analyzing gas production and pressure depletion in Hugoton reservoir models is presented in Section 8.4. Finally, Section 8.5 presents the results of a study investigating simulation of typical Hugoton hydraulic-fracture treatments and the nature of the fractures developed.

8.1. CORE- to WELL- SCALING

Alan P. Byrnes

Correlation of core plug to full-diameter core properties can be influenced by scale due to the potential measurement of pseudo-properties at progressively larger scales as different smaller-scale properties are averaged. This occurs most notably for porosity and permeability. Wireline-density logs, full-diameter core, and routine core plugs measure volumes of approximately 250, 100, and 2 in^3, respectively. Where rocks are homogeneous these measurements provide the same values, but heterogeneity can, obviously, result in differences that vary with the scale of the heterogeneity.

For many Hugoton cores there is sufficient homogeneity over a vertical scale of ~4 inches that full-diameter and plug porosity analyses agree. Comparison of both porosity measures for the Anadarko Flower A-1 core (Figure 8.1.1) shows that this core is homogeneous at the full-diameter scale. Homogeneity should also result in similarity of flow properties, and Figure 8.1.2 shows that full-diameter and plug routine air permeability measurements are also highly correlated. The presence of a few outliers exhibiting significantly higher permeability than the corresponding plugs may indicate either the presence of a fracture or microfracture or the presence of vertical heterogeneity such that the full-diameter analysis represented flow from multiple layers of different properties. The sample exhibiting a full-diameter permeability of 3.3 md and plug permeability of 0.06 md also exhibited full-diameter and plug porosity of 10.9% and 7.1%, respectively. Comparison of the permeability versus porosity trends for the full-diameter and plug data also indicates that both scales exhibit a similar trend (Figure 8.1.3).

Although homogeneous full-diameter and core plug porosities and permeabilities agree, natural bedding can create vertical heterogeneity that can influence properties. If porosity varies among beds, within a full-diameter core the routine helium porosity measured represents an accurate volumetric average of the individual porosities. Because of the architecture of permeability, elements can exert significant influence on the average permeability of the system; at larger scales the nature of full-diameter orientation and core-plug sampling can be important to results. For the full-diameter core clearly when there is bedding the orientation of the core relative to the direction of flow can have a major influence. It is for this reason that full-diameter permeability is often measured in two orthogonal directions and reported as Kmax and K90. For plugs it is usually considered appropriate to obtain samples parallel to bedding and not perpendicular to bedding. A question arises, however, for plugs obtained parallel to bedding but that sample beds of different property. Whatever the orientation of the full-diameter or plug to flow, the resulting permeability data must always be analyzed with respect to the total flow system and at larger scales to evaluate the role of architecture.

A simple example illustrates how differences in core rock properties in a single sample can influence interpretation. Assume we are measuring the permeability of a sample for which we know the matrix permeability is correlated to porosity using the equation for a mudstone/wackestone limestone: $k = 1.15\text{x}10^{-9}\ \phi^{7.61}$ (lithofacies L5; Table 4.2.6). Assume the core comprises two beds of which bed_1 represents 30% of the core and bed_2 represents the remaining 70% of the core. Assume bed_2 porosity ϕ = 10%, the corresponding permeability is 0.047 md permeability. Ranging the possible porosities of the upper layer between 0% porosity and 24% porosity then the permeability of the upper bed ranges from $1.1 \text{ x } 10^{-9}$ to 36.6 md. The average porosity for the core, as it would be measured, is simply the arithmetic average based on the relative volumes (i.e. $\phi_{avg} = 0.7\text{x}10\% + 0.3 \text{ x } \phi_{bed1}$). For a parallel flow architecture average permeability is calculated by calculating the arithmetic average of the permeabilities (and not the geometric average which is the average of logarithm of the permeabilities). Because the two beds are parallel, the measured permeability would be the arithmetic average of the permeability of the upper bed and the permeability of the lower bed ignoring crossflow issues. However, if we calculate the permeability from the average porosity using the permeability-porosity equation above, which we know applies to the matrix, we obtain a very different value than the measured value (Table 8.1.1). The difference between the measured and calculated permeabilities results from the disparity between the arithmetic averaging of linearly distributed porosity and logarithmically distributed permeability. Only when the upper and lower beds have the same properties or when permeability is linearly correlated with porosity do the measured and calculated permeability agree. Examining the nature of the difference in Figure 8.1.4, the ratio of the "measured" permeability (which is known to be correct because the matrix properties and the flow architecture are defined) to the calculated permeability is always great than 1 except when the core is homogeneous and the measured and calculated permeability agree.

Given a measured full-diameter porosity, the permeability measured is not a unique solution of bed properties. Table 8.1.2 shows example combinations of beds of different porosity and fraction of the total core that all exhibit an average porosity of 10%. The permeabilities for these combinations range from 1X the matrix-based permeability to 100X. This range of uncertainty represents one of the contributions to variance in permeability-porosity correlations.

Form the discussion above, it is apparent that full-diameter permeability-porosity trends must exhibit higher permeability at a given porosity than a plug trend except where 1) the core is homogeneous at the full-diameter core scale, and 2) permeability is linearly correlated with porosity. In the Hugoton cores the degree of vertical heterogeneity in full-diameter core samples is not known, but it is likely that a significant fraction of full-diameter cores exhibit some degree of heterogeneity and therefore would have higher permeability at a given porosity than the plug or matrix trends developed. Without knowing the nature of the heterogeneity, these same principles apply to any scale of investigation. If porosity is averaged over an entire interval in a drill stem test (DST) analysis, the measured DST will exhibit a higher permeability than would be calculated from the average porosity.

Chapter 4.2 discussed the influence of confining stress on porosity and permeability. The relationships developed between in situ and routine properties were developed using core-plug data. The application of these equations to full-diameter core is also influenced by the multiple-bed averaging issue discussed above. Because the influence of confining stress generally increases with decreasing permeability, if a core represents multiple permeabilities, the influence of confining stress would differ for each of the beds in the core and the final property would represent a combination of the stress effects.

In addition to heterogeneity issues, full-diameter core are subject to the influence of natural and coring-induced fractures. A permeability-porosity crossplot of full-diameter and plug data (Figure 8.1.5) shows the significant influence that fracturing and microfracturing can have on measured routine air permeability. Given that a single hairline crack can exhibit permeability in a full-diameter core of $k = 0.1$ to 0.5 md, the presence of microfractures is important in full-diameter analysis.

The correspondence of plug and full-diameter permeability illustrated in Figures 8.1.2 and 8.1.3 can be interpreted to indicate that matrix properties dominate flow at the scale of full-diameter core. The question remains do upscaled matrix permeability values accurately represent flow at the well scale. To answer this question upscaled full-diameter measured core permeabilities were compared with drillstem test (DST) measured permeabilities. To upscale full-diameter permeability values it was assumed that flow was parallel into the well and therefore horizontal permeability values were arithmetically averaged. The average of the Kmax and K90 permeability values were averaged for the interval over which a DST was measured. Air permeability values were corrected for confining stress effects using equation 4.2.7 and an approximate relative permeability correction factor of $k_{rg} = 0.9$ to obtain an *in situ* effective-gas Klinkenberg-gas permeability. This permeability corresponds to the conditions measured by a DST. Figure 8.1.6 illustrates the correlation between upscaled core permeability values and DST-measured permeabilities. These two measures of permeability exhibit a high correlation for permeabilities greater than $k = 0.5$ md. Below this permeability the averaged full-diameter permeability values are significantly greater than DST-measured values. This difference is interpreted to result from measured high permeabilities in low-permeability full-diameter core due to microfracturing in the core that does not exist in the subsurface. Also shown in Figure 8.1.6 is the correlation of model-predicted permeabilities and measured-DST permeabilities. The model-predicted permeabilities were obtained from arithmetic averaging of permeabilities predicted from core porosities using the equation discussed in Chapter 4. These permeabilities exhibit better correlation for permeability below *k* = 0.5 md. A single interval for which permeability is significantly under-predicted by the model is a phylloid-algal boundstone interval where the issue of the wide variability of permeability in this lithofacies resulting from touching and non-touching phylloid vugs is evident. The model-predicted permeabilities are also under-predicted in intervals with high moldic porosity.

Routine full-diameter permeability data require correction for confining stress, Klinkenberg gas slippage effect, relative permeability, and appropriate upscaling to correspond to DST-measured permeabilities. In Figure 8.1.7 full-diameter permeabilities corrected to these effects are compared with DST-measured values in four research wells where the wells were air/foam drilled and DST's were allowed to flow until equilibrium pressure was accurately projected. In these wells, the correlation between upscaled core-measured and DST-measured permeabilities is good for *k* > ~0.5 md and is progressively poorer as permeability decreases below *k* = ~0.5 md. As noted above, this is interpreted as resulting from microfractures in the full-diameter core that are not present in the subsurface. The close correspondence between the DST- and core-measured permeabilities is interpreted to indicate that matrix-scale properties dominate flow behavior at the well scale and that is these wells fractures do not exert a significant influence.

It is important to note that although thes wells examined here exhibit matrix-driven properties, fractures are present in the Hugoton. At any given location in the Hugoton flow may be characterized as: 1) matrix-controlled, 2) locally matrix-controlled but regionally controlled by fractures, 3) locally matrix-controlled with random small-scale fractures that may influence flow in some beds, and 4) fracture-controlled (Figure 8.1.8).

Lithofacies Code	General Lithology Lithologic Description	*In situ* Klinkenberg Permeability Equation Parameter A	*In situ* Klinkenberg Permeability Equation Parameter B	Permeability Standard Error of Prediction Factor (factor)
0	Continental vf-fn Sandstone	1.318E-08	6.65	2.9
1	Continental crs Siltstone	1.096E-10	8.00	9.3
2	Continental fn-med Siltstone	8.913E-11	8.00	15.6
3	Marine Shale/Siltstone	3.890E-10	7.74	9.2
4	Mudstone/Mud-wackestone Limestone	1.585E-11	9.20	16.0
5	Wackestone/Wacke-packstone Limestone	1.148E-09	7.61	7.5
6	vf-fn Sucrosic Dolomite	1.585E-12	9.70	5.3
7	Packstone/Grainstone Limestone	1.549E-08	7.09	4.0
8	Phylloid Algal Bafflestone	5.129E-09	8.65	5.4
9	med Sucrosic Moldic Dolomite	1.585E-11	9.70	6.7
10	Marine vf-fn Sandstone	2.399E-12	9.75	3.5

Table 8.1.1. Equation parameters for predicting *in situ* Klinkenberg permeability from *in situ* porosity for each lithofacies. Parameters are used in equation of form:

$$k_{ik} = A\,\phi_i^{\,B}$$

where k_{ik} is in millidarcies (md), porosity is in percent (%). Standard error of prediction factors are also presented (e.g. for a SE = 4X, predicted k_{ik} = 1 md has first standard deviation range of k_{ik} = 4 md or k_{ik} = 0.25 md).

Table 8.1.2. Comparison of measured and calculated permeability for a core with two beds. The solution for an average porosity of 10% is non-unique and a large combination of bed porosities and fractions exhibit the same average porosity but exhibit measured permeabilities that range from 1X to 100X the matrix properties calculated value. Permeability is known to be that of the mudstone/wackestone limestone; $k = 1.15\text{x}10^{-9}\ \phi^{7.61}$ (lithofacies L5; Table 4.2.6). Measured permeability is here calculated from the above equation using arithmetic averaging of permeability because the beds are flowing in parallel. Calculated permeability of average porosity of core is always less than the measured permeability due to correct arithmetic averaging of porosity but incorrect assumption that permeability varies linearly with porosity.

Upper Layer Porosity (%)	Base Layer Porosity (%)	Porosity Difference (%)	Upper Layer Fraction	Upper Layer Permeability (md)	Base Layer Permeability (md)	Average Porosity (%)	Calculated Permeability at Average Porosity (md)	Measured Permeability (md)	Ratio Measured/ Composite Permeability
2.0	13.4	11.4	0.3	0.00000022	0.441	10.0	0.047	0.309	6.6
4.0	12.6	8.6	0.3	0.00004381	0.267	10.0	0.047	0.187	4.0
6.0	11.7	5.7	0.3	0.000959	0.156	10.0	0.047	0.109	2.3
8.0	10.9	2.9	0.3	0.00856	0.087	10.0	0.047	0.064	1.4
10.0	10.0	0.0	0.3	0.0468	0.047	10.0	0.047	0.047	1.0
12.0	9.8	-2.2	0.1	0.187	0.039	10.0	0.047	0.054	1.2
14.0	9.0	-5.0	0.2	0.61	0.021	10.0	0.047	0.138	2.9
16.0	6.0	-10.0	0.4	1.67	0.001	10.0	0.047	0.669	14.3
18.0	2.0	-16.0	0.5	4.10	0.000	10.0	0.047	2.049	43.8
20.0	0.0	-20.0	0.5	9.14	0.000	10.0	0.047	4.568	97.7

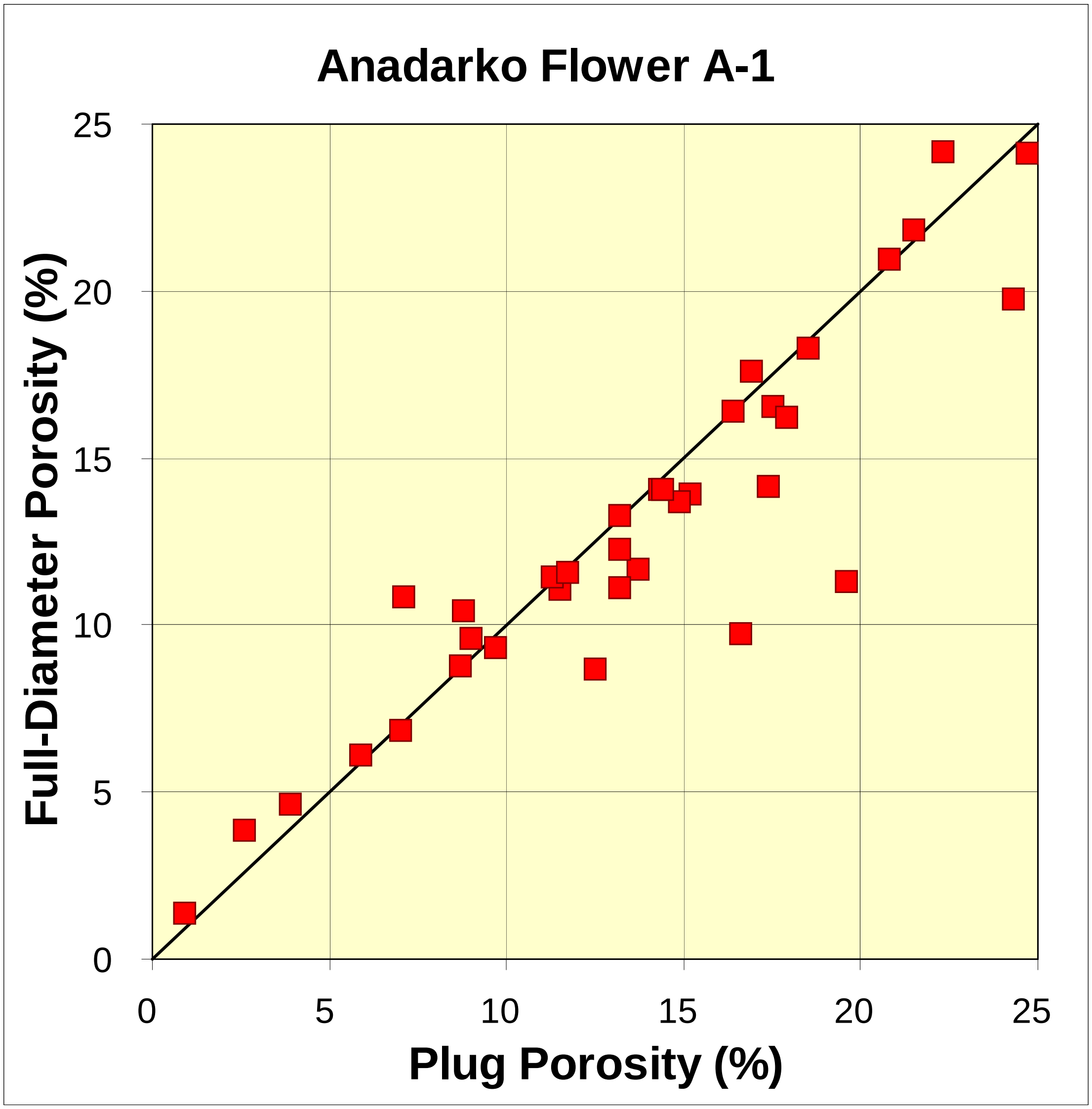

Figure 8.1.1 Crossplot of full-diameter routine helium porosity versus core-plug routine helium porosity for a core from the Anadarko Flower A-1. High correlation indicates that the rock is homogeneous at the full-diameter scale.

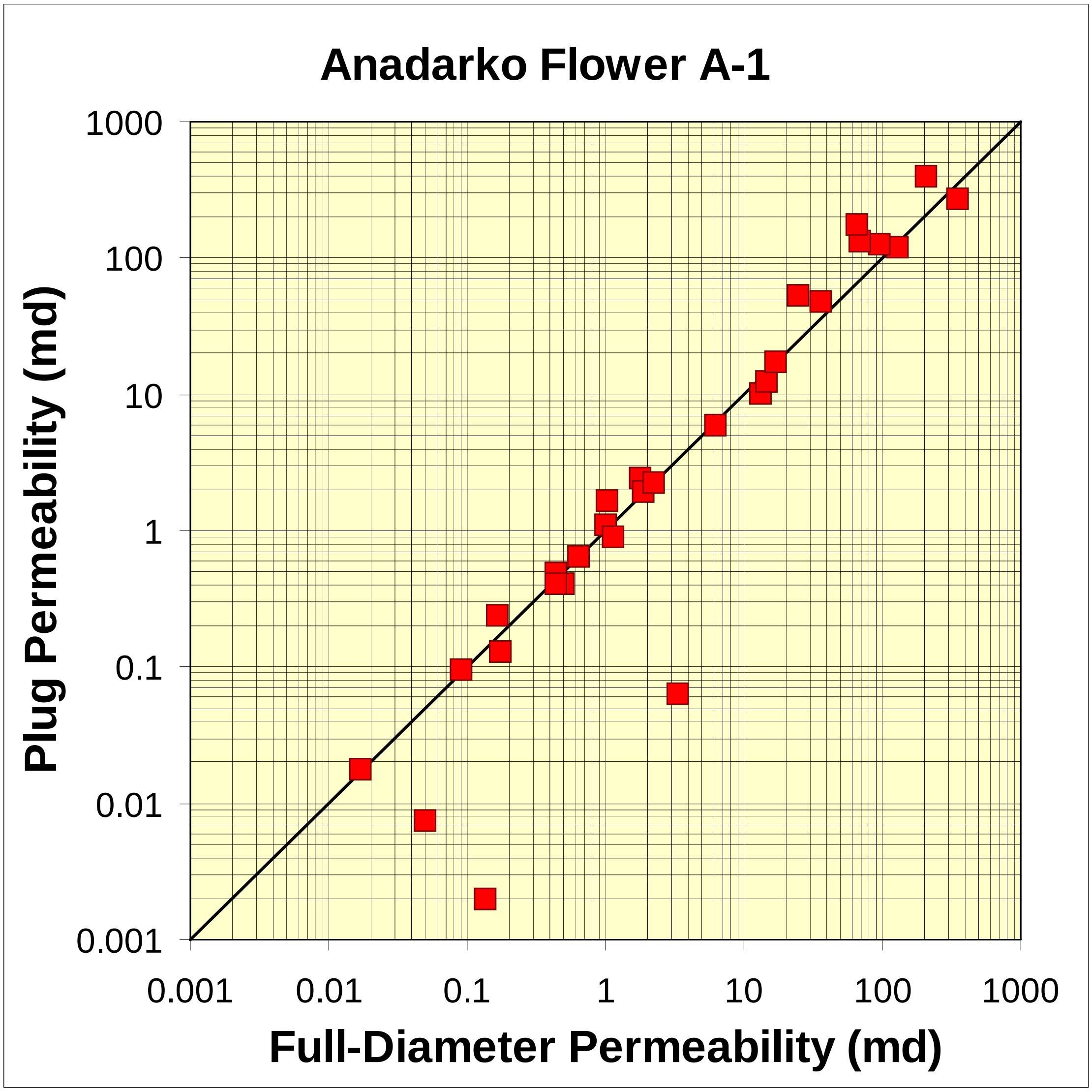

Figure 8.1.2 Crossplot of full-diameter permeability versus core-plug permeability for a core from the Anadarko Flower A-1. High correlation indicates that the rock is homogeneous at the full-diameter scale.

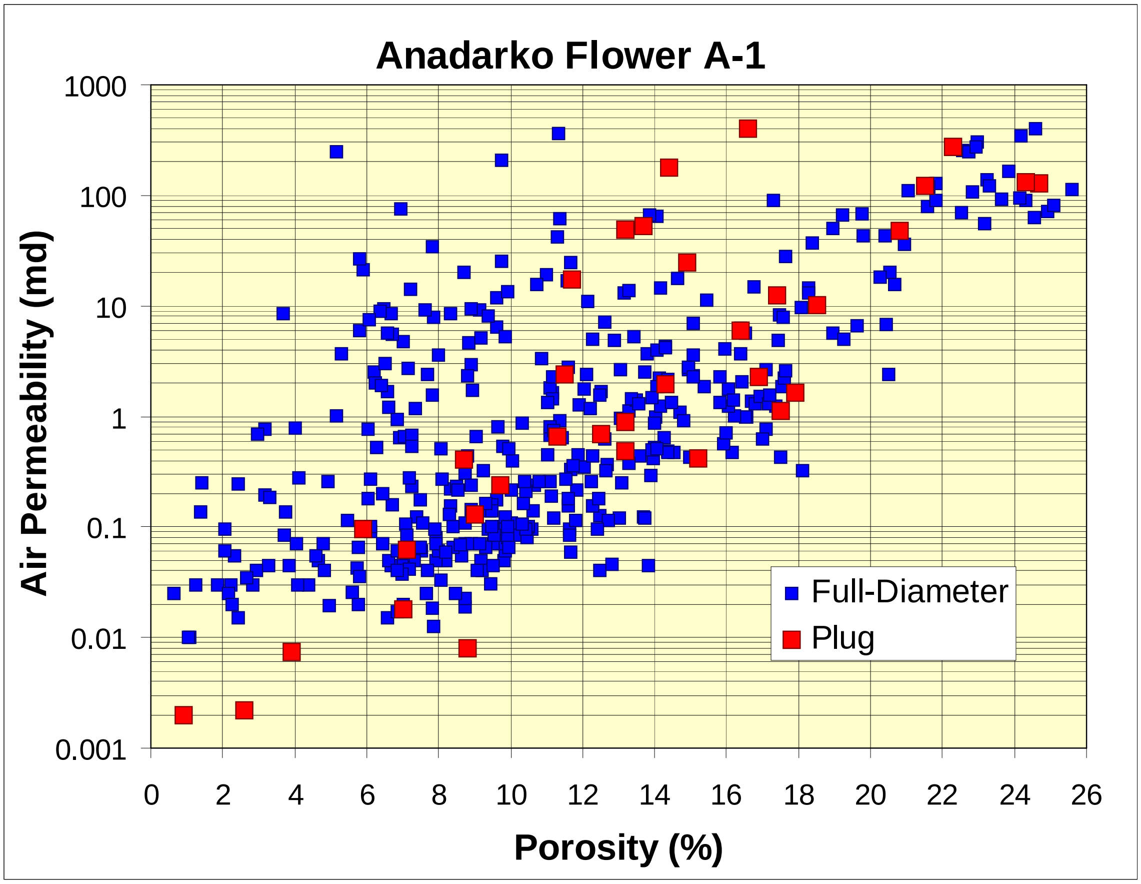

Figure 8.1.3 Crossplot of full-diameter and plug routine air permeability versus routine helium porosity for core from the Anadarko Flower A-1. Both scales of measurement exhibit a similar trend except that both the full-diameter and plug trends have outliers exhibiting higher permeability than the principal populations. These cores may have had fractures.

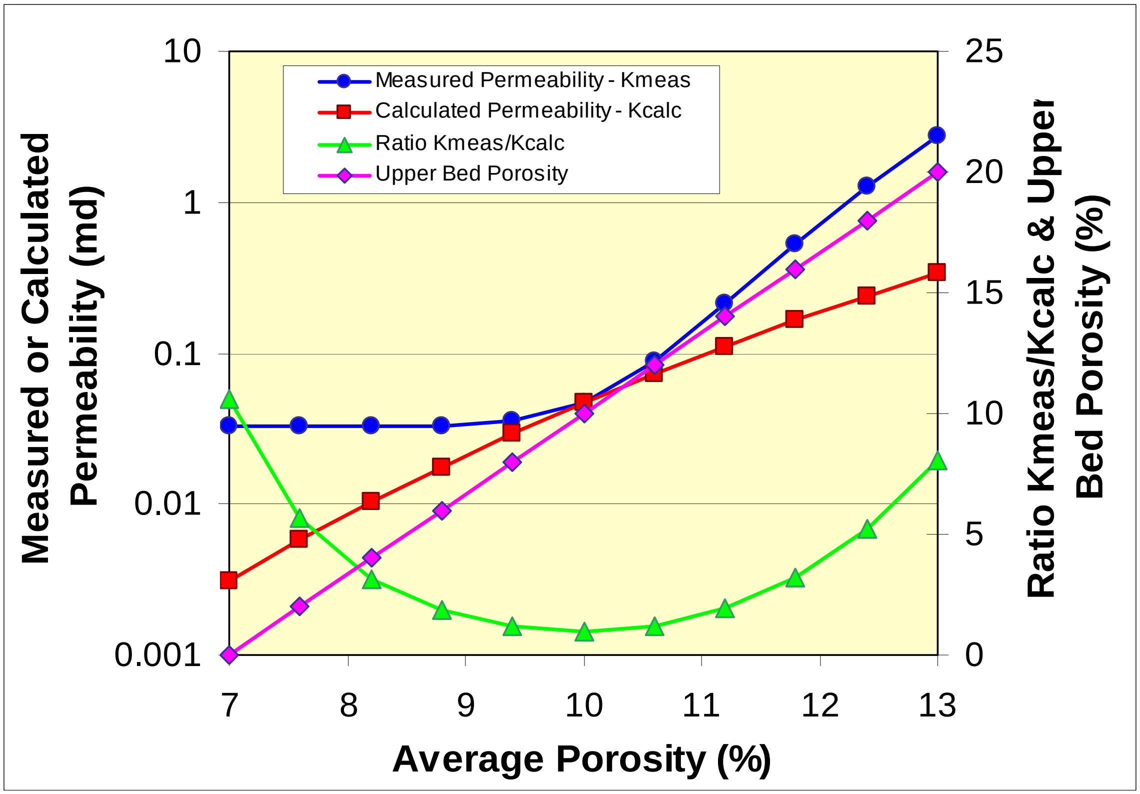

Figure 8.1.4. Crossplot showing relationships of core properties when two beds comprising 30% and 70% of a full-diameter core have porosity and permeability measured as summarized in Table 8.1.1. Ratio K_{meas}/K_{calc} is the ratio of the measured permeability and the permeability calculated from the measured porosity (which is an average of a ϕ=10% bed representing 70% of the sample and the upper bed having the porosities shown (magenta line)). The ratio K_{meas}/K_{calc} shows that no matter what the nature of the bed_2 porosity, the measured permeability in a rock having beds of two different porosities is always greater than what would be calculated from the matrix-based permeability-porosity relationship when permeability and porosity are not linearly correlated. When bed_2 and bed_1 have the same porosity, the sample is homogeneous and the measured and calculated permeabilities agree.

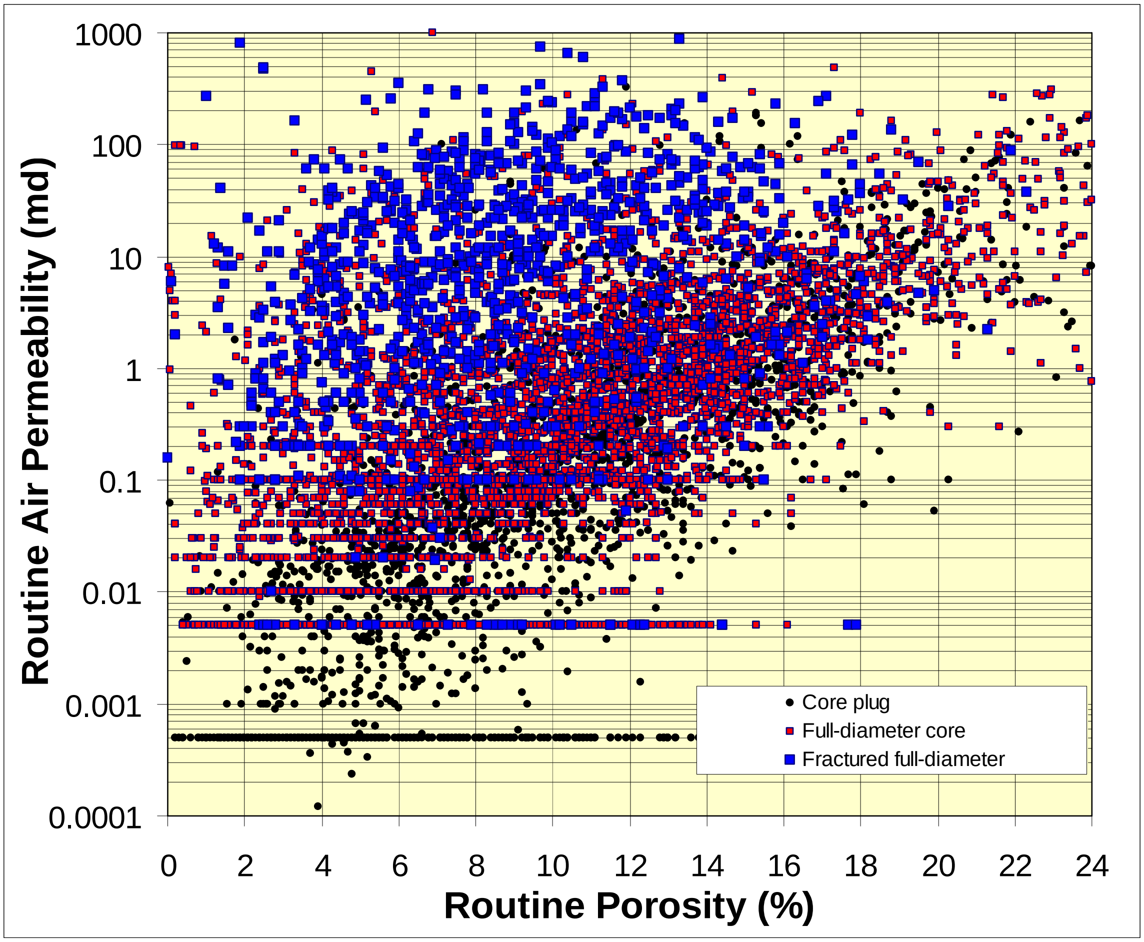

Figure 8.1.5 Crossplot of routine air permeability versus porosity for full-diameter cores where fractures were noted, for the remaining fraction of full-diameter cores in which fractures were not noted but may have been present, and core plugs. Samples with permeability identified as “k<0.1 md” were assigned k=0.05 md and samples with permeability identified as “k< 0.01 md” were assigned a value of k=0.005 md. Full-diameter core values begin to diverge from matrix (plug) values at porosities less than ~10% and matrix permeability of ~0.5 md, reflecting the influence of microfracture(s) on permeability in whole core samples with porosity < 10%. Above 10 % porosity, influence of microfractures(s) is small.

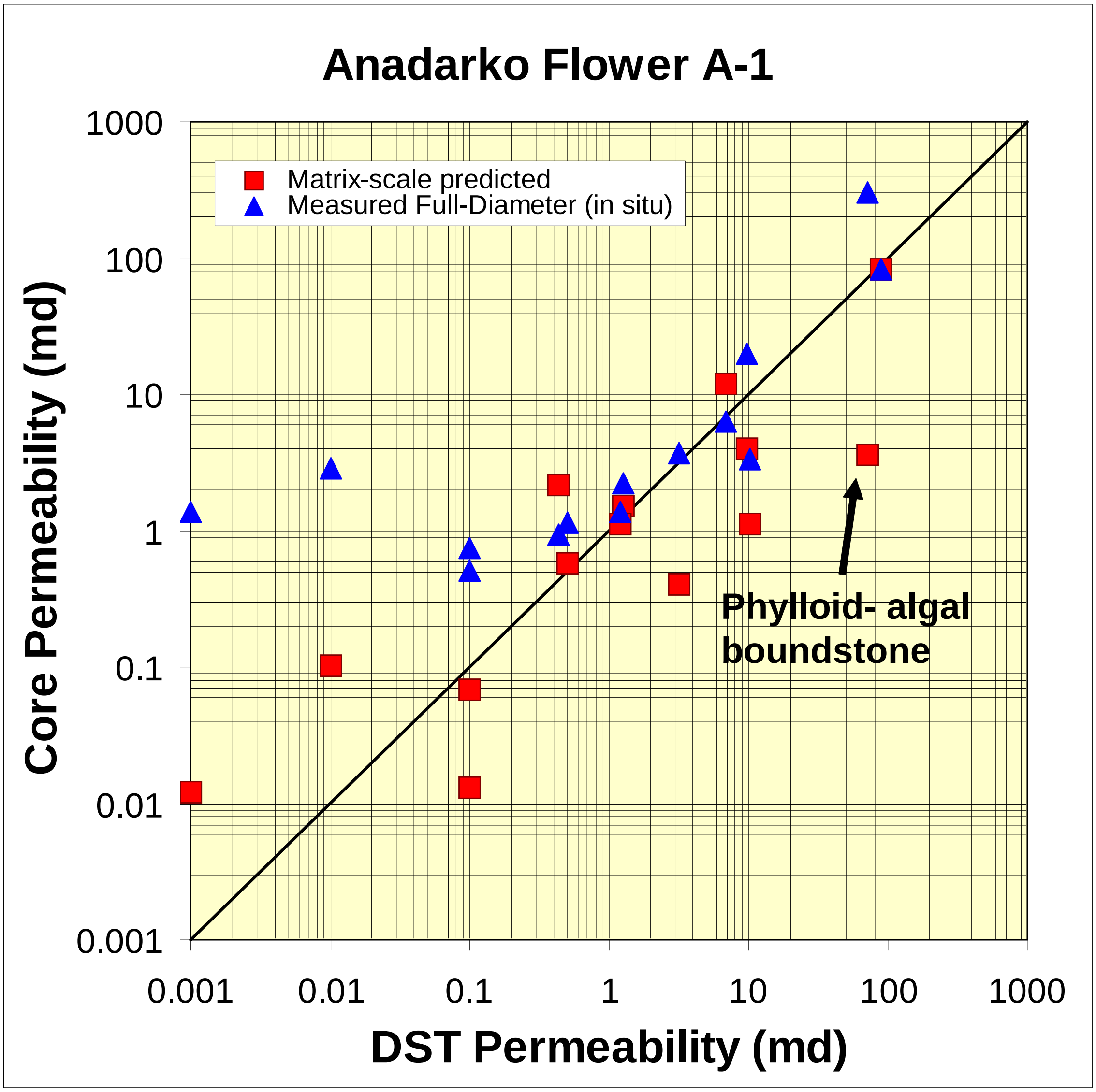

Figure 8.1.6 Crossplot of drillstem test (DST) permeability versus core-matrix permeability for Anadarko Flower A-1 well. Core-measured permeability (blue diamond) represents arithmetic average of full-diameter air permeabilities corrected for confining stress. Correlation is good for intervals with k > ~0.5 md. Poor correlation below k = 0.5 md is interpreted as due to high permeabilities of core permeability values with microfracturing in core. Red squares represent model predicted permeabilities derived from model permeability-porosity equations discussed in Chapter 4.2.

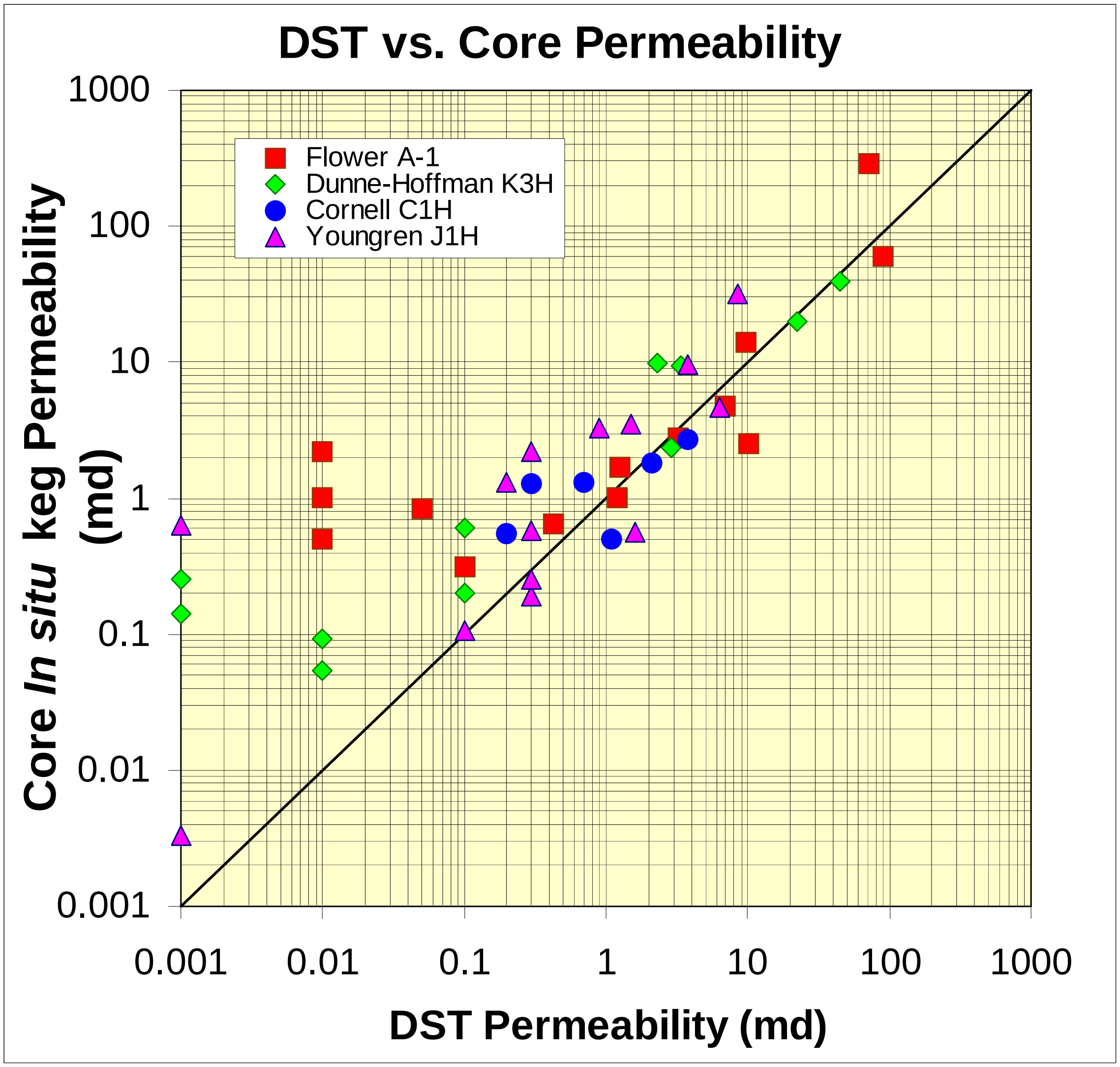

Figure 8.1.7 Crossplot of drillstem test (DST) measured permeability versus core-measured effective *in situ* Klinkenberg-gas permeability for several test wells. Core permeability represents arithmetic average of full-diameter air permeabilities corrected for confining stress, Klinkenberg gas-slippage effect, and relative permeability. Correlation is good for intervals with k > ~0.5 md. Poor correlation below k = 0.5 md is interpreted to be due to high permeabilities of core permeability values resulting from microfractures dominating flow in low-permeability core.

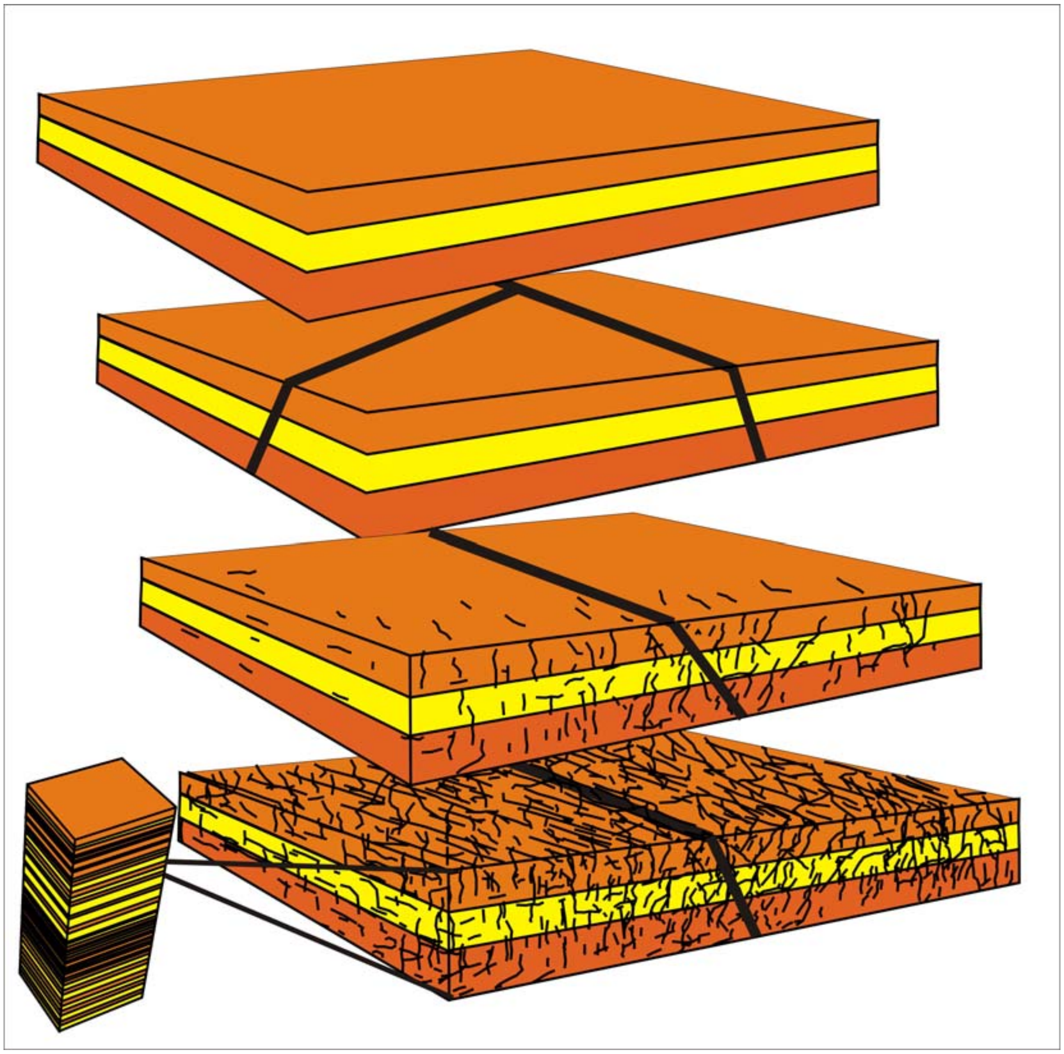

Figure 8.1.8 Permeability models for the Hugoton showing various matrix-fracture scenarios. At any given location in the Hugoton one of these scenarios may apply. Data for many wells support a strongly matrix-controlled system for well production but large-scale pressure equilibration argues for local matrix-control with large-scale fracture control. Four models are shown: 1) Matrix-controlled: well performance and field pressure history consistent with matrix properties; 2) Local matrix-control/Large-scale fractures: well performance consistent with matrix properties, field pressure history indicates large-scale communication; 3) Local matrix-control/random small-scale fracture/large-scale fractures: well performance consistent with matrix properties in some beds and fracture influence in others, field pressure history indicates large-scale communication; 4) Fracture-control: well performance and field pressure history inconsistent with matrix properties, field pressure history indicates large-scale communication.

8.2. POTENITAL INFLUENCE OF THIN HIGH-PERMEABILITY BEDS AND CROSSFLOW

Alan P. Byrnes

Simple flow analysis and low-permeability reservoir studies (e.g., Castle and Byrnes, 1998; Byrnes, 2005) have noted that a small fraction of high-permeability beds can represent the major portion of the cumulative flow capacity from a low-permeability gas interval. Higher porosity and permeability beds can represent over 70% to 90% of the flow capacity, can hold an important portion of the recoverable hydrocarbon storage capacity, and can be considered carrier beds for draining the rest of the lower-permeability portion of the reservoir.

A key question in assessing low-permeability reservoirs is the distribution of permeability. Assumptions or models of permeability architecture are fundamental to how permeability is modeled and upscaled from finer-scale measurements. Flow in all rock systems can be characterized with respect to the fundamental end-member elements of parallel-, series-, random- and crossflow (Figure 8.2.1). Warren and Price (1961) showed, using Monte Carlo simulations, that the most probable behavior of a heterogeneous system approximately approaches that of a homogeneous system with permeability equal to the geometric mean of the individual permeabilities. Frequently, in low-permeability rocks, core- and log- analysis-derived permeabilities are averaged geometrically to obtain an effective average *k*. Use of the geometric mean *k* assumes an approximately random distribution of the measured permeabilities. Given the bed architecture in the Hugoton and that the drainage radius of many low-permeability reservoir intervals may range from 20 to 40 acres, assumption of a random-permeability distribution may not be consistent with the depositional environments. Rather, it is possible these reservoirs are likely to exhibit lateral continuity of lithofacies over many hundreds of feet. On this basis, average permeability should be calculated using the arithmetic-average equation consistent with a parallel-flow model. Using this approach, thin, high-permeability beds result in a significant increase in average permeability.

Three principal mechanisms exist for improved recovery from low-permeability intervals: 1) hydraulic-fracture stimulation; 2) the presence of natural fractures; and 3) the presence of thin, laterally extensive, high-permeability beds. The role of thin, higher-permeability beds in gas producibility is examined here using reservoir simulation. This analysis focuses on parametric analysis examining the influence of different thin-bed horizontal permeability bed properties, reservoir vertical permeability, and the influence of a hydraulic fracture in these systems. This does not represent a complete parametric analysis but illustrates trends and relative influence of variables.

A simple layer model was constructed using the Computer Modeling Group (CMG) *IMEX* reservoir simulator. The radial model comprised thirteen layers with total thickness of 500 ft and measuring 1 mile on a side with a single well in the center (Figure 8.2.2). In all models a single laterally extensive 1-ft-thick bed existed in the vertical center of the model. Porosity was assigned a uniform value of 10%. Permeability of the reservoir outside the 1-ft-thick bed was assigned k = 0.01 md. Water saturation was assigned a value of Sw = 0.4 which, using the gas-relative-permeability equations, resulted in a gas-relative permeability of k_{rg} = 0.27 and an effective gas permeability, $k_{eg,Sw}$ = 0.0027 md. Vertical effective gas permeability was assigned a range of values as discussed below. All models were assigned a reservoir pressure of 450 psi and a well-bottomhole flowing pressure of 50 psi.

For all models with the thin-bed permeability less than ~10 md, flow is still transient (i.e., pressure transient has not reached the reservoir boundary). Recovery from the 10-md reservoir begins to decline after 10 years due to the pressure decline reaching the model boundary (i.e., semi-steady state flow). Reservoirs with permeability equal to 100 md begin semi-steady state flow within 2 years.

The influence of a single 1-foot-thick higher permeability bed on cumulative gas production and gas rate from a reservoir with horizontal permeability of 0.01 md and vertical permeability of 0.001 md is shown in Figure 8.2.3. The contribution of the individual, 1-ft-thick, high-permeability beds to recovery can be seen in Figure 8.2.4. Though the gas produced by the 1-ft intervals is significant, the role that a single high-permeability bed plays in draining vertically adjacent low-permeability beds is evident. For the cases where the thin bed has a permeability of 0.01-0.1 md (with the adjacent reservoir k = 0.01 md), recovery is the same as a uniform 0.01-md reservoir. Recovery increases with increasing permeability of the thin bed. Greater recovery with increasing thin-bed permeability is due to an increase in the ability of the bed to drain vertically adjacent reservoir and carry the gas to the wellbore.

From these results it can be interpreted that the presence of a single, 1-ft-thick, high-permeability bed effectively drains overlying and underlying beds and that the radius of influence is controlled by the thin-bed permeability and its ability to transport gas from vertically adjacent intervals to the wellbore. Gas is supplied first vertically, and with increasing thin-bed permeability and/or decreasing reservoir thickness, the drainage radius expands at a greater rate. The uniformity of the vertical-pressure profiles would indicate that while some gas may flow laterally to the wellbore in the near-wellbore region, the majority of the gas flow occurs vertically to the high-permeability bed and horizontally through this bed to the wellbore.

For the vertical permeabilities present in the models shown (k_v = 0.001 md), the primary rate-limiting constraint is the thin-bed permeability. However, the ability of gas to flow vertically to the high-permeability thin bed is controlled by vertical permeability (k_v). Figure 8.2.5 shows the dependence of cumulative gas on the vertical permeability for a reservoir with 0.01 md and a 1-ft-thick bed of 100 md, and Figure 8.2.6 shows the ratio of cumulative recovery through time for various k_v. Increase in k_v greater than $1x10^{-3}$ md does not significantly increase recovery over that obtained at $k_v = 1x10^{-2}$ md. With k_v decrease below $1x10^{-3}$ md, recovery decreases with decreasing vertical permeability down to $1x10^{-7}$ md. For k_v below approximately $1x10^{-7}$ md, recovery is similar to recovery for vertical permeability equal to zero. That is, there is no significant crossflow and no vertical drainage to the high-permeability thin bed. The relative influence of k_v on cumulative gas recovery changes through time. In the earlier years of production, the influence of the thin bed has not reached out radiay as far; to see the same cumulative recovery ratio, higher k_v values are needed.

Figure 8.2.7 illustrates the general process by which high-permeability thin beds enhance recovery from a reservoir. The thin beds drain rapidly to the wellbore, dropping the pressure in the thin bed. This pressure drop promotes vertical gas flow to the thin bed and through the thin bed to the wellbore. When the thin bed has dropped the pressure sufficiently in the vertical column, the thin-bed low-pressure region expands laterally away from the wellbore and the process of vertical drainage is repeated. The rate of lateral expansion is controlled by the thin-bed permeability and the volume of gas that it transmits from over- and underlying reservoirs, which is a function of reservoir thickness and pore volume. Where $k_v = 0$, there is no vertical gas supply to the thin bed.

In the Hugoton system the lowest-permeability rocks are generally the continental shaly very fine- to fine-grained siltstones and marine shales. A fundamental question is what role these might play in blocking vertical gas flow. Figure 8.2.8 examines the continental siltstone properties as a function of porosity and height above free-water level. Using the capillary-pressure equations, H_{afwl}-S_w curves were constructed for siltstones of various porosity and S_w was predicted for a range of H_{afwl} from 10 to 500 ft. Using the k_{ik}-ϕ_i trend to predict permeability and the relative permeability equations to predict relative permeability at the predicted water saturations, a final effective-gas permeability was calculated and, assuming a k_v/k_h ratio of 0.06, an effective vertical gas permeability was predicted. It is clear that the vertical permeability through the siltstones changes with H_{afwl}. Siltstones with ϕ_i>12% exhibit $k_v > 1x10^{-5}$ over nearly the entire vertical section and are therefore not a barrier to flow but can be a restriction at $H_{afwl} < 200$ ft. Siltstones with ϕ_i<8% are water saturated over much of the rock column. These may initially present barriers to flow. However, with pressure depletion in overlying beds, it is possible that high-pressure underlying beds may displace water from the siltstones into the depleted overlying beds and vertical communication may be established where there was none at the start. The pressure depletion of high permeability beds would also shift them lower on their capillary pressure curve which would increase the capillary force for them to imbibe water from adjacent saturated intervals. The nature of possible dewatering of the siltstones into overlying low-pressure carbonates is a complex function of the differences in capillary-pressure properties between the beds, the initial water saturations, and the pressures in the overlying, underlying, and siltstone beds.

References

Castle, J.W., and Byrnes, A.P., 1998, Petrophysics of low-permeability Medina sandstone, northwestern Pennsylvania, Appalachian Basin, The Log Analyst, v. 39, no. 4, p. 36-46.

Byrnes, A. P., 2005, “Permeability, capillary pressure, and relative permeability properties in low-permeability reservoirs and the influence of thin, high-permeability beds on production”, *in “Gas in Low Permeability Reservoirs of the Rocky Mountain*

Region", Rocky Mountain Assoc. of Geologists 2005 Guidebook CD, M.G. Bishop, S.P. Cumella, J.W. Robinson, and M.R. Silverman *eds.*, p. 69-108.

Warren, J.E., and Price, H.S., 1961, Flow in heterogeneous porous media, Soc. Petroleum Eng. J., v. 1, no. 3, p. 153-170.

Fetkovich, M.J., D.J. Ebbs Jr., and Voelker, J.J., 1994, Multiwell, multilayer model to evaluate infill-drilling potential in the Oklahoma Hugoton field, SPE Reservoir Engineering, Aug 1994, p. 162 – 168.

Oberst, R.J., P.P. Bansal, M.F. Cohen, and T.C. Ryan, 1994, 3-D reservoir simulation results of a 25-square mile study area in the Kansas Hugoton gas field, SPE 27931, SPE Mid-continent Gas Symposium, Amarillo, TX

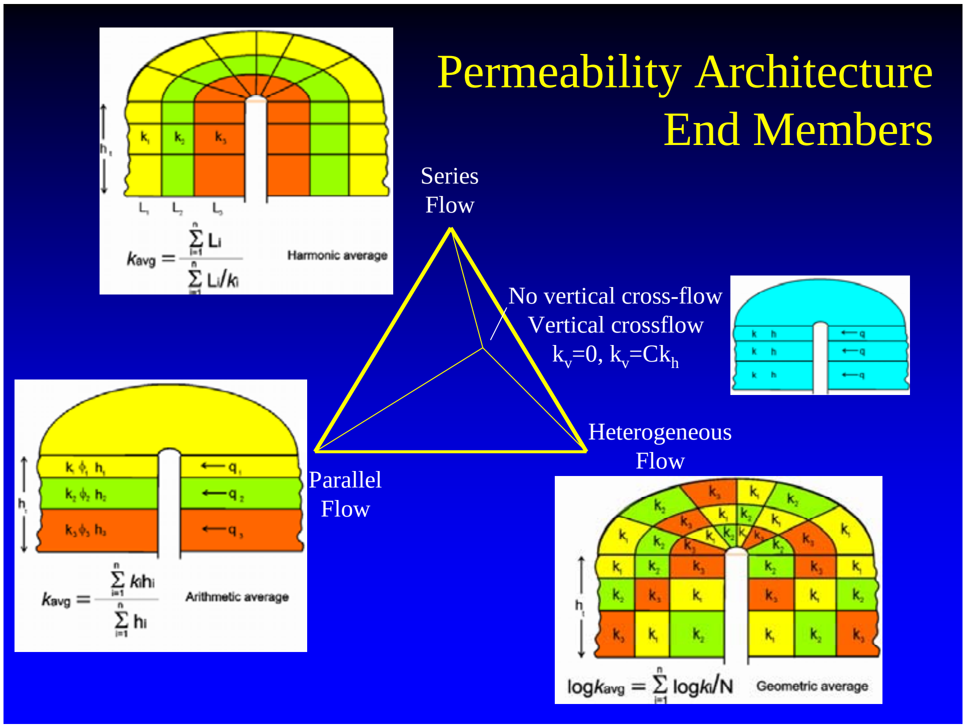

Permeability Architecture End Members

Figure 8.2.1. Basic end-member permeability averaging models that must be considered when upscaling permeability data and developing flow models for low-permeability sandstone reservoir systems. Frequently applied geometric averaging of permeability data is not always correct for sheet-like sandstone bodies.

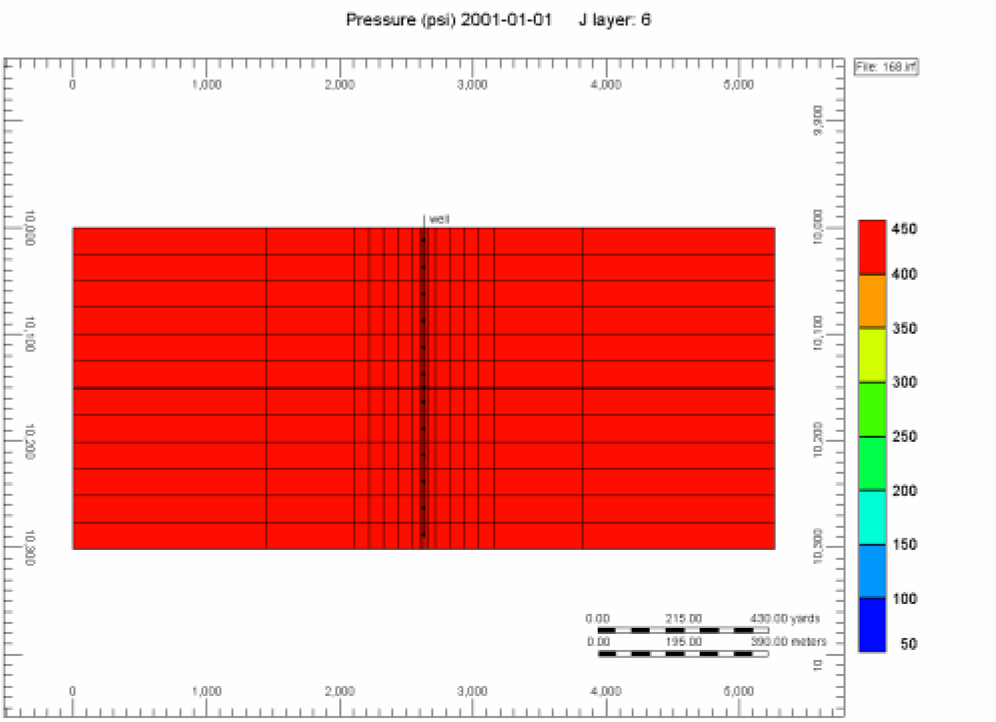

Figure 8.2.2. Computer Modeling Group (CMG) *IMEX* simulation model used to examine influence of reservoir properties. Large cross-section shows cut-away to vertical layer with gas well. Inset 3-D figures shows the central locations of the gas well. Both images show the variable gridcell spacing used to approach radial modeling. Model properties are discussed in text

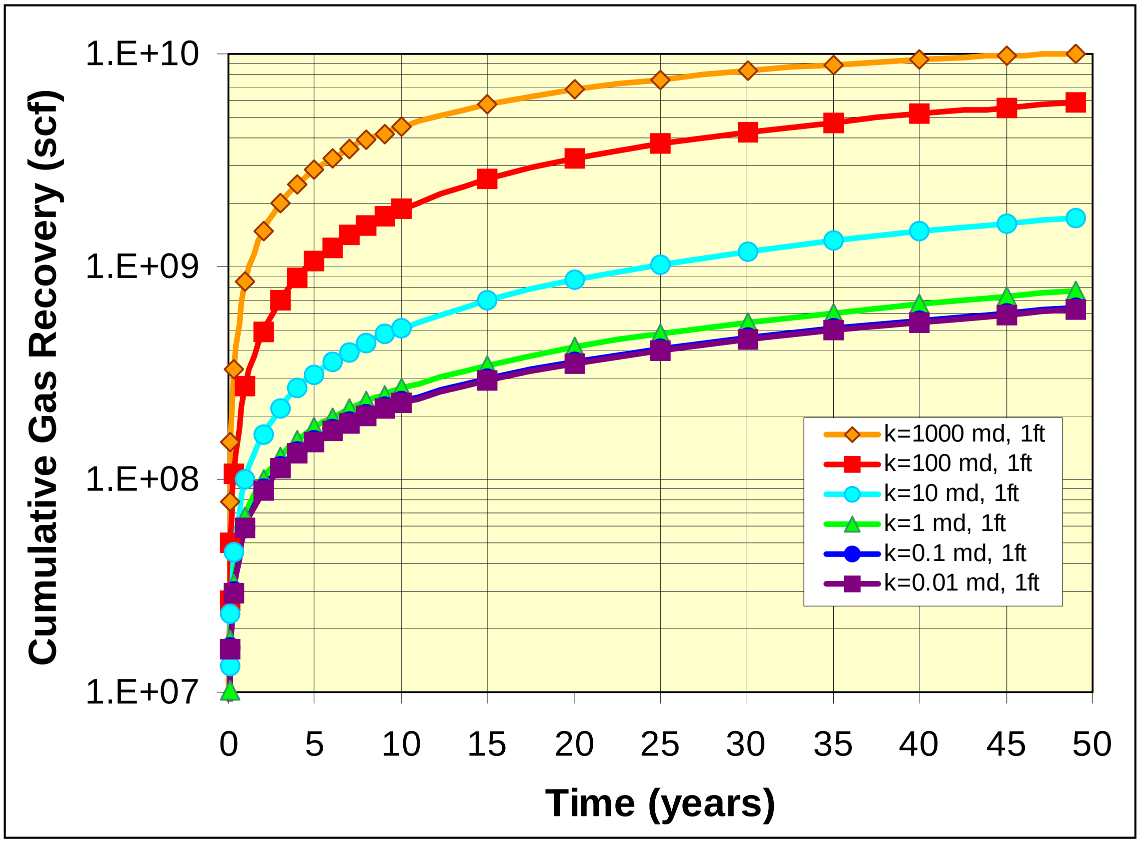

Figure 8.2.3. Cross-plot showing cumulative recovery for a 500-foot thick reservoir with permeability of 0.01 md and variable thin-bed permeabilities from 0.01 md to 1000 md. As the thin-bed permeability increases above 1 md cumulative gas recovery increases.

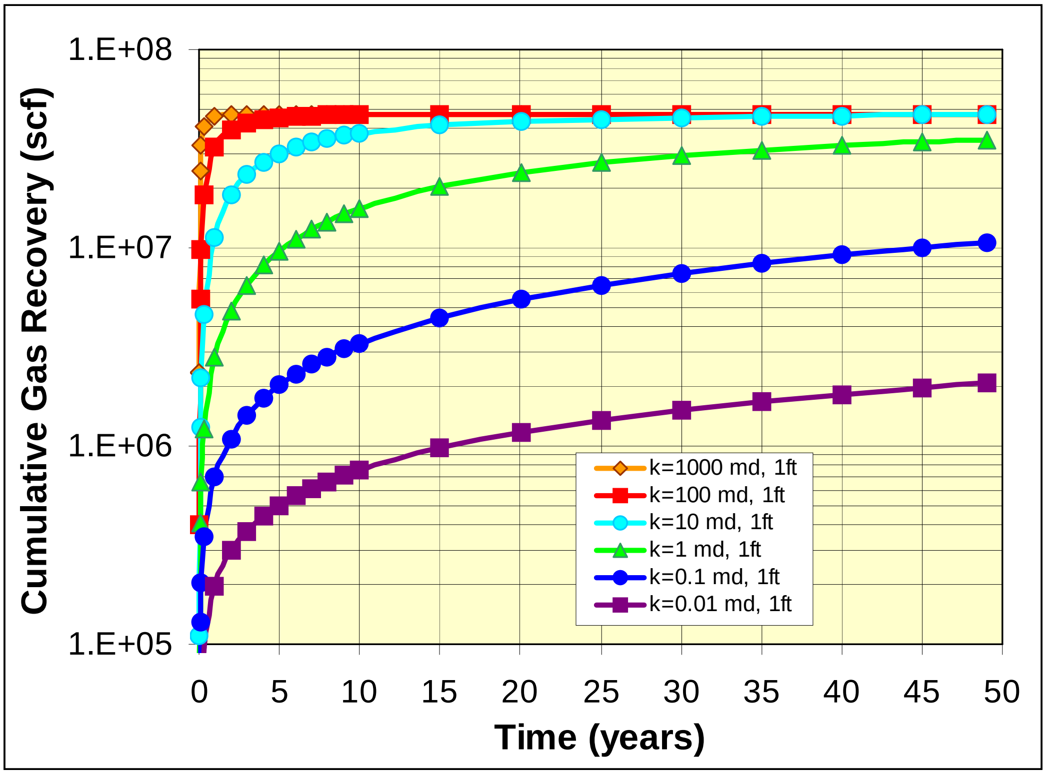

Figure 8.2.4. Cumulative gas recovery from a 1-ft thick bed alone with permeability varying from 0.01 md to 1000 md and with porosity of 10. Cumulative recovery for k>10 md beds stabilize before 50 years because drainage radius reaches boundary of model at 1 mile from wellbore.

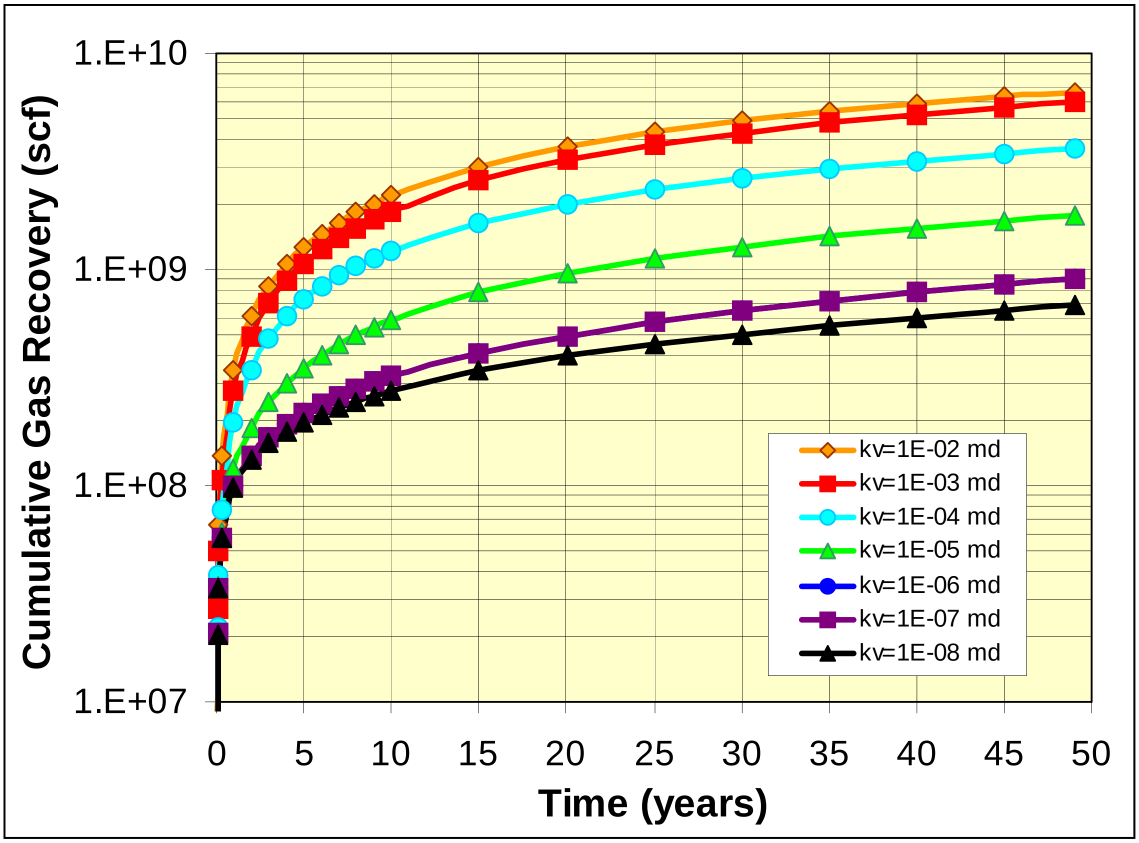

Figure 8.2.5. Cross-plot showing the dependence of cumulative gas on the vertical permeability (k_v) for a reservoir with 0.01 md and a 1-ft thick bed of 100 md, $P_{initial}$ =450, BHP=50 psi.

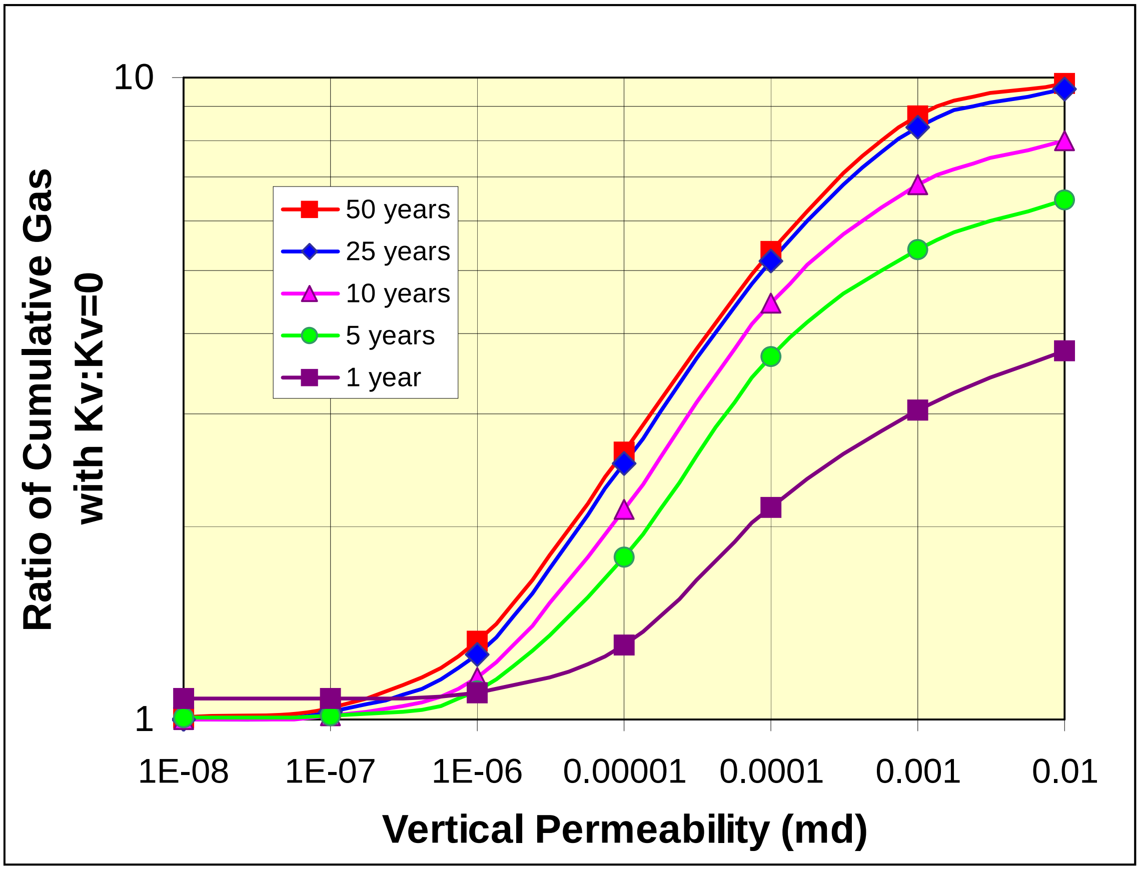

Figure 8.2.6. Cross-plot showing the dependence of incremental cumulative gas recovery over recovery with K_v=0 on the vertical permeability (k_v) for a reservoir with 0.01 md and a 1-ft thick bed of 100 md, $P_{initial}$ =450, BHP=50 psi Ratio increases with increasing time with expansion of drainage radius. Increase in k_v greater than $1x10^{-3}$ md does not significantly increase recovery over that obtained at k_v =$1x10^{-2}$ md. With k_v decrease below $1x10^{-3}$ md recovery decreases with decreasing K_v down to $1x10^{-7}$ md. For k_v below approximately ~$1x10^{-7}$ md recovery is similar to recovery for vertical permeability equal to zero, that is, no crosslfow and no vertical drainage to the high-permeability thin bed.

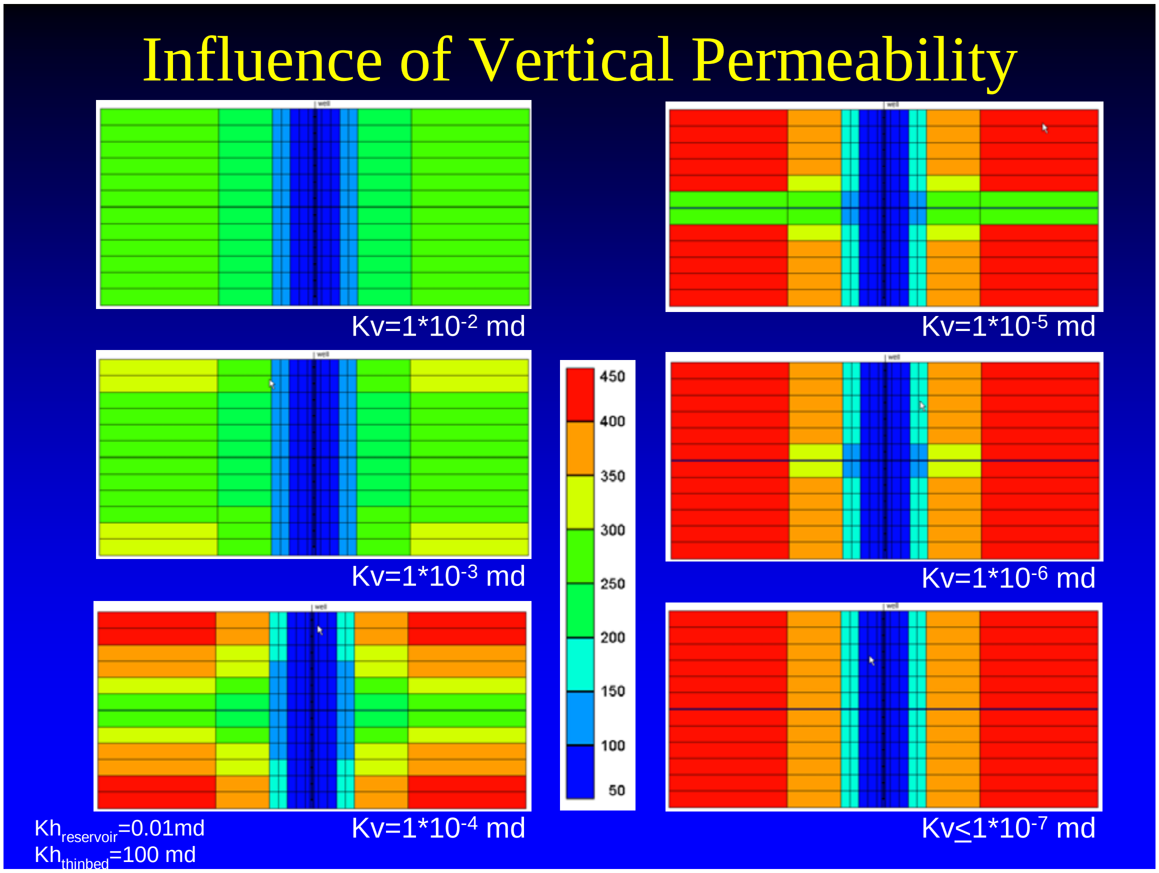

Influence of Vertical Permeability

$Kh_{reservoir}$=0.01md

$Kh_{thinbed}$=100 md

Figure 8.2.7. Example images showing thin bed reaching out and up and down with increasing Kv.

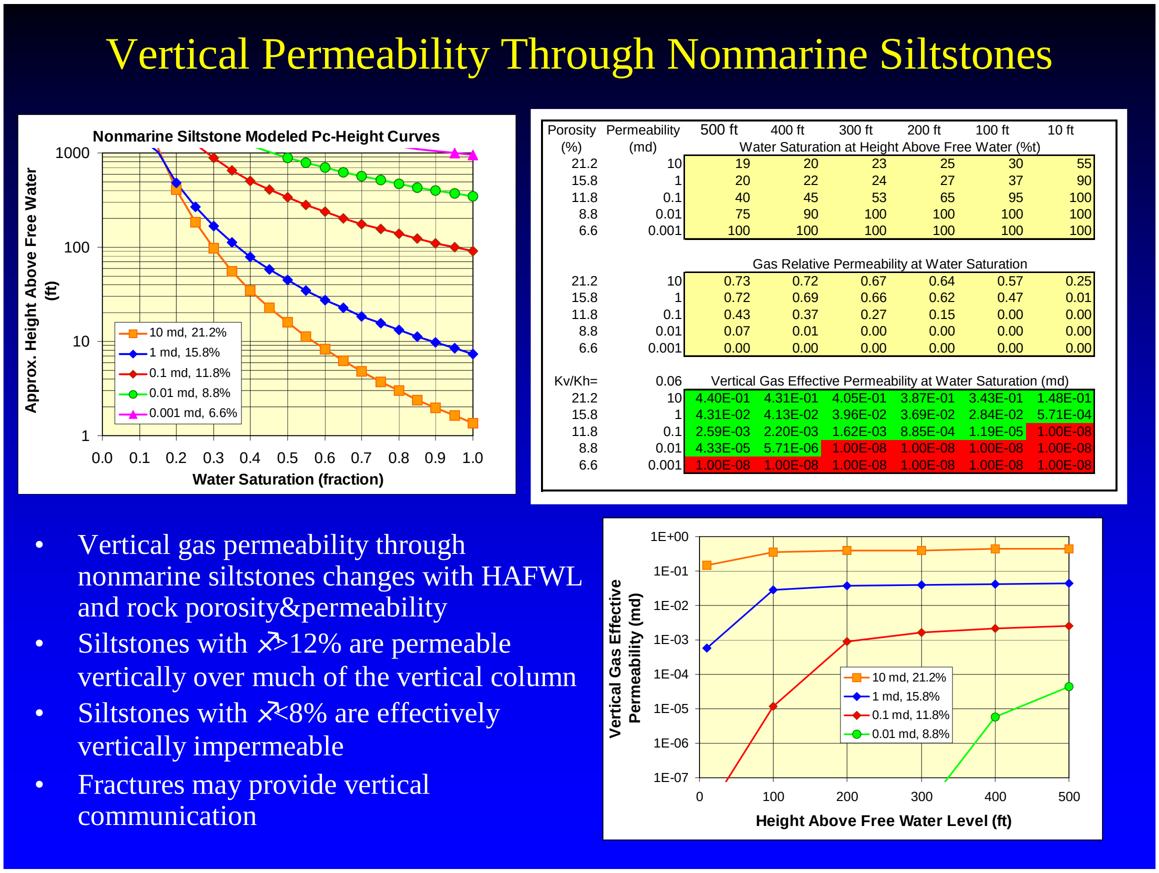

Vertical Permeability Through Nonmarine Siltstones

Porosity (%)	Permeability (md)	500 ft	400 ft	300 ft	200 ft	100 ft	10 ft
		Water Saturation at Height Above Free Water (%t)					
21.2	10	19	20	23	25	30	55
15.8	1	20	22	24	27	37	90
11.8	0.1	40	45	53	65	95	100
8.8	0.01	75	90	100	100	100	100
6.6	0.001	100	100	100	100	100	100
		Gas Relative Permeability at Water Saturation					
21.2	10	0.73	0.72	0.67	0.64	0.57	0.25
15.8	1	0.72	0.69	0.66	0.62	0.47	0.01
11.8	0.1	0.43	0.37	0.27	0.15	0.00	0.00
8.8	0.01	0.07	0.01	0.00	0.00	0.00	0.00
6.6	0.001	0.00	0.00	0.00	0.00	0.00	0.00
Kv/Kh=	0.06	Vertical Gas Effective Permeability at Water Saturation (md)					
21.2	10	4.40E-01	4.31E-01	4.05E-01	3.87E-01	3.43E-01	1.48E-01
15.8	1	4.31E-02	4.13E-02	3.96E-02	3.69E-02	2.84E-02	5.71E-04
11.8	0.1	2.59E-03	2.20E-03	1.62E-03	8.85E-04	1.19E-05	1.00E-08
8.8	0.01	4.33E-05	5.71E-06	1.00E-08	1.00E-08	1.00E-08	1.00E-08
6.6	0.001	1.00E-08	1.00E-08	1.00E-08	1.00E-08	1.00E-08	1.00E-08

- Vertical gas permeability through nonmarine siltstones changes with HAFWL and rock porosity&permeability
- Siltstones with ♐>12% are permeable vertically over much of the vertical column
- Siltstones with ♐<8% are effectively vertically impermeable
- Fractures may provide vertical communication

Figure 8.2.8. Properties of siltstones and their potential role as vertical flow barriers in early reservoir history.

8.3. COMMUNICATION BETWEEN CHASE AND COUNCIL GROVE

Martin K. Dubois

Introduction

In the study area, production is from the lower Permian Chase and Council Grove Groups (fig. 1), although field development up to the 1960’s was confined to the Chase Group. Gas was first discovered in widely spaced wells in Seward County, Kansas (1922) and a few years later (1925) in Texas County, Oklahoma. After a Stevens County, Kansas, discovery in 1927 the Hugoton began to emerge as a significant field when it was realized that the wells were drawing from a common reservoir (Hemsell, 1939; Pippin, 1970). Development was slow initially due to market and pipeline constraints and the field was not fully developed, and field limits defined, until the late 1950’s. In Kansas, the Hugoton field is defined by the State regulatory agency as production from the Chase Group and the Panoma field as production from the directly underlying Council Grove Group. Though regulated as separate fields in Kansas, in most places the gas column is continuous between the two stratigraphic intervals inside the Panoma boundary (Pippin, 1970; Parham and Campbell, 1993) and reaches a maximum thickness of 500 ft (150 m) in the west central part of the study area. It has been recognized that the Hugoton field has a sloped gas-water contact, and we interpret a sloped free water level (FWL), that is several 100’s of feet (100’s m) higher at the west updip margin than on the east downdip limits (Garlough and Taylor, 1941; Hubbert, 1953, 1967; Pippin, 1970; Sorenson, 2005). Outside the Panoma field boundary, vertical continuity between the Chase and Council Grove is limited. In Oklahoma Council Grove production outside the Panoma produces from Council Grove intervals that are up to 300 ft (100 m) below the lowest perforations in the Chase. The trapping mechanism for these accumulations is unrelated to the Panoma and is not part of this discussion. Another exception may occur in the very western portion of the field in Kansas described by Olson and others (1997) as being compartmentalized by faults.

The main pay zones in the Hugoton are the 13 thin (mean thickness 6-70 ft, 2-21 m) marine; mainly carbonate intervals (six in the Chase and seven in the Council Grove), deposited during sea level highstands. These are separated by continental, mainly siltstone (redbed) intervals (mean thickness 6-25 ft, 2-8 m) deposited during sea level lowstands, when most of the shelf was exposed. The siltstones generally have poor reservoir quality and vertically isolate, or restrict communication between, the 13 pay intervals (Siemers and Ahr, 1990; Ryan et al., 1994; Oberst et al., 1994; Olson et al., 1997). Although the Hugoton and Panoma fields appear to be one large reservoir system that may have filled and changed pressure in stages (Sorenson, 2005), the 6 pay zones in the Chase portion of the layered reservoir are being depleted at different rates as indicated by different pressures exhibited by individual zone tests and reservoir simulation (Ryan et al., 1994; Oberst et al., 1994; Fetkovich et al., 1994). Oberst et al. (1994) and Fetkovich et al. (1994) treated the siltstone intervals between the marine carbonates as no-flow layers and the marine carbonate pay zones as separate reservoirs in their simulation work that only included the Chase. Our simulation work and zone pressures provided to this study suggest that all 13 pay zones in the Chase and Council Grove are being depleted at different rates.

Conflicting observations and possible conduits

A number of observations suggest that all 13 Wolfcampian pay zones are isolated reservoirs but others suggest that the entire system is connected.

1. The Hugoton and Panoma pressures generally track one another suggesting that vertical communication exists between the two fields that are regulated as separate reservoirs.
2. Pressure-by-zone data show that individual zones are depleted at different rates, suggesting a lack of communication between zones.
3. Siltstone layers separating the marine carbonates in the Chase and Council Grove have similar properties and nothing is unique about the Speiser Shale that separates the Chase from the Council Grove. Either the marine carbonates are all sealed or none is sealed, at least for a given height above free water level.
4. Permeabilities calculated from drill-stem tests approximate core-plug permeability, ruling out closely spaced natural fractures that could connect the reservoir system.

In this section we will lay out evidence that suggests that the Chase and Council Grove are in communication. This communication could be natural and on a regional scale or be induced by hydraulic-fracture treatments during completions, or both. As a working hypothesis, we suggest that, locally, matrix-driven properties are in play, but swarms of small fractures or larger regional fractures correlated with basement faults and fractures may be contributing to the large-scale communication (Figure 8.3.2).

Pressures suggest communication at varying scales

Pressure data are a very effective means of evaluating communication between reservoir volumes. Three types of pressure data are available in the Hugoton, 72-hour wellhead shutin pressures (WHSIP), long-term WHSIP, and individual zone-pressure tests from drill stem tests (DST) or repeat formation tests (RFT), described in Table 8.3.1. WHSIP are abundantly available due to requirements that wells be tested at least every two years and these data are in the public domain. One drawback is that the WHSIP measures the pressure of the lowest pressured, highest permeability in the commingled wellbore.

Grant County, Kansas, is ideal for comparing WHSIP for different classes of wells (Hugoton or Panoma) because it is in the center of the field and fully developed for the Hugoton (Chase), Panoma (Council Grove), and the Hugoton infill (Chase). The 4X4 township county has 576 regular sections. Digital Wellhead Shutin Pressure (WHSIP) data since the 1930’s and annual production data since 1969 are available. Figure 8.3.3 is a composite or average initial WHSIP for Panoma wells by year compared to the average field-wide WHSIP for the Hugoton. More than two decades separate the development of the two fields, but if truly separate, the Panoma Field should have had an IBHP >= to that for the Hugoton (435 psi) unless the reservoir in which it was completed had been partially drained. On average, early Panoma wells started at pressures close but slightly less than the Hugoton field-wide pressure. This is not surprising because this is the field-wide average for Kansas Hugoton, and the first area of development in the Council Grove took place in roughly the same region that the earliest Chase (Hugoton) production was established; and the wells were completed before much gas had been withdrawn from the Hugoton. When Panoma development accelerated in 1970, the average IWHSIP was under 300 psi, significantly less than the original Hugoton of 435 psi. Keep in mind that the fields are both prorated and production was limited to less than the wells were capable of producing through much of their life. Since Panoma IWHSIP, the first pressure readings when a well is put on line is 300 psi rather than something closer to 435 psi, it appears likely that a substantial amount of gas may have been removed from the Council Grove prior to completion of the majority of the Panoma wells.

Composite WHSIP through 2004 for Grant County, an average of all WHSIP by class of wells, Hugoton parent, Panoma, and Hugoton infill, is shown in Figure 8.3.4. Data before 1969 are IWHSIP and after 1969 are all WHSIP. The average pressure for all classes is within a few psi and their respective plots parallel each other very closely. It is highly doubtful that this phenomenon is coincidental; however, the fields are regulated and rate-constrained, in part to ensure that the Panoma wells, withdrawal does not impact the Hugoton well production (Ford, 1982). Since the mid-1990's, however, most wells have been allowed to produce at capacity and the pressures still closely parallel each other, suggesting that they are drawing from a common reservoir.

Potential interference between classes of wells

Figure 8.3.5 is a composite, or average pressures, for the combined Hugoton, Panoma, and Hugoton infill well dataset for Grant County. The first curve (yellow) is the Hugoton "Parent" well where there appears to be two changes in slope. The first change, a subtle one, is coincident with the ramping-up of Panoma development. The second curve (pink) combines Hugoton and Panoma wells and illustrates a more dramatic change that is coincident with Hugoton infill development. Combining the Hugoton-Parent with the Panoma production and pressures "removes" the interference of the Panoma wells (pink), and the one change in slope is probably interference by the Hugoton infill wells. Finally, combining all production and pressures (blue) yields a linear trend without significant departures. It appears that the entire system may be in communication with Panoma wells interfering with Hugoton-Parent wells and Hugoton-Infill wells interfering with both Panoma and Hugoton-Parent wells. Possible influence or interference by the addition of wells was first noticed in modeling a unit (9 square miles) in Grant County (Figure 8.3.6). There appeared to be a change in slope of the composite P/Z vs. Cumulative Gas trend line for the nine Panoma wells (Council Grove) from contiguous units that were coincident with the timing of the drilling and completion of nine Hugoton

Infill wells (Chase). The same patterns of potential interference among all three classes of wells at the county scale are also observed at the nine-unit scale (Figure 8.3.7).

Caveats with wellhead shut-in pressure

WHSIP does not accurately reflect BHP for all layers (Table 8.3.2), and more closely approximates the zone having the highest permeability, greatest depletion, and lowest pressure. It has been recognized that 72-hour WHSIP taken for proration purposes under-estimates actual WHSIP due to insufficient time for the entire reservoir to equilibrate. Plotted in Figure 8.3.8 are the composite or average long-term WHSIP for Chase and Council Grove wells in Stevens County, Kansas that illustrate this phenomenon. Wells of both fields (Hugoton and Panoma) were shut in more than a hundred days. The hundred-day WHSIP is 33-50% higher than 72-hour WHSIP (30 psi). Although it is certain that 72-hour WHSIP cannot be used to project remaining GIP, it remains a useful metric in evaluating communication and relative depletion and is available for practically all wells through time in the field. When SIP for Chase wells in the data set are extrapolated for 100 years, the resulting pressure is 89 psi in 100 years with an R-square of 0.952. This would suggest that there is three times remaining pressure than the 72-hour WHSIP would indicate, and may be a more accurate reflection of remaining producible GIP. Extrapolation of already long term WHSIP for an even longer period may prove useful, but needs additional study to ascertain of its validity.

WHSIP through time and space

Earlier discussions considered pressures through time and there are distinct correlations of the pressures between classes through time. A 3D-visualization tool developed for this study takes advantage of temporally and spatially related pressure to view the data in higher dimensions. One of the functions of the tool is to create an isobar surface through the volume of pressure data arranged in a 3D volume, where XY are coordinates and Z = time. Figure 8.3.9 illustrates a map view of the 170-psi surface for the Panoma in Grant County that is sliced horizontally with an opaque surface that is the first derivative of the Ft Riley structure map (dip map). High areas of dip are warm. The variation among the four images is the change in opacity of the isobar surface. There seems to be a strong correlation between areas where 170 psi is attained later in the life of the field and lineament in the dip map that is an opaque surface placed at 1976 on the z-axis. Areas below the surface are where that pressure was attained at an earlier date. This phenomenon persists through time. It would seem logical that these areas of higher pressure would correlate with areas with less production, but a first pass suggests that this is not the case and possibly the opposite relationship may exist. We suggest that the higher pressure may be a result of there being a higher concentration of small fractures and joints (swarms) throughout the Chase and Council Grove associated with the lineaments that could be in turn associated with basement faults and fractures. A higher incidence of fractures would facilitate the movement of gas from the lower-permeability rocks and thus the WHSIP would be better equilibrated in these regions.

Figure 8.3.10 compares isobar surfaces at 143 psi for the Panoma and Council Grove in 1981. The spatial relationships are nearly identical, although the Panoma appears to be approximately two years behind the Hugoton, that is, the Panoma is higher in pressure than the Hugoton and reaches a given pressure two years after the Panoma (Figure 8.3.11). This is also apparent in the 2D plot in Figure 8.3.4. The strong correlations through both space and time for the Panoma and Hugoton suggest that the same processes are at work on the two systems in space and time, or that they are part of the same larger system, or both.

Fort Riley dip and possible relation to basement fractures and faults

A very large data set (12,000+ tops) allows for very well constrained structure map on the top of the Chase Group, Fort Riley Limestone Member. The first derivative, a dip-intensity map (Figure 8.3.12), bears strong relationship with known basement-related faults in the Hugoton area and we feel that it reflects other smaller faults and fractures as well. The known faults rarely cut the Wolfcampian, but we suggest that they could control the distribution of small fractures in the reservoir system. Figure 8.3.13 is an enlarged portion of the Fort Riley dip map in the Flower simulation model area. We have enhanced the lineaments with hand-drawn lines that subjectively classify the lineaments into three classes of intensity. The distribution is on the township to multi-section scale in this view, but at county a larger scales in the Figure 8.3.12 view.

Nearly vertical open fractures in core (Figure 8.3.14) were noted in all 28 of the cores examined in the study, although their frequency was highly variable, consistent with the swarms of fractures concept. Joint frequency and geometry in some cores suggest that if regular (square), they may occur in 10-15 ft patterns. For comparison, Figure 8.3.15 illustrates a regularly spaced joint system in Silverdale member quarry, Fort Riley Limestone Member, in southeast Kansas.

Conclusions

Pressure data for Hugoton and Panoma show similar patterns in distribution of pressure through space and time and suggests that the two systems are in communication. Slightly higher WHSIP persists though time in a given space in both the Chase and Council Grove and appears to correlate with basement-related fractures. The two systems are behaving as one reservoir system unless they are separate and behaving exactly the same, which is unlikely. Recurrent movement along basement fractures or tension related to bending could cause higher frequency of open joints (swarms) in linear to sub-linear trends that provide better communication within zones having low permeability, enabling better equilibration of WHSIP.

References

Dubois, M. K., A. P. Byrnes, and R. Brownrigg, 2005, Reservoir pressures suggest communication between Hugoton and Panoma Fields and provide insights on the nature of the connections (abs): American Association of Petroleum Geologists Midcontinent Section Meeting, Oklahoma City, Oklahoma. http://www.kgs.ku.edu/PRS/Poster/2005/MidcontAAPG/index.html (accessed 9/21/06)

Fetkovitch, M. J., D. J. Ebbs Jr., and J. J. Voelker, 1994, Multiwell, multilayer model to evaluate infill-drilling potential in the Oklahoma Hugoton field: Society of Petroleum Engineers, 65th Annual Technical Conference and Exhibition, New Orleans, Paper SPE 20778, p. 162-168.

Ford, J. D., 1982, Historical and reservoir engineering study of the Panoma Council Grove field in Wichita, Finney, Kearny, Hamilton, Haskell, Grant, Stanton, Seward, Stevens and Morton counties, Kansas: Society of Petroleum Engineers, Paper SPE 11667, 31 p.

Garlough, J. L., and G. L. Taylor, 1941, Hugoton gas field, Grant, Haskell, Morton, Stevens, and Seward counties, Kansas, and Texas County, Oklahoma: *in* Levorsen, A. I., ed., Stratigraphic Type Oil Fields: American Association of Petroleum Geologists, Tulsa, p. 78-104.

Hemsell, C. C., 1939, Geology of Hugoton Gas Field of southwestern Kansas: American Association of Petroleum Geologists, Bulletin, v. 23, no. 7, p. 1054-1067.

Hubbert, M. K., 1953, Entrapment of petroleum under hydrodynamic conditions: American Association of Petroleum Geologists, Bulletin, v. 37, p. 1954-2026.

Hubbert, M. K., 1967, Application of hydrodynamics to oil exploration: 7th World Petroleum Congress Proceedings, Mexico City, v. 1B: Elsevier Publishing Co., LTD, p. 59-75.

Oberst, R. J., P. P. Bansal and M. F. Cohen, 1994, 3-D reservoir simulation results of a 25-square mile study area in Kansas Hugoton gas field: Society of Petroleum Engineers Mid-Continent Gas Symposium, Amarillo, TX, Paper SPE 27931, p. 137-147.

Olson, T. M., Babcock, J. A., Prasad, K. V. K., Boughton, S. D., Wagner, P. D., Franklin, M. K., and Thompson, K. A., 1997, Reservoir characterization of the giant Hugoton Gas Field, Kansas: American Association of Petroleum Geologists, Bulletin, v. 81, p. 1785-1803.

Parham, K. D., and J. A. Campbell, 1993, PM-8. Wolfcampian shallow shelf carbonate-Hugoton Embayment, Kansas and Oklahoma: *in* D. G. Bebout, ed., Atlas of Major Midcontinent Gas Reservoirs: Gas Research Institute, p. 9-12.

Pippin, L., 1970, Panhandle-Hugoton field, Texas-Oklahoma-Kansas-The first fifty years, *in* Halbouty, M. T. (ed.), Geology of Giant Petroleum Fields: American Association of Petroleum Geologists, Memoir 14, Tulsa, p. 204-222.

Ryan, T. C., M. J. Sweeney, and W. H. Jamieson Jr., 1994, Individual layer transient tests in low-pressure, multi-layered reservoirs:
Society of Petroleum Engineers Mid-Continent Gas Symposium, Amarillo, TX, Paper SPE 27928, p. 99-113.

Siemers, W. T., and W. M. Ahr, 1990, Reservoir facies, pore characteristics, and flow units: Lower Permian Chase Group, Guymon-Hugoton Field, Oklahoma: Society of Petroleum Engineers Proceedings, 65th Annual Technical Conference and Exhibition, New Orleans, LA, September 23-26, 1990, Paper SPE 20757, p. 417-428.

Sorenson, R. P., 2005, A dynamic model for the Permian Panhandle and Hugoton fields, western Anadarko basin: American Association of Petroleum Geologists Bulletin, v. 89, no. 7, p. 921-938.

Tables:

Main types	Utility	Shortfall
1. 72 hour well head shut in pressure (WHSIP) Extensive in Kansas and Oklahoma.	Connectivity within and "between" reservoirs at various scales	Commingled, equals lowest pressured zone
2. Long term (equilibrated) buildup Abundant locally, absent otherwise.	Implications on ultimate recovery and field life	Dense data but only in one area
3. Pressure by zone (layer) through time Modest amount of data.	Critical for estimating remaining GIP and simulation	Minimal scattered data

Table 8.3.1 Types of pressure data available in study area.

Group	Zone	1994 Science Well		2005 Replacement Well
		DST-SIP psi (kPa)	Composite psi(kPa)	XPT^{TM}-SIP* psi (kPa)
CHASE GROUP	Herington	120 (830)	104 (720)	19 (130)
	Krider	88 (610)		21 (145)
				30 (210)
	Winfield SS	105 (720)		141 (970)
	Winfield LS	121(830)		217 (1500)
	Towanda	230 (1590)		165 (1140)
	U. Ft. Riley	>400 (2750)		192 (1320)
	Florence	398 (2740)		265 (1830)
	Wreford	372 (2570)		219 (1510)
COUNCIL GROVE GROUP	A1_LM	400 (2760)	156 (1080)	nt
	B1_LM	350 (2410)		nt
	B2_LM	131(900)		nt
	B3_LM	368 (2540)		386 (2660)
	B4_LM	215 (1480)		nt
	B5_LM	160 (1100)		348 (2400)

Table 8.3.2 Pressures by zone for two relatively closely spaced wells. The well, drilled in 1994, was a research well (Flower A1), drilled with a foam fluid to limit filtrate invasion and formation damage. Pressures are 24-hr shut-in pressures from drill-stem tests. The well drilled in 2005 is located 6 mi (10 km) north of the earlier well and pressures were recorded in the open hole by Schlumberger's XPT^{TM} tool, a repeat formation tester.

Figures:

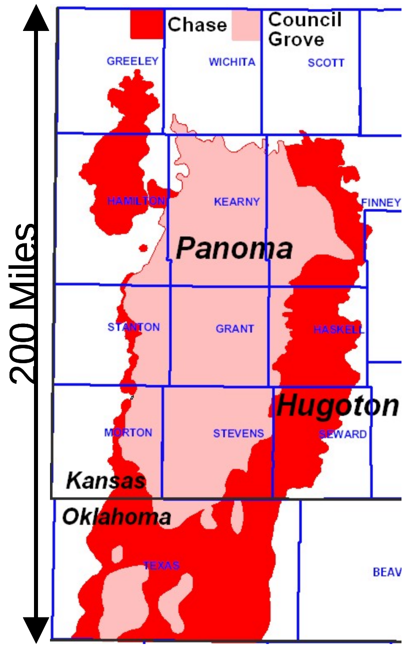

Figure 8.3.1 Hugoton (Chase) and Panoma (Council Grove) in Kansas and Oklahoma

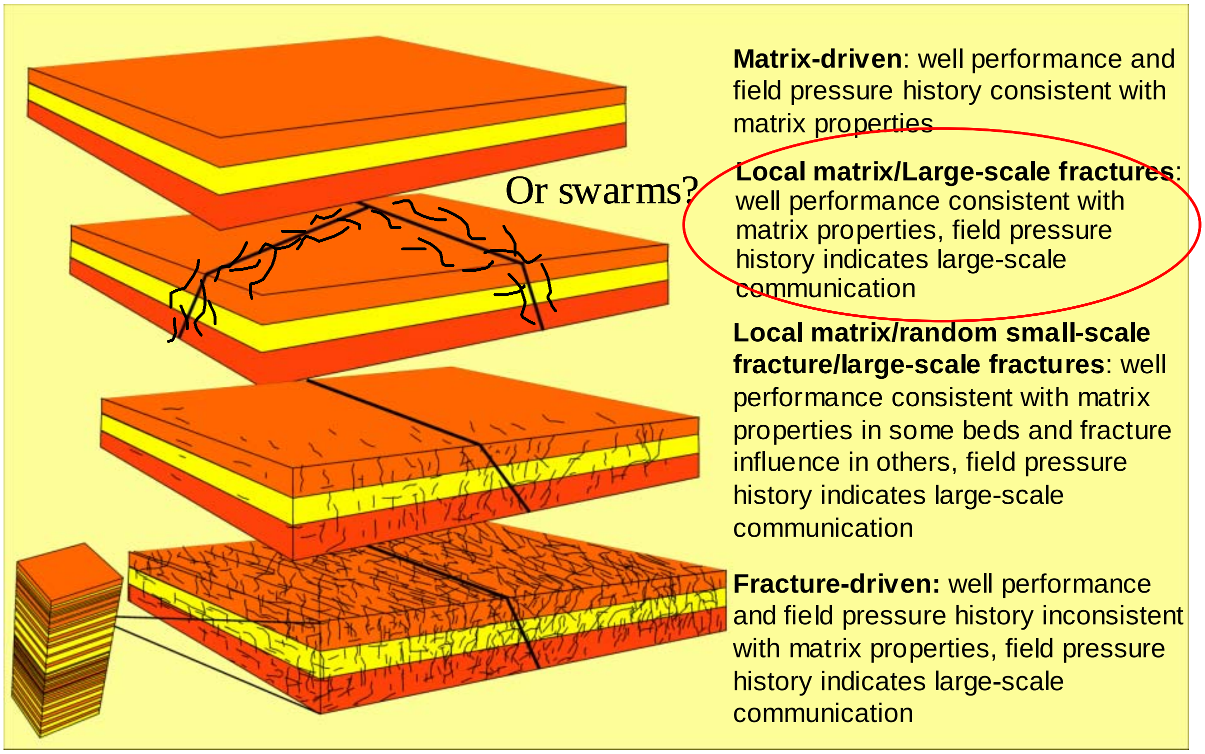

Or swarms?

Matrix-driven: well performance and field pressure history consistent with matrix properties

Local matrix/Large-scale fractures: well performance consistent with matrix properties, field pressure history indicates large-scale communication

Local matrix/random small-scale fracture/large-scale fractures: well performance consistent with matrix properties in some beds and fracture influence in others, field pressure history indicates large-scale communication

Fracture-driven: well performance and field pressure history inconsistent with matrix properties, field pressure history indicates large-scale communication

Figure 8.3.2 Four scenarios for reservoir-communication mechanisms with matrix-driven and fracture-driven at opposite ends of a continuum. The Hugoton may be an example of a reservoir with communication by large-scale fractures (township-scale) but locally controlled by matrix properties.

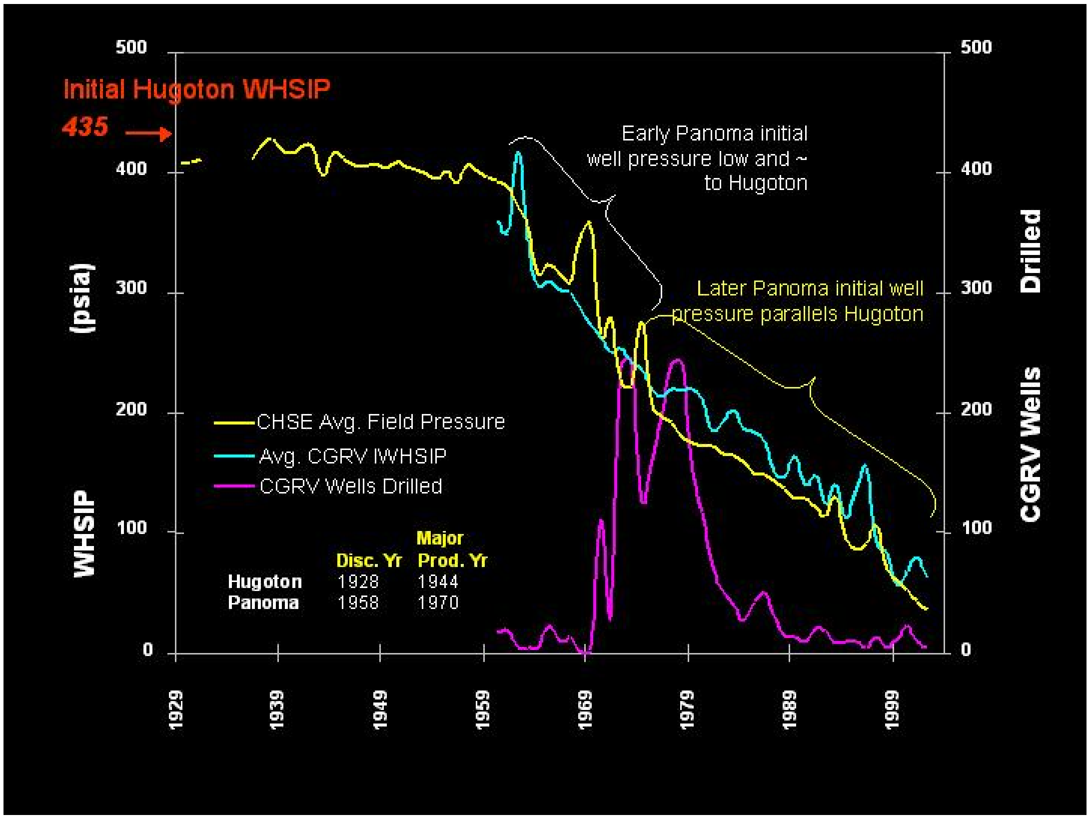

Figure 8.3.3. Composite (average) Panoma initial WHSIP and Hugoton average field-wide WHSIP through time for Kansas. Most Panoma wells were drilled after 1970, and their average IWHSIP is less than 300 psi.

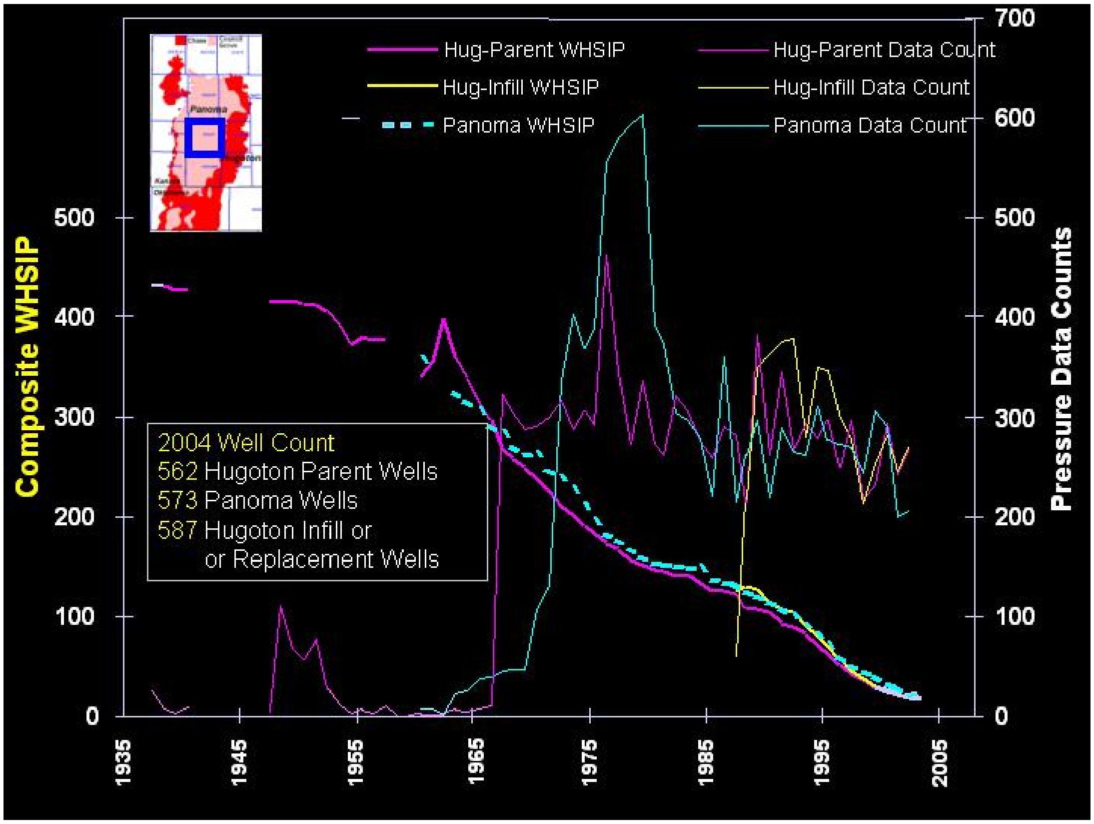

Figure 8.3.4 Hugoton and Panoma composite WHSIP, Grant County, Kansas.

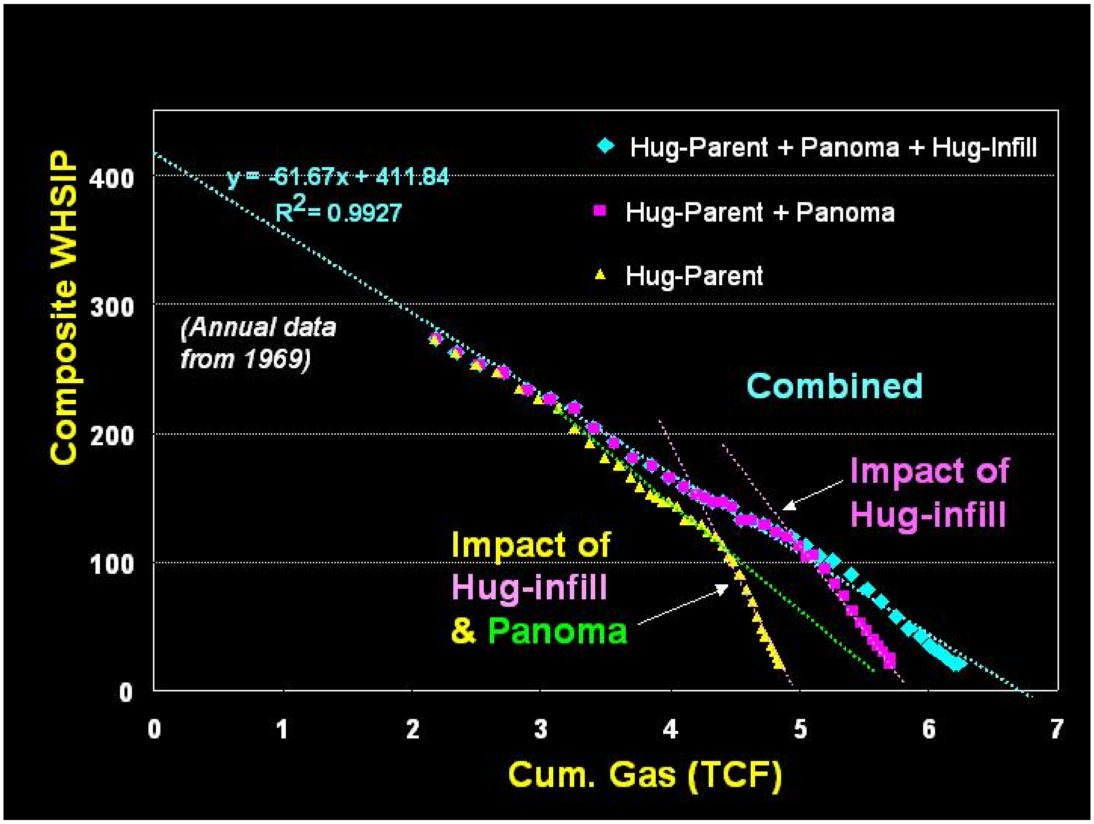

Figure 8.3.5. Composite, or average pressures vs. cumulative production for the combined Hugoton, Panoma, and Hugoton infill well dataset for Grant County. The first curve (yellow) is the Hugoton "parent," second is Hugoton parent + Panoma (pink), and the third includes Hugoton parent, Panoma, and Hugoton infill (blue).

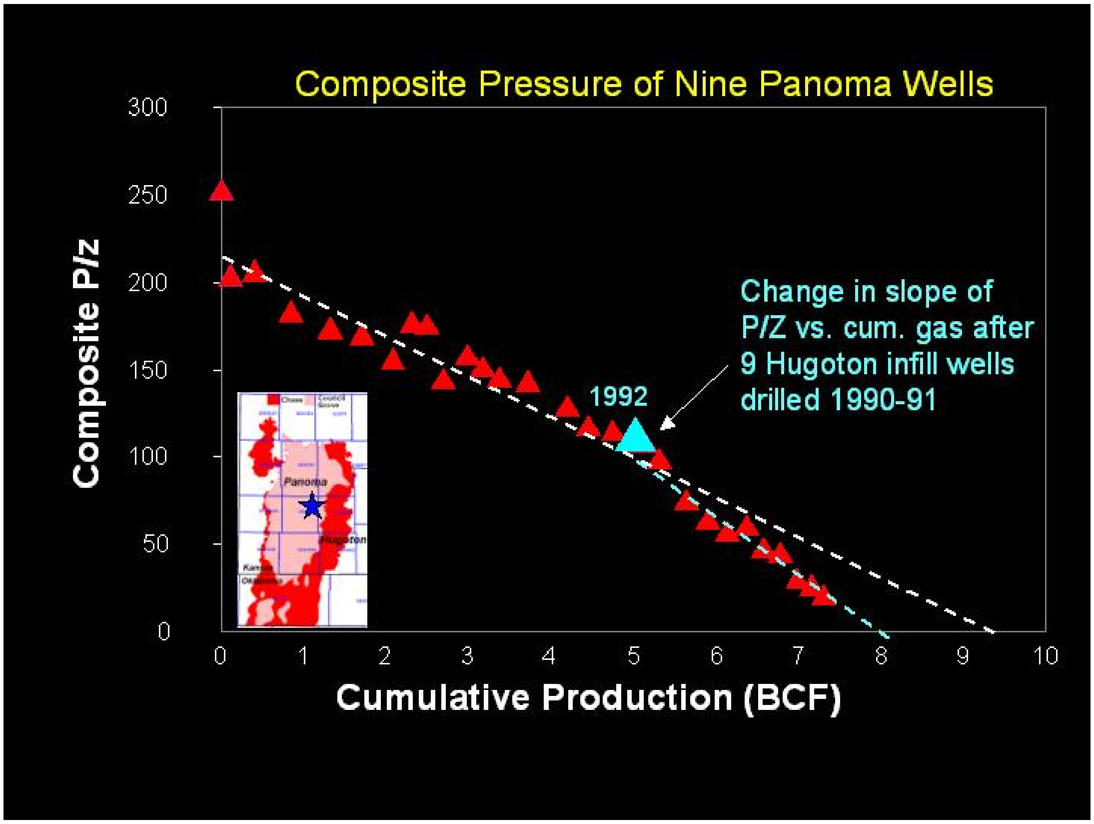

Figure 8.3.6. Composite P/Z vs. cumulative gas for nine Panoma wells in contiguous nine-units in Grant County, Kansas.

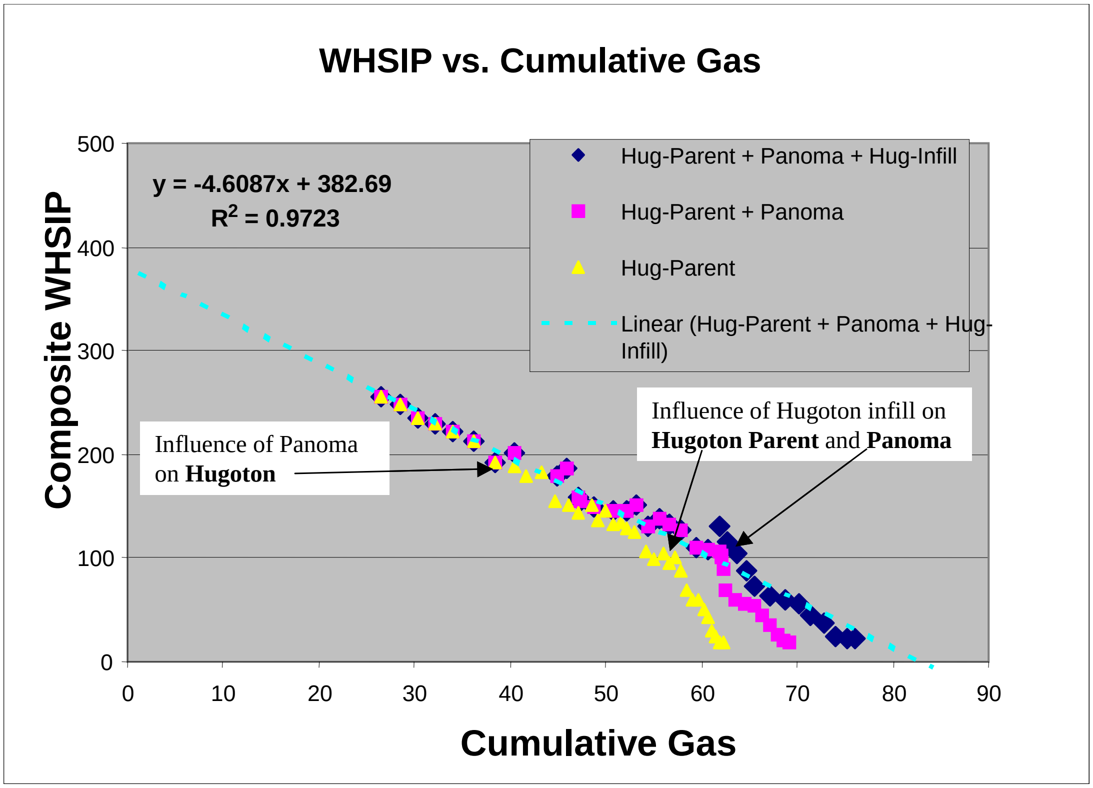

Figure 8.3.7. Plot of same wells in Fig. 8.3.6 plotted in same manner as in Fig. 8.3.5.

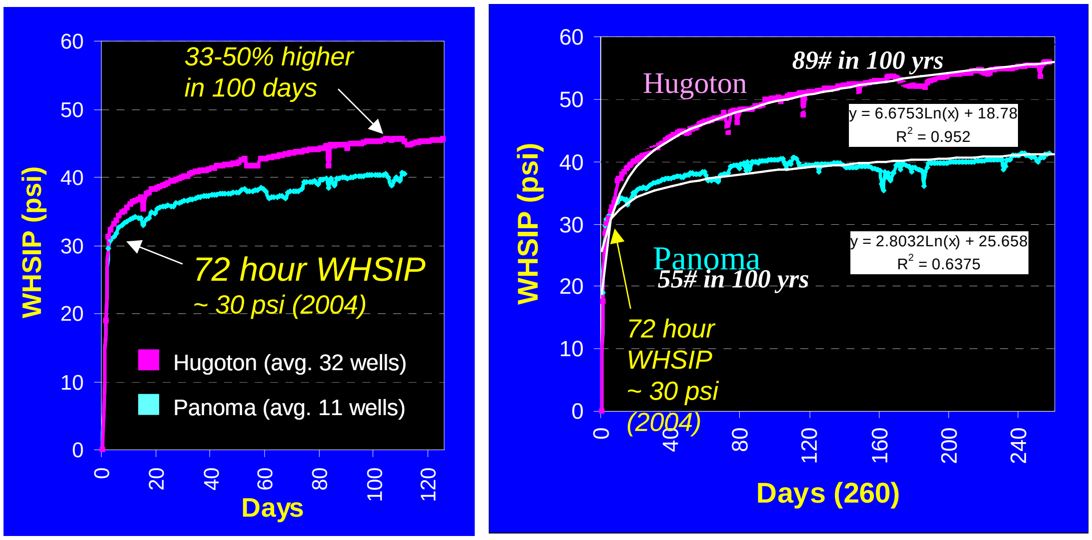

Figure 8.3.8. Composites of long-term wellhead shut-in pressures for Panoma and Hugoton wells in Stevens County, Kansas.

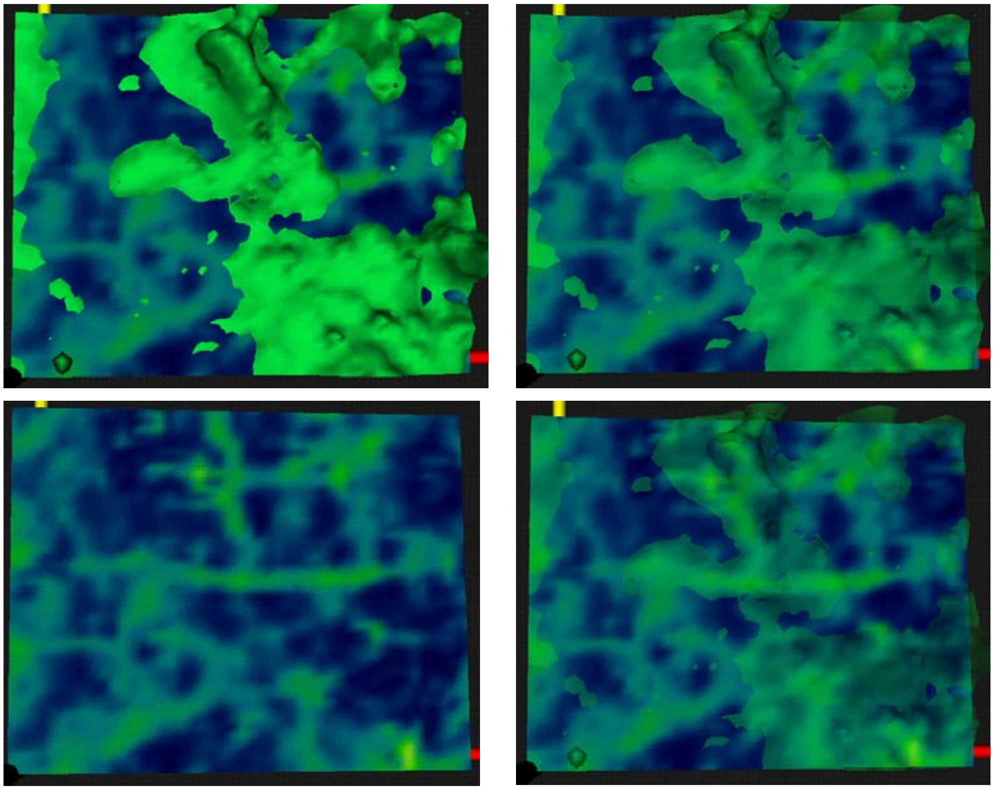

Figure 8.3.9. Relationship of Panoma Isobar Surface to Fort Riley Dip Surface, Grant County, Kansas. Areas with high rates of dip (warmer colors) may be areas where joints and fractures provide more effective communication between layers and thus higher WHSIP as gas is fed from higher-pressure layers. Pressure =176 psi and year =1976.

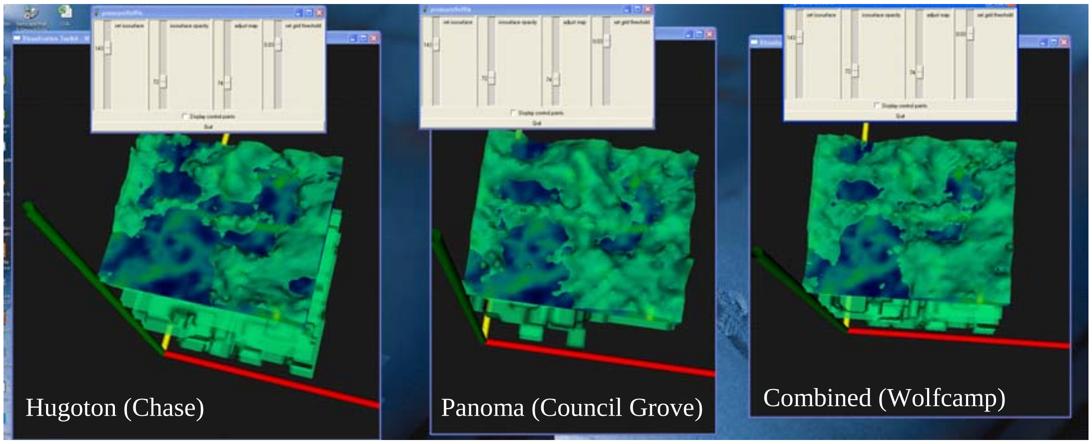

Figure 8.3.10. Hugoton and Panoma WHSIP and Fort Riley dip map, Grant County, Kansas. WHSIP isobar surface = 143 psi X-axis (red) points East, Y (yellow) is North, and Z is time increasing upward. Fort Riley dip map at 1981 on time axis. P=143, T=1981.

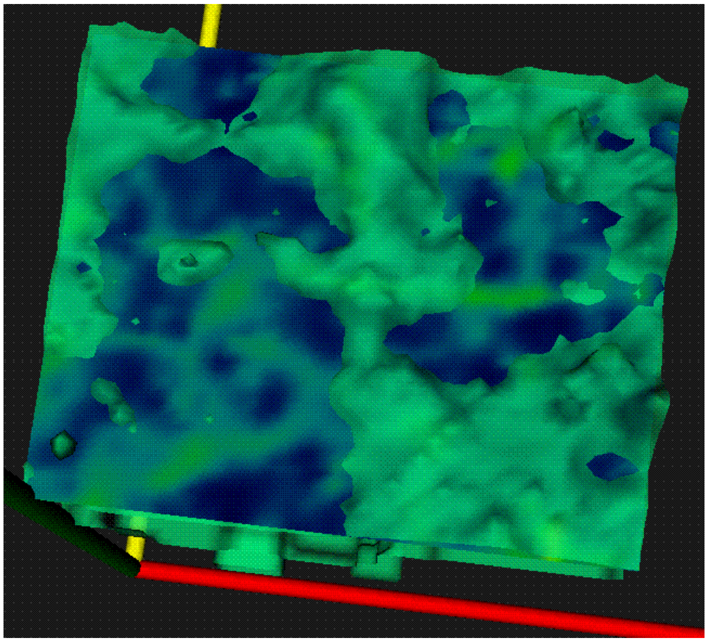

Figure 8.3.11. Panoma (Council Grove) with Fort Riley dip map at 1983. P=143, T=1983.

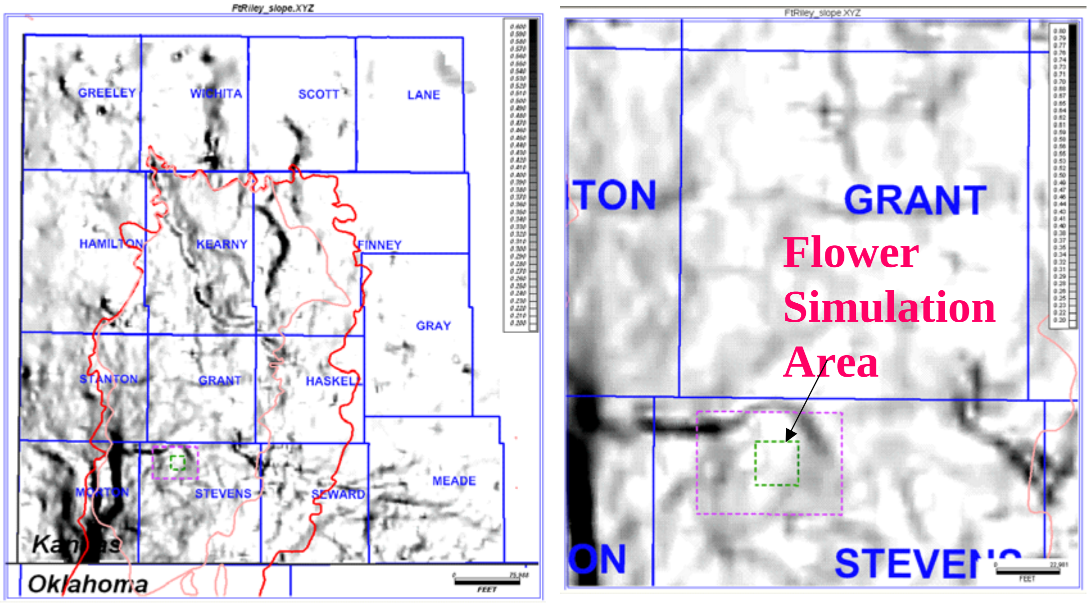

Figure 8.3.12 First derivative of Fort Riley structure map of Kansas Hugoton area and enlarged portion around Flower simulation area. Areas of steep dip are dark lineaments that may be associated with basement faults and fractures.

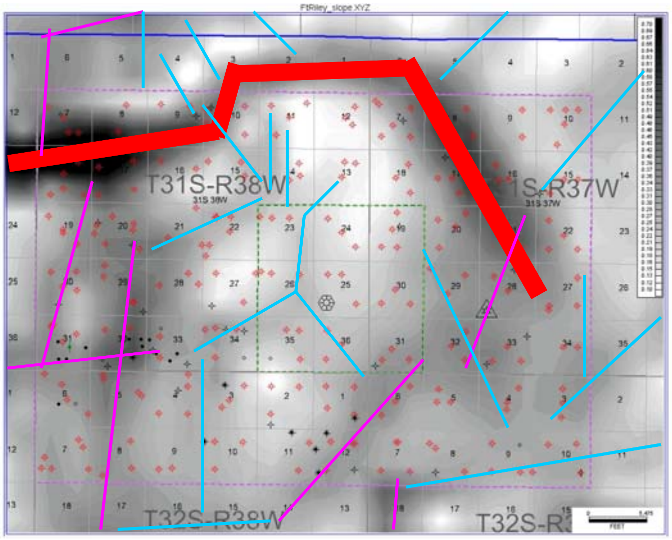

Figure 8.3.13. Panoma (Council Grove) with Fort Riley dip map at 1983.

Figure 8.3.14. Open vertical fracture in core slab of Krider core, Flower A1 well in Stevens County, Kansas.

Figure 8.3.15. Regularly spaced joint system in Silverdale member quarry, Fort Riley Limestone Member, in southeast Kansas.

8.4 DIFFERENTIAL DEPLETION OF RESERVOIR PRESSURE – SIMULATION STUDIES

Saibal Bhattacharya

One single-section and three multi-section simulation studies were carried out in this project and have been detailed in Section 9. Figure 8.4.1 shows the simulator-calculated pressure distribution within a 640-acre area around the Alexander D1 (Chase Parent) and Alexander D2 (Council Grove) wells as of February 1991, i.e., before the onset of production from the Chase Infill well (Alexander D3) drilled in the same section. This pressure distribution was obtained after matching production and pressure histories at the Alexander D1 and D2 wells and confirming that the model had no excess-flow capacity. Figure 8.4.1 shows that different layers in the Chase and Council Grove reservoirs have depleted by varying degrees.

Figure 8.4.2 displays the simulator-calculated pressure distribution in the area simulated around the Flower A1 well (sec. 25, T. 31 S., R. 38 W.) as of January 1970, i.e., before the onset of production from the Council Grove well drilled in the same section. Figure 8.4.3 shows simulator-calculated pressure distribution in the same area as of January 1995. Both the above figures represent simulation results after history matching available production and pressure data from Chase Parent, Council Grove, and Chase Infill wells drilled in this nine-section area. These results indicate that Chase and Council Grove layers are differentially depleted as a result of production and confirms observations reported by Fetkovich et al. (1994) and Oberst et al. (1994). However, critical differences exist between our current study and multi-section simulation studies carried out by these authors. Unlike previously reported simulation studies, our study has modeled the Chase and the Council Grove reservoirs as one system allowing crossflow between adjacent layers based on vertical permeabilities estimated from available core data. Figures 8.4.4A and 8.4.4B compare the simulator-calculated layer pressure at the location of the Flower A1 well with that recorded by layer-specific DST tests carried out at this well as of January 1995. Figure 8.4.4A shows close matches between simulator-calculated and layer-DST pressures for all but three layers (pairs circled) when completions at the Chase wells were constrained to Chase layers while those at the Council Grove wells extended up to Krider (Layer 2 in the Chase reservoir). However, when completions at the Chase wells were extended to B5 Lime (Layer 23 in the Council Grove reservoir) keeping Council Grove completions extended to Krider, the match between the simulator-calculated layer pressure and the layer-DST recordings improved for two of the three layers (refer Figure 8.4.4B), where a close match had not been obtained earlier. The layer-DST pressures recorded at the Flower A1 well confirm the presence of differential depletion in the Chase and Council Grove reservoirs in the Hugoton and Panoma fields.

Figure 8.4.5 displays the simulator-calculated pressure distribution in a twelve-section area around the Hoobler Estate Unit well (sec. 20, T. 6 N., R. 17 E.) after history matching well performance. Simulation results indicate differential pressure depletion in the Chase reservoir. Unlike the Flower area, the Hoobler area is located outside the Panoma field and on the edge of the “other” Council Grove production area, and, thus has no producing Council Grove wells. Figure 8.4.6A plots the decline in the simulator-calculated pore-volume-averaged layer pressures for select pay zones in the Chase reservoirs in the modeled area. Starting from a constant initial-reservoir pressure, different layers deplete at varying rates. Figure 8.4.6B compares the simulator-calculated average reservoir pressure as of May 2006 with corresponding layer pressures (best) estimated from layer-specific RFT data recorded at wells within and around this study area. Good match between simulator-calculated layer pressures and those estimated from RFTs confirm the validity of differential depletion observed in simulation results.

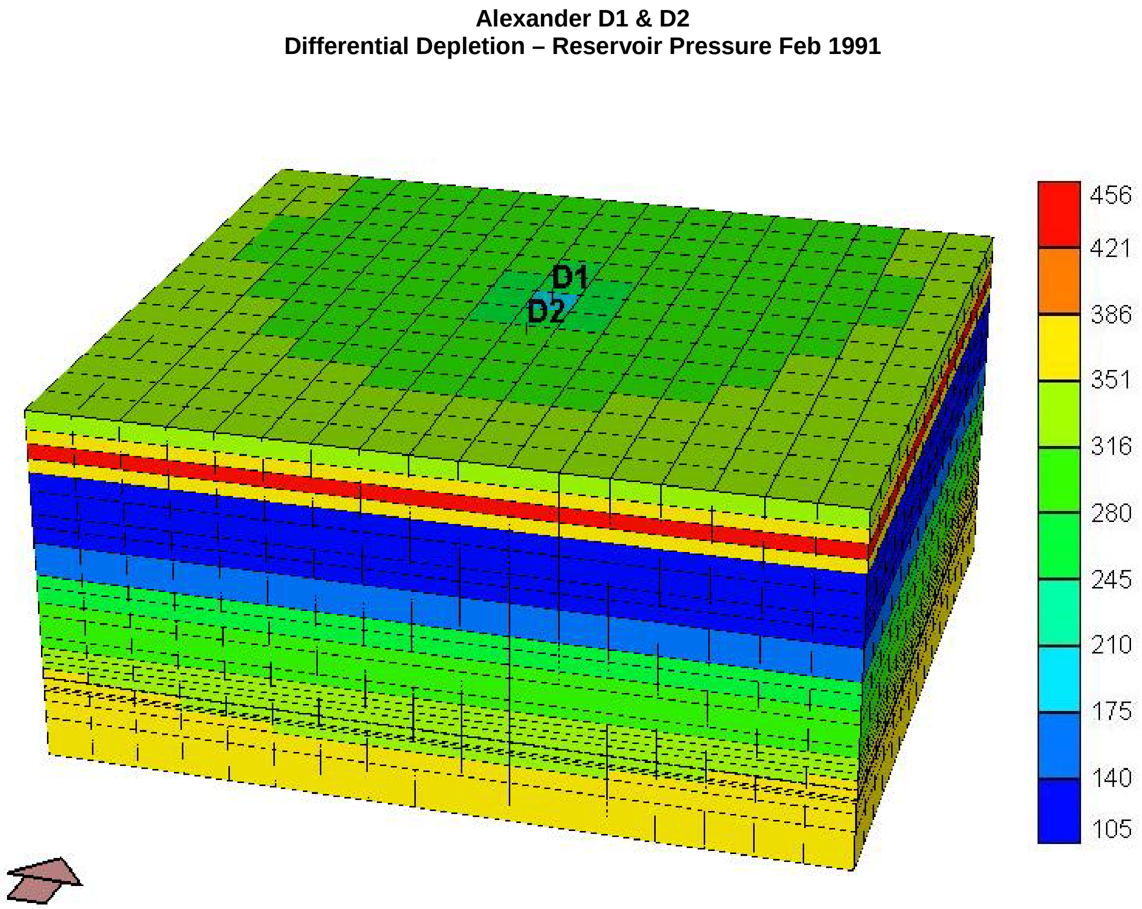

Figure 8.4.1. Simulator-calculated pressure distribution in the 640-acres around the Alexander D1 and D2 wells after well history match showing layers depleting at varying rates.

CG Fractures extend to L2 & Pi = 423 psi, OGIP = 179.5 bcf

Flower Area
Differential Depletion – Reservoir Pressure Jan 1970
(before CG wells came online)

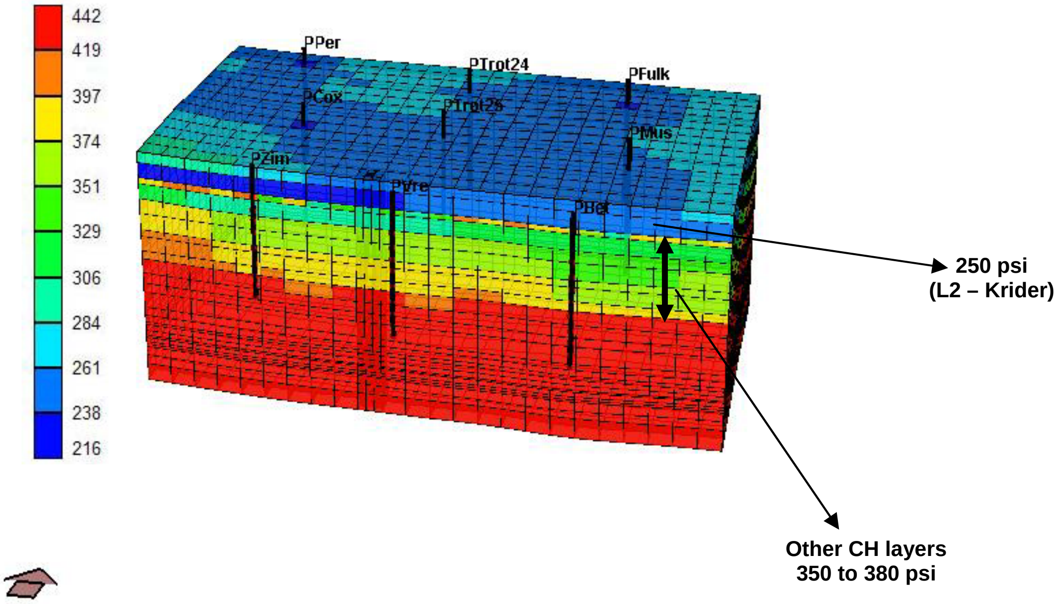

250 psi
(L2 – Krider)

Other CH layers
350 to 380 psi

Figure 8.4.2. Simulator-calculated pressure distribution in the Flower study area as of January 1970 showing differential depletion.

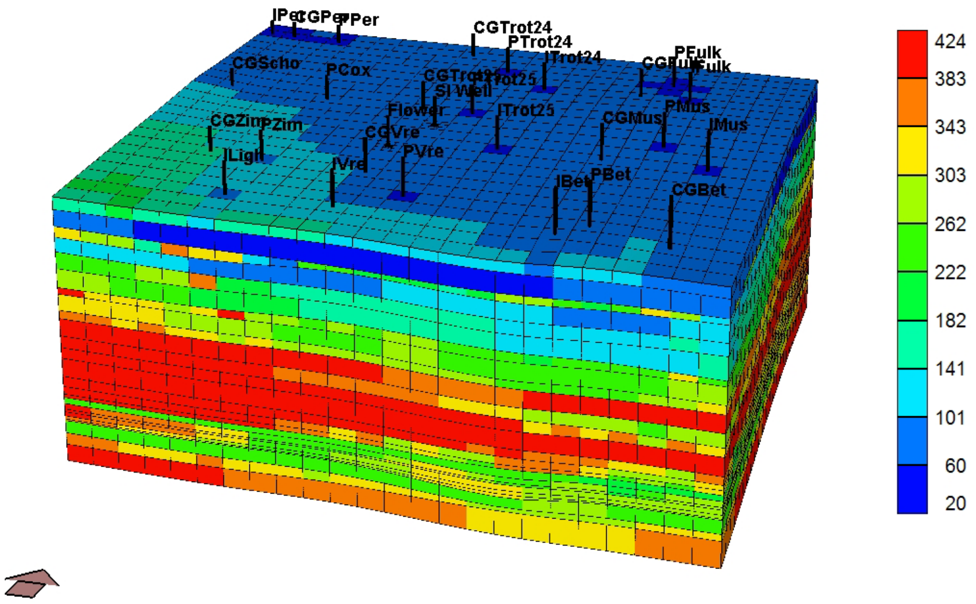

CG Fractures extend to L2 & Pi = 423 psi, OGIP = 179.5 bcf

Flower Area
Differential Depletion – Reservoir Pressure Jan 1995

Figure 8.4.3. Simulator-calculated reservoir pressure distribution in the Flower study area as of January 1995 shows differential depletion and confirms layer-specific DST pressures recorded at the Flower A1 well.

A.

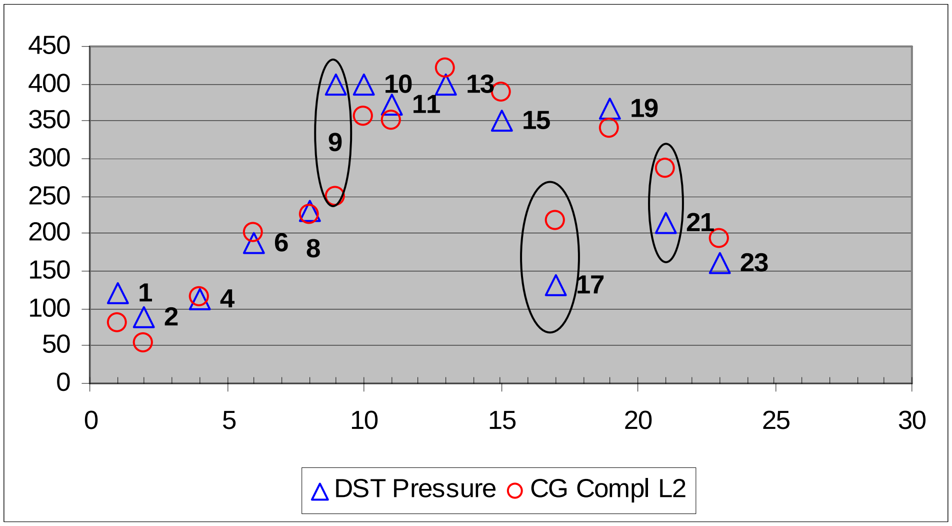

B.

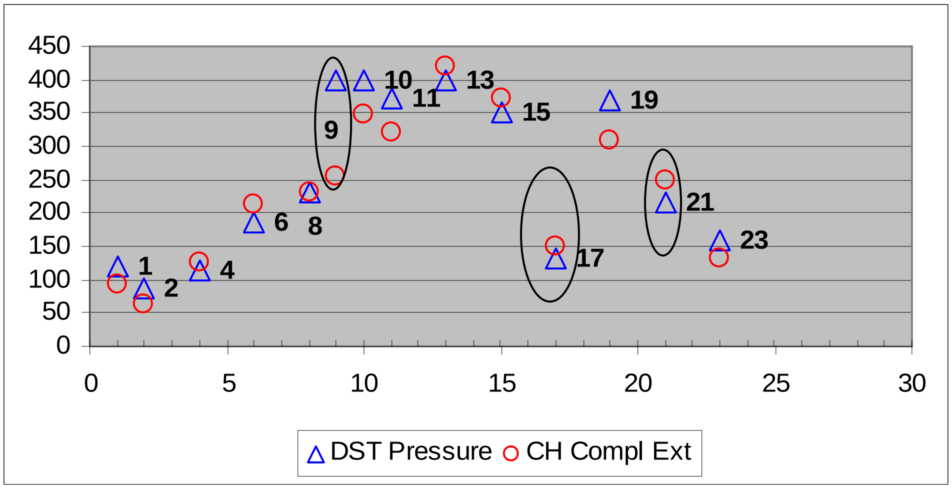

Figure 8.4.4. Comparison between simulator-calculated layer pressure at the location of the Flower A1 well with layer-specific DST pressures as of January 1995. **A)** Results when Chase wells were completed within Chase while completions in Council Grove wells were extended to Krider. **B)** Results when Chase wells were completed to B5 Lime while Council Grove completions were extended to Krider. Match between simulator-calculated layer pressure and layer-specific DST improved when Chase completions were extended into Council Grove.

Hoobler Area
Differential Depletion – Reservoir Pressure May 2006

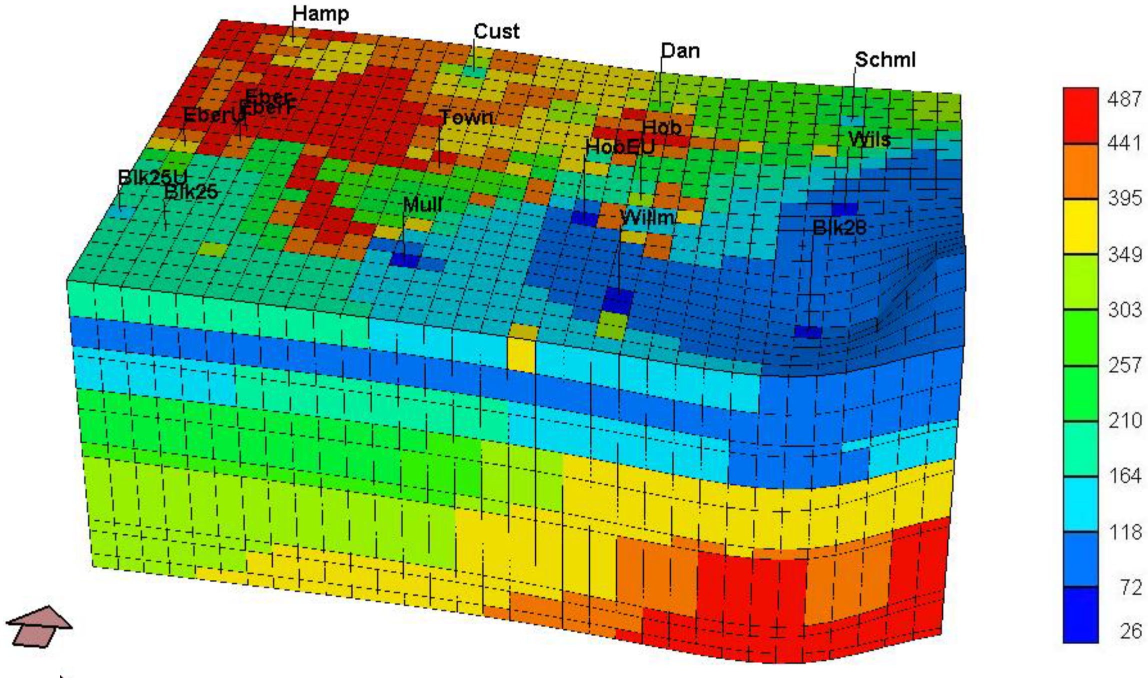

Figure 8.4.5. Simulator-calculated differential depletion in Chase layers in the Hoobler study area as of May 2006 due to production from the Chase wells.

A.

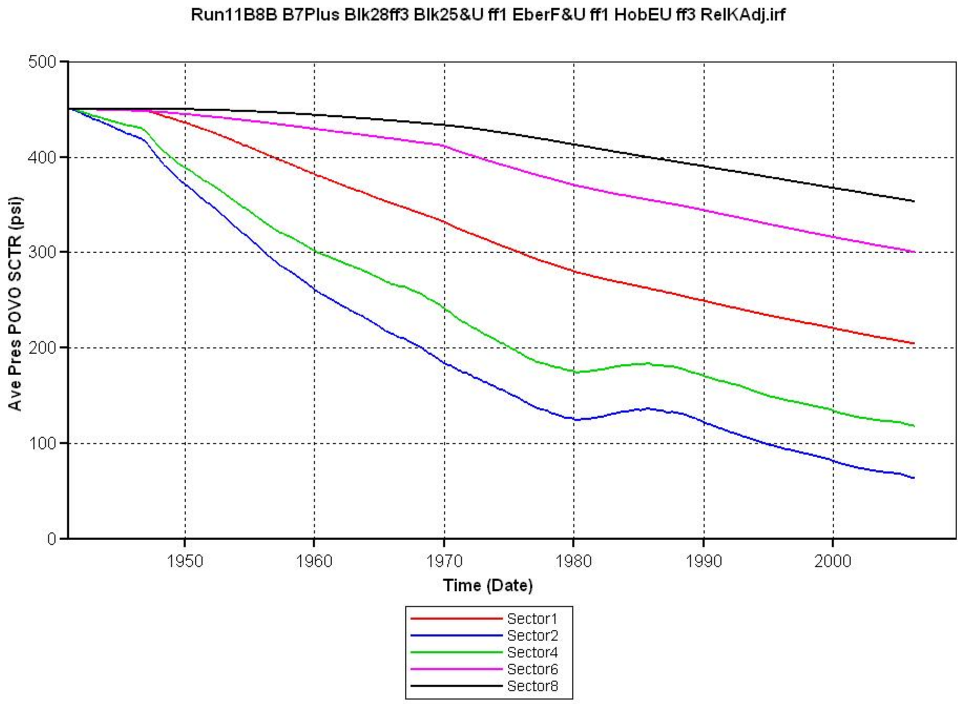

B.

	RFT, psi	PV Avg Sim psi @ May 2006
Herrington	200 +	204
Krider	40 to 60	63
Winfield	40 to 60	118
Towanda	150 to 300	300
Ft. Riley	450	353

Figure 8.4.6. A) Simulator-calculated (pore-volume) average pressure in select pay layers in the Chase reservoir in the Hoobler study area shows layers depleting at different rates. **B)** Comparison between simulator-calculated average reservoir pressure (as of May 2006) and (best) estimated pressures from corresponding RFT recorded in key productive horizons in the Chase reservoir shows good match and thus validates simulator results regarding differential depletion.

8.5 HYDRAULIC FRACTURES

Robert E. Barba and Martin K. Dubois

Modeling Hydraulic Fractures, Hugoton and Panoma Fields, Southwest Kansas

Abstract

Hydraulic fracturing of the thinly layered reservoir system is a common practice in the Hugoton and underlying Panoma fields in Kansas. After perforating and acidizing multiple zones (as many as six), all zones are typically fracture treated with one or two large treatments. Understanding communication between zones and, potentially, between fields, whether by natural means or by introduced hydraulic fractures, is critical to understanding reservoir performance and estimating remaining gas in place. This study simulates hydraulic-fracture treatments typical of a small region in a generic rock-mechanical model. The model is based on limited core data, rock mechanical data and reservoir condition information, some of which was estimated. Results of simulations suggest that hydraulic-fracture treatments in the Chase Group zones (Hugoton) do not extend downward appreciably, whereas, hydraulic fracture treatments in the Council Grove (Panoma) probably extend upward into the Chase Group, which directly overlies the Council Grove. Additional measured properties would increase our confidence in the model and simulation.

Introduction

Little is known about the geometry of the hydraulic fractures in nearly 12,000 wells in the Hugoton and Panoma wells in Kansas and Oklahoma. It has been suspected that Council Grove wells may be in communication with the shallower Chase interval but not necessarily the converse (Ford, 1982; Bhattacharya et al., 2005). The limited published work on hydraulic fractures in the Hugoton and Panoma deal primarily with techniques intended to reduce the problem of fractures extending vertically beyond the optimal limits (e.g.: Hecker and Downie, 1996) but do not discuss the resultant geometry of the fractures induced by the majority of fracture treatments either from direct or indirect measures or from models and simulations. We built a generic rock-mechanical model and simulated hydraulic fractures common to a small area (Figure 8.5.1) in the central portion of the field to evaluate the most likely geometry of hypothetical fractures. A three-step workflow was employed:

1. Build a rock-mechanical model based on continuous core and associated petrophysical data from the Flower A1 well, and critical rock properties and parameters measured or derived from nearby wells.
2. Estimate reservoir conditions at the time of the fracture treatments by utilizing measured properties, when available, or properties from reservoir-simulation results.
3. Simulate four classes of hydraulic-fracture treatments typical of the region using the MFRAC P3D hydraulic-fracture-modeling software (Meyer, 2003).

History of Hydraulic Fractures in Hugoton and Panoma

Hydraulic fracturing has been used in the Hugoton field since 1949 and in the study area since 1960. Up until the 1960’s, wells were generally open-hole completed in the upper Chase and acidized with up to several tens of thousands of gallons of acid. These early wells (Hugoton “parent” wells) were eventually stimulated by hydraulic fractures in the 1960’s, a date that coincides with the beginning of Council Grove (Panoma) development. All except the very initial Panoma wells and the later Chase wells (Hugoton replacement and “infill” wells) were perforated through casing. Multiple-zone completions are the norm with acidization of each zone separately with up to several thousand gallons preceded large single fracture treatments over the entire interval of 100 to 200 ft. Fracture treatments described in this paper, 100-200 thousand pounds of sand and 100-200 thousand gallons of treated water in roughly the same proportions, are typical of the field during the 1960’s to early 1980’s. However, Hecker et al., (1995) reported it was not uncommon for treatment sizes to increase to 300-500 thousand pounds of sand and 80,000- 90,000 gallons of crosslinked fluid. These treatments are much larger than those utilized in the study area. Hecker and Downie (1996) report that changing treatment strategies in Chase infill wells by substantially reducing fracture treatments from 450 thousand pounds of sand used in the early 1990’s to 100,000 pounds of sand and 30,000 gallons of crosslinked fluids reduced the length of downward migration into water-bearing zones. Though not specifically stating it, the implication was that undesirable fracture heights were a problem with the larger fracture treatments.

Critical Data and Methodology

The most critical input to modeling hydraulic fractures is the *in-situ* stress distribution. Other important rock properties include Young’s modulus, Poisson’s ratio, pore pressure, and fracture toughness. The P3D model estimates the stress induced by the hydraulic fracture and estimates the vertical and lateral growth of the fracture based on the interaction of the induced stress with the *in-situ* stress distribution. The stress induced by the hydraulic fracture (net pressure) is a function of injection rate, fluid viscosity, and the height of the system. The injection rate in the fracture is a function of the rate entering the perforations minus the rate leaking off into the formation. Along with the created geometry, the P3D models estimate the proppant distribution during the fracture treatment and at fracture closure.

Closure stress can be estimated directly from a pump-in test at fracturing rates. The pressure at which the fracture closes (closure stress) can be measured directly from plots of bottomhole pressure vs. time. Numerous studies have shown that this closure stress can be estimated from a combination of reservoir pressure and log-derived rock properties data. The relationships for all of the critical rock-properties inputs are presented in the “Rock-properties Data” section below. The majority of the data for the study were obtained from the Flower A1 well in sec 25, T. 31 S., R. 38 W. The well was drilled in 1994 as a “science” and observation well in an underbalanced condition (foam as a drilling fluid). Each zone was cored and tested by drill-stem test (DST) separately and a comprehensive open-hole log suite was run. The generic geologic and rock model is based directly on the properties derived from this well's dataset or estimated in adjacent wells through property transforms on measurements taken in adjacent wells.

Analysis Methodology

Steps employed to model the hydraulic-fracture treatments include:

1. Review previous hydraulic fracture, rock-properties, and field studies conducted in Hugoton (Chase) and Panoma (Council Grove).
2. Utilize full-wave sonic data (Flower A1 and 3 offset wells with dipole sonic data) to develop a correlation to Flowers area using common log suites.
3. Review fracture-treatment data for the major development periods and establish four classes of treatments based primarily on timing and stratigraphic interval.
4. Obtain rheological properties from historical service-company data books.
5. Develop log-based mechanical-properties model for type well (Flower A1 observation well)-Poissons ratio, Young's modulus, Biot's constant, and fracture toughness. Use Flower A1 well for primary input supplemented with coherent data from other three wells with dipole-sonic data.
6. Calibrate log-based mechanical-properties model to field-pressure data where bottomhole-pressure data were available.
7. Calibrate fluid-efficiency model as a function of log data, fluid type, and reservoir pressure from measured bottomhole-pressure data in selected zones from the 28 well study area.
8. Simulate fracture treatments for each of the four classes with various fluid systems used in that period.
9. Provide best estimates of fracture geometry for each treatment type in each of the four classes based on fracture-treatment pressure matches.

Rock Properties Model

One objective of the rock-property model is to estimate closure stress, which is done here from log data because no measured data are available. The relationship proposed is that in Baree and Conway (1998):

$$\sigma x \text{ min} = (\nu/1-\nu)\ (\sigma z - \alpha(PPG) + \varepsilon E \qquad (1)$$

Where: σx min = Closure-stress gradient (psi/ft)
σz = Overburden gradient (psi/ft)
ν = Poisson's ratio
α = Biot's constant
PPG = Pore-pressure gradient (psi/ft)
ε = Tectonic strain (microstrains)
E = Young's modulus psi E6

A key component of the above relationship is Poisson' ratio (ν). Poisson's ratio can be estimated from shear and compressional transit-time data using the following relationship from Newberry et al. (1985):

$$\nu = [(0.5*(\Delta TS/\Delta TC)_2-1]/[(\Delta TS/\Delta TC)_2-1] \qquad (2)$$

Where:

DTS = Delta T shear (microseconds/ft)
DTC = Delta T compressional (microseconds/ft)

Young's modulus can be estimated from the following relationship:

$$E=2*(13400*(\rho b/\Delta TS_2)+(1+\nu)) \qquad (3)$$

The pore-pressure history of the study area by zone was provided by history-matched reservoir simulation studies (Bhatttacharya et al., 2005). Three constraints on the pressure history are the original pore pressure of 460 psi, measured bottomhole pressures by DST from the Flower A1 well in 1994, and bottomhole pressures from repeat formation tests in a nearby well in 2005. Simulation-model pressures were assigned for the main producing zones, depending on the year of the fracture treatment. Intervening impermeable layers were assigned 422 psi, the initial pore pressure assigned in the simulation model. Overburden gradient was estimated from bulk density log data from the Thurow 1B well in sec. 15, T. –31 S., 37 W. near the study area, and determined to be 1.03 psi/ft in the zones of interest. A plot of overburden gradient vs. depth is provided as Figure 8.5.2.

Discussion of Rock-properties Model

Potential error due to inaccurate data must be eliminated and gaps in data estimated (Barba and Batcheller, 2006). The dipole sonic tool has inherent errors from thin beds, depth matching, and borehole irregularities. Coherence curves (CHRP and CHRS for the Schlumberger DSI tool) provide an avenue for checking the quality of the data. Figures 8.5.3-6 show the coherence curves for the Chase and Council Grove intervals for the Flower A1 and Youngren 1 wells. While there is a significant amount of incoherent data, there is a representative sampling of coherent data that provides critical calibration intervals and reasonable correlation over the range of rock types and facies in the study.

Gas affects both the shear and compressional data; however, the effect on the shear data is greater. The result is an abnormally low Poisson's ratio. Gas does not affect the coherency of the data, and it must be detected using other means. Poisson's ratios have a characteristic response in known lithology, a property available from core X-ray diffraction (XRD) data in the Flower A1 well. Typical values for Poisson's versus lithology are shown in Table 8.5.1. A comparison of the quality data points from the dipole in non-gas-affected zones and the XRD-lithology-based Poisson's with U matrix apparent from the litho-density data provided a reasonable correlation. The grain density for the U matrix apparent was evaluated using core–derived grain density. The relationship is shown in Figure 8.5.7.

The wireline-log-density input to both the U matrix apparent and Young's modulus estimate was crosschecked against the core-grain density and porosity measurements. This was useful in the zones with rugose hole and severe gas effect. A core-based bulk density was developed as an editing tool from Schlumberger well services (1995) using the relationship below:

$$\rho b=\rho gcore^{*}\ (1-\Phi core)+\rho f^{*}-\Phi core \tag{4}$$

The photoelectric-effect curve (PEF) was edited in selected areas using the XRD and core-lithology descriptions.

Young's Modulus Estimation

While the data-editing process improved the quality of the rock properties, an additional quality-control method for Young's modulus was implemented. Young's modulus is a function of lithology and porosity (Equation 3), and accurate porosity and lithology data are available in the core. An additional correction factor that transforms the field-derived dynamic Young's modulus to a static Young's modulus is necessary. The link between rock type in a previous rock-mechanics paper (Yale and Jamieson, 1994) and that defined in core in the Flower A1 facies provided a good alternative for obtaining a static Young's modulus that they tied to rock-mechanical facies (Table 8.5.2a). Our 11 rock lithofacies (Figure 8.5.8) were lumped and correlated with their six rock mechanical facies (Table 8.5.2b). An excellent correlation between core porosity and static Young's modulus by transformed lithofacies was obtained (Figures. 8.5.9-15).

Integrated plots of all petrophysical and rock properties for the 3D-model input are shown in Figures 8.5.16-20. Computed outputs displayed on the plots and their source include:

VCL = Non-linear clay volume from Petcom algorithm
ClayX = XRD-clay volume
RHOGCORF = Grain density from core
RHOMAND = Grain density from neutron-density crossplot
Pef/UMAA = U matrix apparent (from Pef and electron-density product)
PRUMAA = Poisson's ratio from UMAA correlation
DCHRDIP = Dipole-coherence flag (green=coherent data)
DPRFINAL = Poisson's ratio from dipole (QC layers only)
EMOD = Youngs modulus from Mobil facies and core porosity
PRXRDV = Poison's ratio from XRD mineralogy
CorSwf = Core Sw
SWQ = Computed water saturation
Kfinl = Effective permeability from KGS model

KCORNOB = NOB Klinkenberg core permeability
RHOBRG = Bulk density from core-grain density and core porosity
DSDTP = P-wave sonic-transit time
DDTS = Shear-wave sonic-transit time
NPHILP = Neutron porosity
PHICORF = Core NOB porosity
PHICDF = Porosity from KGS model
PHIEQ = Calculated effective porosity
BVWQ = Calculated bulk-volume water
XRD = Mineral distribution from core XRD analysis
Petcom 5 min = 5-mineral analysis from Petcom

Rock Properties and Fluid-loss Model Calibration

Pump-in test data are not available in the immediate study area, but microfrac and minifrac test data in similar Chase Group reservoirs in Texas County, Oklahoma were reviewed. We assumed that leak-off properties would be similar as a function of permeability and that the tectonic offset would be reasonably similar. The microfracs and minifracs were measured with downhole-quartz gauges. However surface shut-in was used and wellbore storage effects made the data unusable for detailed leak-off calculations. Stress data obtained were similarly weak, however it could be ascertained that there were no major tectonic strain effects on the *in-situ* stress measurements. An example of one of the microfrac tests is shown in Figures 8.5.21 and 8.5.22. While the conventional closure-analysis plots (Figure 8.5.21) indicated an event that was originally interpreted as closure, the unit slope on the log-log plot (Figure 8.5.22) indicates wellbore storage was a factor. In microfrac and minifrac analysis a quality dataset will have a log-log half slope for fracture linear flow, quarter slope for bilinear flow, and ideally a flattening of the slope after fracture closure and pseudoradial flow. None of the datasets had these flow regimes present due to the wellbore-storage effects. The recommendation was made for future tests to use a downhole shut-in tool for any tests in the future.

Leak-off Parameter Estimation

The analytical model in MFRAC was used to estimate fluid efficiency from key reservoir and frac parameters. While the Keenan A5 test data were not quantitatively acceptable, they did suggest that the leak-off coefficients would be at the high end of the spectrum (greater than 0.005 ft/min$^{0.5}$). This is consistent with permeabilities in the 1-md range and reservoir pressures in the 200-psi range (vs. a minimum of 1500-psi fracture extension pressures). The MFRAC dynamic leak-off model uses the following static inputs for estimating leak-off coefficients:

1. Reservoir permeability, porosity, and pressure
2. Wall-building coefficient
3. Frac fluid and reservoir fluid viscosity

4. Reservoir compressibility

The MFRAC model uses these static inputs to dynamically model fluid flow from the fracture to the formation based on the rock properties and fluid rheology during the treatment. While additional work is recommended to validate the resultant leak-off coefficients with measured bottomhole data, the model provides the “best available” estimate in the absence of these measured data.

Hydraulic-fracture Classes

Four classes of hydraulic fractures were defined primarily on the basis of the time period of the treatment and stratigraphic interval treated; 1960 Chase parent, 1969 Chase parent, 1969 Council Grove, and 1987-88 Chase infill. Although drilled and completed in the 1950’s, the Chase “parent” wells (Hugoton) were not fracture treated until 1960 in the study area, and only one of the study wells in that year. The balance of the Chase parent wells was fraced in 1969. Council Grove wells (Panoma), one per section, were all fraced upon completion in 1969, and all Chase infill wells (1987-88) were also fraced upon completion. The only rock mechanical-model variable that changes with the fracture simulations is the zonal pressures derived from the earlier-mentioned simulation models. In these models we assumed that there was some withdrawal of gas from the Council Grove before well completions in that interval because wellhead shut-in pressures in the Council Grove in this area and across the field were already below the original pressure when initially completed.

1960 Chase Parent Well Fracs

The one Chase parent well fraced in 1960 was an openhole slotted liner completion with 7-inch casing set at the top of the Hollenberg and the liner run from there to total depth (TD) in the lower Fort Riley, 71 ft above the top of the Wreford. The treatment consisted of 120,000 pounds of proppant pumped with 100,000 gallons of “slick water.” The rate was not included in the report but typically the subsequent fracs were treated at 150 to 300 barrels per minute (BPM). Both high and low rates were modeled to determine a range of possible frac geometries. Rock- and fluid-properties tables used for this simulation are shown in Tables 8.5.3-6 and simulation outputs are shown in Figures 8.5.23-30. The most likely bottom limit of fracture conductivity at the higher rate (300 BPM) is the base of the Towanda zone. It is not likely that the treatment reached the Council Grove.

1969 Chase Fracs

Eight Chase parent wells were fraced in 1969. Typical completion included the setting of 7-inch casing set at the top of the Hollenberg and a slotted liner set from that point to TD approximately 80 ft into the Fort Riley, but not down to the Wreford. Typical treatments consisted of 180,000 pounds of proppant pumped with 150,000 gallons of slick water pumped at 300 BPM. Rock- and fluid-properties tables used for this simulation are shown in Tables 8.5.7-10, and simulation outputs are shown in Figures 8.5.31-33. The most likely bottom limit of fracture conductivity at the higher rate (300 BPM) is again the base of the Towanda zone. It is not likely that the treatment reached the Council Grove.

1969 Council Grove Fracs

Five Council Grove (Panoma) wells fraced when completed in 1969. Typical completion included 5 ½-inch casing set to the base of the Council Grove with perforations in six Council Grove zones from the B5_LM upward. A typical treatment consisted of 100,000 pounds of proppant pumped with 126,000 gallons of "slick water" pumped at 162 BPM. Rock- and fluid-properties tables used for this simulation are shown in Tables 8.5.11-13, and simulation outputs are shown in Figures 8.5.35-37. It is highly likely that the Council Grove fracture treatments propped into the Chase Group. The precise vertical extent of the penetration cannot be refined without measured bottomhole pressures; however, the estimated growth with the parameters used is the lower portion of the Towanda zone. It is highly probable that the Fort Riley and Wreford zones were contacted by the Council Grove fracture treatments and should thus be in hydraulic communication with the Council Grove.

1987 Chase Infill Fracs

Eight Chase infill wells fraced when completed in 1987 or 1988. Typical completion included 5 ½-inch casing set to the base of the Chase with perforations in all six Chase zones. A typical treatment consisted of 250,000 pounds of proppant pumped with 100,000 gallons of cross-linked gel pumped at 60 BPM. The estimated pressure data from the 1990 reservoir simulation ere used for the frac simulations. Rock- and fluid-properties tables used for this simulation are shown in Tables 8.5.14-17, and simulation outputs are shown in Figures 8.5.38-41. The most likely maximum extent of fracture conductivity is restricted to the perforated intervals (Chase), with the majority of the treatment going into the thicker lower-pressure zones in the upper Chase. It is not likely that the treatment reached downward into the Council Grove.

Summary

The objective of this study was to determine the most likely vertical extent and overall geometry of the historic hydraulic-fracture treatments in the study area. Due to the significant depletion from the early-unfractured production the thick, permeable upper Chase members most likely received the majority of the stimulation during all Chase fracture treatments. It is unlikely that any Chase treatments communicated with the Council Grove. Conversely, it appears likely that the 1969 Council Grove fracture treatments extended into the Fort Riley and Towanda zones in the lower to mid-Chase, at a minimum. Key to the conclusions are the basic assumptions that went into the model. Pressures were estimated by a combination of direct measurements and history-matched reservoir-simulation models. Because pressures are a major control on fracture geometry, variations from those projected would affect the geometry of the fractures. If pressures had been significantly lower in the Council Grove upon completion, the fracture treatments might not have migrated upward as far. However, the pressure data used are consistent with those measured directly after completion. Perhaps the most loosely constrained variables are *in-situ* stress and fluid-leak-off properties. Direct measurements of these properties would add confidence to the modeling and simulation.

Understanding hydraulic-fracture geometries may provide clues to communication between zones and possibly fields that help explain production histories. The subject study suggests that conclusions from the earlier simulation study that the Council Grove wells may be communicated with the Chase interval but not necessarily the converse may be valid (Bhattacharya et al., 2005).

References

Barba, R. E. and G. W. Batcheller, 2006, Best practices for well completions using the completion efficiency process: short course workbook.

Baree, R., and M. Conway, 1998, hydraulic fracturing technology: course workbook.

Bhattacharya, S., M. K. Dubois, A. P. Byrnes, J. H. Doveton, and G. C.Bohling, 2005, Reservoir engineering studies in Hugoton-Panoma systems: (abs): American Association of Petroleum Geologists Midcontinent Section Meeting, Oklahoma City, Oklahoma, p. 31. Also online http://www.kgs.ku.edu/PRS/Poster/2005/MidcontAAPG/6_Bhattacharya_simulation_MCaapg05.pdf (accessed June 12, 2006).

Dubois, M. K., A. P. Byrnes, T. R. Carr, G. C. Bohling, and J. H. Doveton, *in press*, Multiscale geologic and petrophysical modeling of the giant Hugoton gas field (Permian), Kansas and Oklahoma, in P. M. Harris and L. J. Weber, eds., Giant reservoirs of the world: From rocks to reservoir characterization and modeling: American Association of Petroleum Geologists, Memoir 88.

Ford, J. D., 1982, Historical and reservoir engineering study of the Panoma Council Grove field in Wichita, Finney, Kearny, Hamilton, Haskell, Grant, Stanton, Seward, Stevens and Morton counties, Kansas: Society of Petroleum Engineers, paper, SPE 11667, 31 p.

Hecker, M. T., M. E. Houston, and J. D. Dumas, 1995, Improved completion designs in the Hugoton field utilizing multiple gamma emitting tracers: Society of Petroleum Engineers, Annual Technical Conference and Exhibition, Dallas, TX, Paper SPE 30651, p. 223-235.

Hecker, M. T. and R. C. Downie, 1996, Process changes improve fracture treatment designs in the Hugoton field: Society of Petroleum Engineers, Annual Technical Conference and Exhibition, Calgary, Alberta, Paper, SPE 35259, p. 93-101.

Meyer, B. R., 2003, MFRAC-II Hydraulic Fracture Model Users Manual: Meyer and Associates, Natrona Heights, PA 2003.

Newberry, B. M., R. F. Nelson, and U. Ahmed, 1985, Prediction of vertical hydraulic fracture migration using compressional and shear wave slowness: Society of Petroleum Engineers, SPE/DOE Symposium on Low Permeability Reservoirs, Denver, CO, paper SPE 13895.

Schlumberger Well Services, 1995, Log interpretation charts, chart Por-5: Schlumberger Wireline and Testing, Houston, TX.

Yale, D. P. and W. H. Jamieson, 1994, Static and dynamic rock properties in the Hugoton and Panoma fields, Kansas: Society of Petroleum Engineers, Mid-Continent Gas Symposium, Amarillo, TX, paper SPE 27939, p. 209-219.

Tables:

Mineral	Poisson's Ratio
Quartz	0.18
Dolomite	0.29
Calcite	0.31
Anhydrite	0.32
Shale	0.30

Table 8.5.1 Poisson's ratio by mineralogy.

A

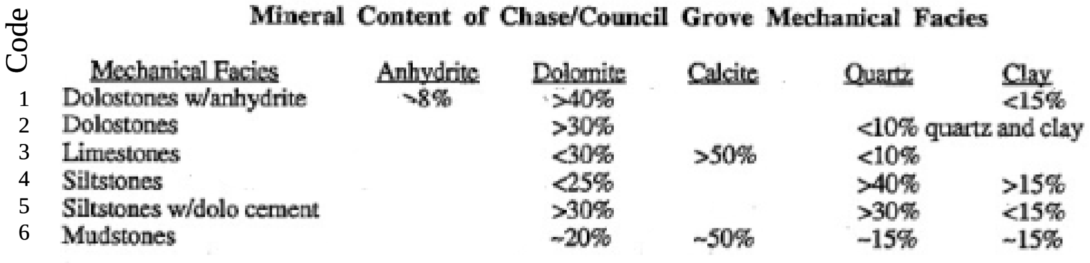

Mineral Content of Chase/Council Grove Mechanical Facies

Code	Mechanical Facies	Anhydrite	Dolomite	Calcite	Quartz	Clay
1	Dolostones w/anhydrite	~8%	>40%			<15%
2	Dolostones		>30%		<10% quartz and clay	
3	Limestones		<30%	>50%	<10%	
4	Siltstones		<25%		>40%	>15%
5	Siltstones w/dolo cement		>30%		>30%	<15%
6	Mudstones		~20%	~50%	~15%	~15%

B

Mechanical Facies Code	**Dubois, et al. (2006) lithofacies classification**
1	L6 or L9 with anhydrite
2	All other L6 and L9
2	L4, 5, 7, 8 with grain density >= 2.76
2	L10 with grain density>= 2.74
3	Other L4, 5, 7, 8 with low clay content
4	L1, 2, 3 and grain density < 2.74
5	L1, 2, 3 and grain density >= 2.74;
5	L10 and grain density < 2.74
6	L4, 5, 7, 8 with high clay content

Table 8.5.2 (A) Rock-mechanical facies classification (after Yale et al., 1994). We assigned a numeric rock code (1-6), 1- dolostones w/ anhydrite, 2- dolostones, 3- limestones, 4- siltstones, 5- siltstones w/ dolomitic cement, and 6- mudstones.
(B) Yale et al. (1994) mechanical facies correlated to lithofacies in Dubois et al. (*in press*).

Simulation Pass-1960 Pressures
Original Pressure 422

Model Layer	Zone	Top Depth	Layer h	Layer K*	Layer Kh	Reservoir Pressure	Compress-ibility	Porosity
1a	HOLLENBRG	2450	22.5	0.01	0.225	317	0.0115	0.0691
1	HRNGTN	2472.5	22.5	5.668	128	317	0.0115	0.0815
2	KRIDER	2495	40.5	90.30	3657	296	0.0109	0.1593
3	ODELL	2535.5	13.5	0.017	0.230	372	0.0134	0.0742
4	WINF	2549	35.5	7.60	270	380	0.0137	0.1192
5	GAGE	2584.5	33.5	0.064	2.14	408	0.0150	0.0959
6	TWND	2618	38	1.666	63.3	409	0.0150	0.1280
7	B/TWND	2656	18	1.859	33.5	412	0.0151	0.1188
8	FTRLY	2674	32	0.948	30.3	413	0.0152	0.1242
9	L_FTRLY	2706	24	0.019	0.456	417	0.0154	0.0818
10	B/FTRLY	2730	33	0.039	1.287	422	0.0156	0.0752
11	WREFORD	2763	26	0.5	13.0	421	0.0155	0.0851
12	A1_SH	2789	22	0.001	0.022	422	0.0156	0.0765
13	A1_LM	2811	37	0.023	0.851	422	0.0156	0.0729
14	B1_SH	2848	17	0.002	0.034	422	0.0156	0.0867
15	B1_LM	2865	15	0.123	1.845	422	0.0156	0.0654
16	B2_SH	2880	8.5	0.004	0.034	422	0.0156	0.0772
17	B2_LM	2888.5	13.5	10.2	137.7	422	0.0156	0.0959
18	B3_SH	2902	12.5	0.002	0.025	422	0.0156	0.0865
19	B3_LM	2914.5	4	0.047	0.188	422	0.0156	0.0837
20	B4_SH	2918.5	13.5	0.001	0.014	422	0.0156	0.1009
21	B4_LM	2932	6.5	3.2	20.80	422	0.0156	0.1155
22	B5_SH	2938.5	5	0.002	0.010	422	0.0156	0.1290
23	B5_LM	2943.5	20.5	72.1	1478.1	422	0.0156	0.0975
24	C_SH	2964	21.5	0.002	0.043	423	0.0156	0.0700
25	C_LM	2985.5	46	0.089	4.094	425	0.0157	0.07

Table 8.5.3 Model properties by layer, Chase hydraulic-fracture simulation, 1960. Pressures are from history-matched reservoir simulation (Bhattacharya et al., 2005)

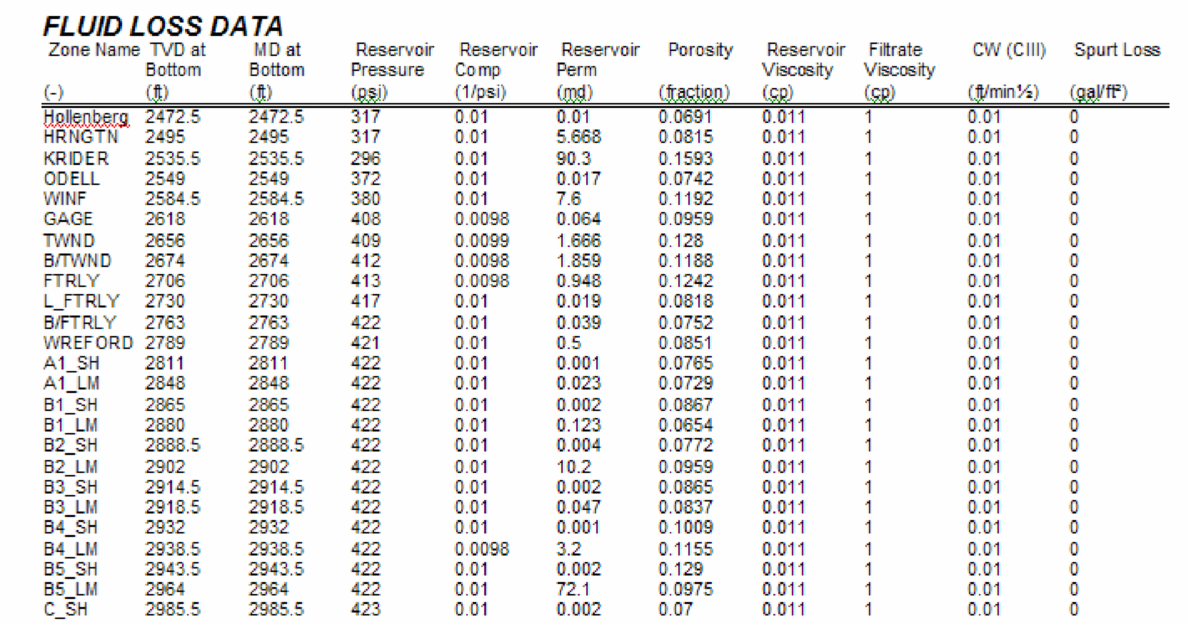

FLUID LOSS DATA

Zone Name (-)	TVD at Bottom (ft)	MD at Bottom (ft)	Reservoir Pressure (psi)	Reservoir Comp (1/psi)	Reservoir Perm (md)	Porosity (fraction)	Reservoir Viscosity (cp)	Filtrate Viscosity (cp)	CW (CIII) (ft/min½)	Spurt Loss (gal/ft^2)
Hollenberg	2472.5	2472.5	317	0.01	0.01	0.0691	0.011	1	0.01	0
HRNGTN	2495	2495	317	0.01	5.668	0.0815	0.011	1	0.01	0
KRIDER	2535.5	2535.5	296	0.01	90.3	0.1593	0.011	1	0.01	0
ODELL	2549	2549	372	0.01	0.017	0.0742	0.011	1	0.01	0
WINF	2584.5	2584.5	380	0.01	7.6	0.1192	0.011	1	0.01	0
GAGE	2618	2618	408	0.0098	0.064	0.0959	0.011	1	0.01	0
TWND	2656	2656	409	0.0099	1.666	0.128	0.011	1	0.01	0
B/TWND	2674	2674	412	0.0098	1.859	0.1188	0.011	1	0.01	0
FTRLY	2706	2706	413	0.0098	0.948	0.1242	0.011	1	0.01	0
L_FTRLY	2730	2730	417	0.01	0.019	0.0818	0.011	1	0.01	0
B/FTRLY	2763	2763	422	0.01	0.039	0.0752	0.011	1	0.01	0
WREFORD	2789	2789	421	0.01	0.5	0.0851	0.011	1	0.01	0
A1_SH	2811	2811	422	0.01	0.001	0.0765	0.011	1	0.01	0
A1_LM	2848	2848	422	0.01	0.023	0.0729	0.011	1	0.01	0
B1_SH	2865	2865	422	0.01	0.002	0.0867	0.011	1	0.01	0
B1_LM	2880	2880	422	0.01	0.123	0.0654	0.011	1	0.01	0
B2_SH	2888.5	2888.5	422	0.01	0.004	0.0772	0.011	1	0.01	0
B2_LM	2902	2902	422	0.01	10.2	0.0959	0.011	1	0.01	0
B3_SH	2914.5	2914.5	422	0.01	0.002	0.0865	0.011	1	0.01	0
B3_LM	2918.5	2918.5	422	0.01	0.047	0.0837	0.011	1	0.01	0
B4_SH	2932	2932	422	0.01	0.001	0.1009	0.011	1	0.01	0
B4_LM	2938.5	2938.5	422	0.0098	3.2	0.1155	0.011	1	0.01	0
B5_SH	2943.5	2943.5	422	0.01	0.002	0.129	0.011	1	0.01	0
B5_LM	2964	2964	422	0.01	72.1	0.0975	0.011	1	0.01	0
C_SH	2985.5	2985.5	423	0.01	0.002	0.07	0.011	1	0.01	0

Table 8.5.4 Model properties by layer, Chase hydraulic-fracture simulation, 1960.

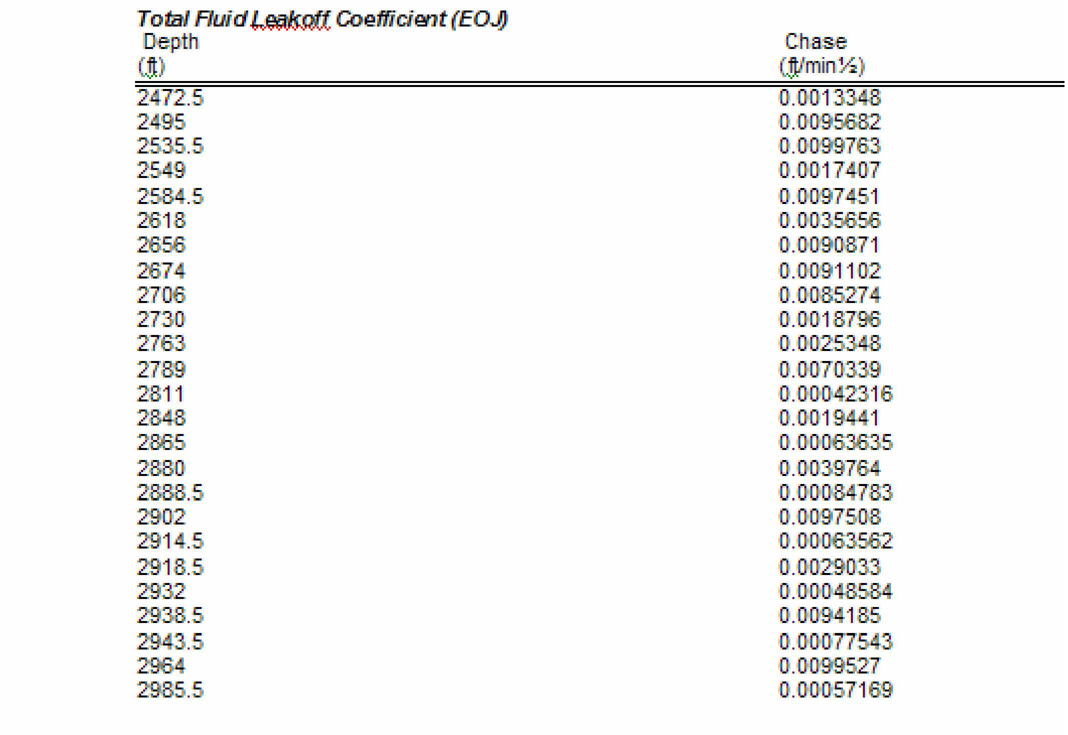

Total Fluid Leakoff Coefficient (EOJ)

Depth (ft)	Chase (ft/min½)
2472.5	0.0013348
2495	0.0095682
2535.5	0.0099763
2549	0.0017407
2584.5	0.0097451
2618	0.0035656
2656	0.0090871
2674	0.0091102
2706	0.0085274
2730	0.0018796
2763	0.0025348
2789	0.0070339
2811	0.00042316
2848	0.0019441
2865	0.00063635
2880	0.0039764
2888.5	0.00084783
2902	0.0097508
2914.5	0.00063562
2918.5	0.0029033
2932	0.00048584
2938.5	0.0094185
2943.5	0.00077543
2964	0.0099527
2985.5	0.00057169

Table 8.5.5 Model properties by layer, leak-off coefficients, Chase hydraulic-fracture simulation, 1960.

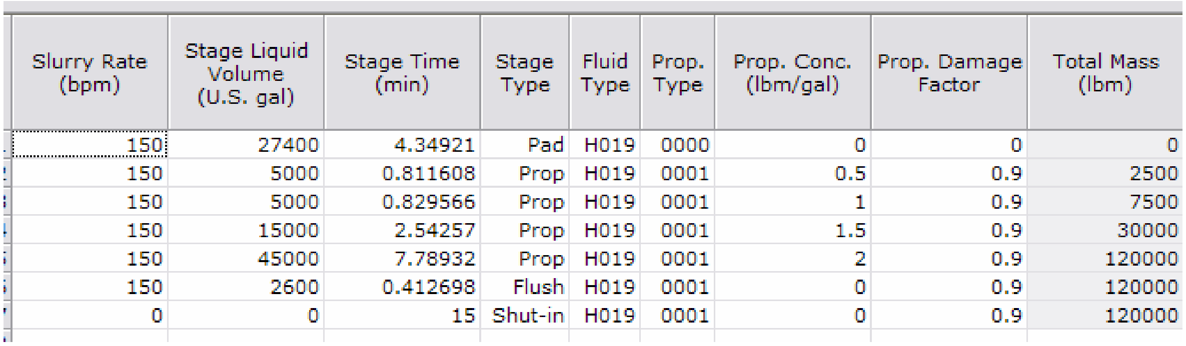

Slurry Rate (bpm)	Stage Liquid Volume (U.S. gal)	Stage Time (min)	Stage Type	Fluid Type	Prop. Type	Prop. Conc. (lbm/gal)	Prop. Damage Factor	Total Mass (lbm)
150	27400	4.34921	Pad	H019	0000	0	0	0
150	5000	0.811608	Prop	H019	0001	0.5	0.9	2500
150	5000	0.829566	Prop	H019	0001	1	0.9	7500
150	15000	2.54257	Prop	H019	0001	1.5	0.9	30000
150	45000	7.78932	Prop	H019	0001	2	0.9	120000
150	2600	0.412698	Flush	H019	0001	0	0.9	120000
0	0	15	Shut-in	H019	0001	0	0.9	120000

Table 8.5.6 Model treatment schedule assumptions, Chase hydraulic fracture simulation, 1960. We assumed fluid properties for Dowell WF120 (20lb linear gel). Actual viscosity may have been lower and would have resulted in less vertical growth.

Simulation Pass-1969 Pressures

Original Pressure **422**

Model Layer	Zone	Top Depth	Layer h	Layer K*	Layer Kh	Reservoir Pressure	Compress-ibility	Porosity
1a	HOLLENBRG	2450	22.5	0.01	0.225	230	0.0098	0.0691
1	HRNGTN	2472.5	22.5	5.668	128	230	0.0098	0.0815
2	KRIDER	2495	40.5	90.30	3657	204	0.0098	0.1593
3	ODELL	2535.5	13.5	0.017	0.230	420	0.0155	0.0742
4	WINF	2549	35.5	7.60	270	230.5	0.0098	0.1192
5	GAGE	2584.5	33.5	0.064	2.14	420	0.0155	0.0959
6	TWND	2618	38	1.666	63.3	283.5	0.0106	0.1280
7	B/TWND	2656	18	1.859	33.5	420	0.0155	0.1188
8	FTRLY	2674	32	0.948	30.3	314.5	0.0114	0.1242
9	L_FTRLY	2706	24	0.019	0.456	420	0.0155	0.0818
10	B/FTRLY	2730	33	0.039	1.287	420	0.0155	0.0752
11	WREFORD	2763	26	0.5	13.0	423.5	0.0157	0.0851
12	A1_SH	2789	22	0.001	0.022	420	0.0155	0.0765
13	A1_LM	2811	37	0.023	0.851	432.5	0.0161	0.0729
14	B1_SH	2848	17	0.002	0.034	420	0.0155	0.0867
15	B1_LM	2865	15	0.123	1.845	410	0.0150	0.0654
16	B2_SH	2880	8.5	0.004	0.034	420	0.0155	0.0772
17	B2_LM	2888.5	13.5	10.2	137.7	308	0.0112	0.0959
18	B3_SH	2902	12.5	0.002	0.025	420	0.0155	0.0865
19	B3_LM	2914.5	4	0.047	0.188	415	0.0153	0.0837
20	B4_SH	2918.5	13.5	0.001	0.014	420	0.0155	0.1009
21	B4_LM	2932	6.5	3.2	20.80	347.5	0.0125	0.1155
22	B5_SH	2938.5	5	0.002	0.010	420	0.0155	0.1290
23	B5_LM	2943.5	20.5	72.1	1478.1	322.5	0.0116	0.0975
24	C_SH	2964	21.5	0.002	0.043	423	0.0156	0.0700
25	C_LM	2985.5	46	0.089	4.094	425	0.0157	0.07

Table 8.5.7 Model properties by layer, Chase and Council Grove hydraulic-fracture simulations, 1969. Pressures are from history-matched reservoir simulation (Bhattacharya et al., 2005).

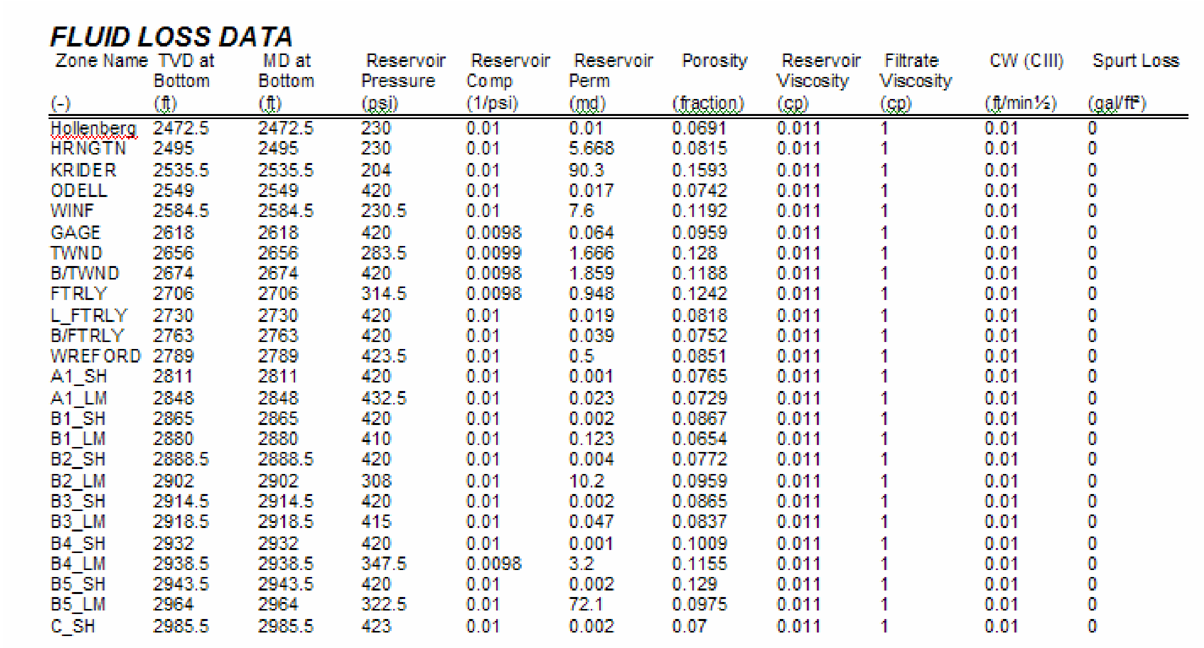

FLUID LOSS DATA

Zone Name (-)	TVD at Bottom (ft)	MD at Bottom (ft)	Reservoir Pressure (psi)	Reservoir Comp (1/psi)	Reservoir Perm (md)	Porosity (fraction)	Reservoir Viscosity (cp)	Filtrate Viscosity (cp)	CW (CIII) (ft/min½)	Spurt Loss (gal/ft^2)
Hollenberg	2472.5	2472.5	230	0.01	0.01	0.0691	0.011	1	0.01	0
HRNGTN	2495	2495	230	0.01	5.668	0.0815	0.011	1	0.01	0
KRIDER	2535.5	2535.5	204	0.01	90.3	0.1593	0.011	1	0.01	0
ODELL	2549	2549	420	0.01	0.017	0.0742	0.011	1	0.01	0
WINF	2584.5	2584.5	230.5	0.01	7.6	0.1192	0.011	1	0.01	0
GAGE	2618	2618	420	0.0098	0.064	0.0959	0.011	1	0.01	0
TWND	2656	2656	283.5	0.0099	1.666	0.128	0.011	1	0.01	0
B/TWND	2674	2674	420	0.0098	1.859	0.1188	0.011	1	0.01	0
FTRLY	2706	2706	314.5	0.0098	0.948	0.1242	0.011	1	0.01	0
L_FTRLY	2730	2730	420	0.01	0.019	0.0818	0.011	1	0.01	0
B/FTRLY	2763	2763	420	0.01	0.039	0.0752	0.011	1	0.01	0
WREFORD	2789	2789	423.5	0.01	0.5	0.0851	0.011	1	0.01	0
A1_SH	2811	2811	420	0.01	0.001	0.0765	0.011	1	0.01	0
A1_LM	2848	2848	432.5	0.01	0.023	0.0729	0.011	1	0.01	0
B1_SH	2865	2865	420	0.01	0.002	0.0867	0.011	1	0.01	0
B1_LM	2880	2880	410	0.01	0.123	0.0654	0.011	1	0.01	0
B2_SH	2888.5	2888.5	420	0.01	0.004	0.0772	0.011	1	0.01	0
B2_LM	2902	2902	308	0.01	10.2	0.0959	0.011	1	0.01	0
B3_SH	2914.5	2914.5	420	0.01	0.002	0.0865	0.011	1	0.01	0
B3_LM	2918.5	2918.5	415	0.01	0.047	0.0837	0.011	1	0.01	0
B4_SH	2932	2932	420	0.01	0.001	0.1009	0.011	1	0.01	0
B4_LM	2938.5	2938.5	347.5	0.0098	3.2	0.1155	0.011	1	0.01	0
B5_SH	2943.5	2943.5	420	0.01	0.002	0.129	0.011	1	0.01	0
B5_LM	2964	2964	322.5	0.01	72.1	0.0975	0.011	1	0.01	0
C_SH	2985.5	2985.5	423	0.01	0.002	0.07	0.011	1	0.01	0

Table 8.5.8 Model properties by layer, Chase hydraulic-fracture simulation, 1969.

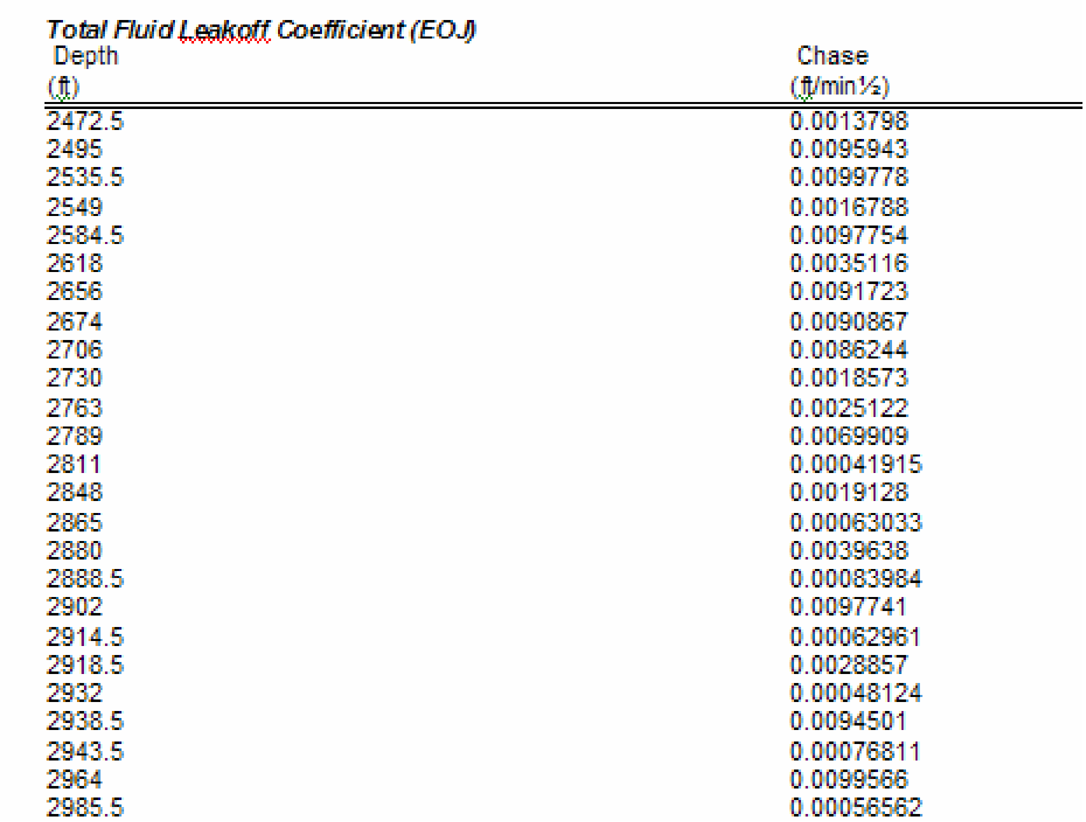

Total Fluid Leakoff Coefficient (EOJ)

Depth (ft)	Chase (ft/min½)
2472.5	0.0013798
2495	0.0095943
2535.5	0.0099778
2549	0.0016788
2584.5	0.0097754
2618	0.0035116
2656	0.0091723
2674	0.0090867
2706	0.0086244
2730	0.0018573
2763	0.0025122
2789	0.0069909
2811	0.00041915
2848	0.0019128
2865	0.00063033
2880	0.0039638
2888.5	0.00083984
2902	0.0097741
2914.5	0.00062961
2918.5	0.0028857
2932	0.00048124
2938.5	0.0094501
2943.5	0.00076811
2964	0.0099566
2985.5	0.00056562

Table 8.5.9 Model properties by layer, leak-off coefficients, Chase hydraulic-fracture simulation, 1969.

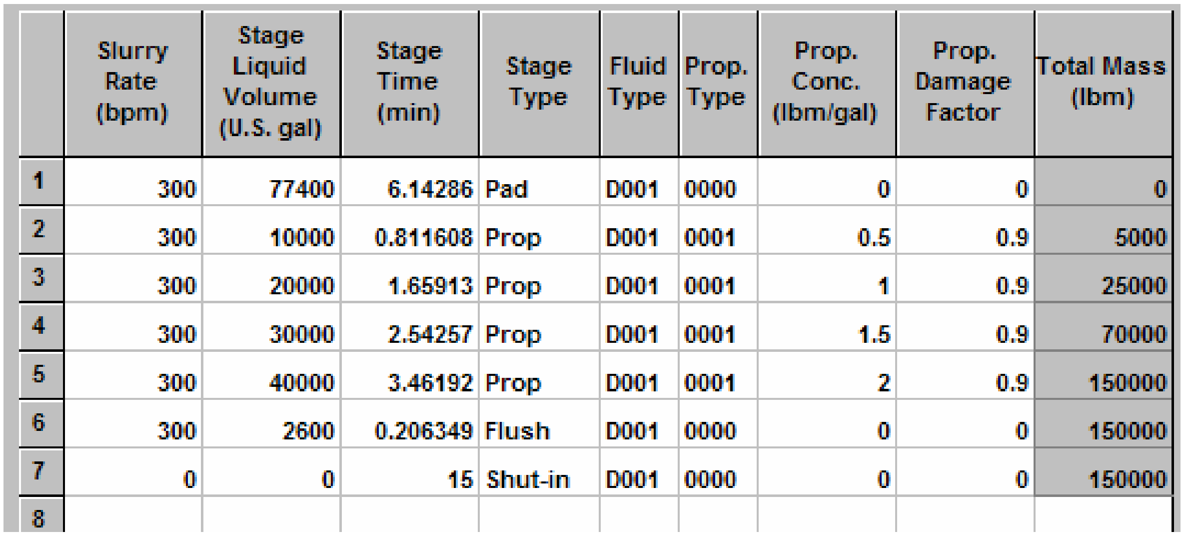

	Slurry Rate (bpm)	Stage Liquid Volume (U.S. gal)	Stage Time (min)	Stage Type	Fluid Type	Prop. Type	Prop. Conc. (lbm/gal)	Prop. Damage Factor	Total Mass (lbm)
1	300	77400	6.14286	Pad	D001	0000	0	0	0
2	300	10000	0.811608	Prop	D001	0001	0.5	0.9	5000
3	300	20000	1.65913	Prop	D001	0001	1	0.9	25000
4	300	30000	2.54257	Prop	D001	0001	1.5	0.9	70000
5	300	40000	3.46192	Prop	D001	0001	2	0.9	150000
6	300	2600	0.206349	Flush	D001	0000	0	0	150000
7	0	0	15	Shut-in	D001	0000	0	0	150000
8									

Table 8.5.10 Model treatment schedule assumptions. Chase hydraulic-fracture simulation, 1969.

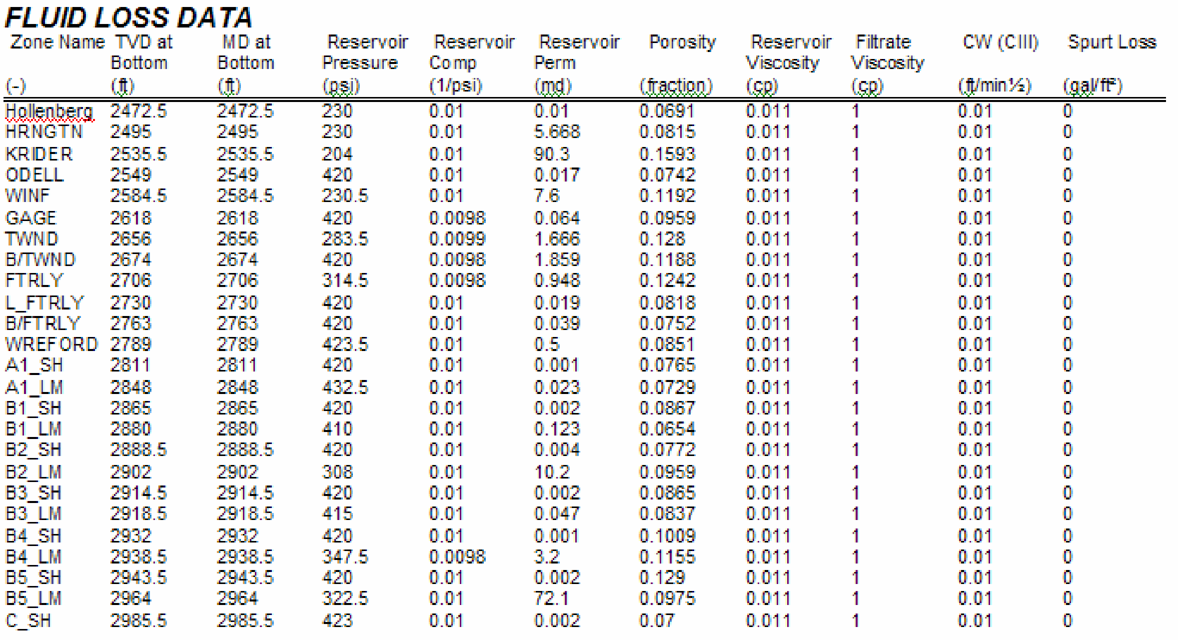

FLUID LOSS DATA

Zone Name (-)	TVD at Bottom (ft)	MD at Bottom (ft)	Reservoir Pressure (psi)	Reservoir Comp (1/psi)	Reservoir Perm (md)	Porosity (fraction)	Reservoir Viscosity (cp)	Filtrate Viscosity (cp)	CW (CIII) (ft/min½)	Spurt Loss (gal/ft²)
Hollenberg	2472.5	2472.5	230	0.01	0.01	0.0691	0.011	1	0.01	0
HRNGTN	2495	2495	230	0.01	5.668	0.0815	0.011	1	0.01	0
KRIDER	2535.5	2535.5	204	0.01	90.3	0.1593	0.011	1	0.01	0
ODELL	2549	2549	420	0.01	0.017	0.0742	0.011	1	0.01	0
WINF	2584.5	2584.5	230.5	0.01	7.6	0.1192	0.011	1	0.01	0
GAGE	2618	2618	420	0.0098	0.064	0.0959	0.011	1	0.01	0
TWND	2656	2656	283.5	0.0099	1.666	0.128	0.011	1	0.01	0
B/TWND	2674	2674	420	0.0098	1.859	0.1188	0.011	1	0.01	0
FTRLY	2706	2706	314.5	0.0098	0.948	0.1242	0.011	1	0.01	0
L_FTRLY	2730	2730	420	0.01	0.019	0.0818	0.011	1	0.01	0
B/FTRLY	2763	2763	420	0.01	0.039	0.0752	0.011	1	0.01	0
WREFORD	2789	2789	423.5	0.01	0.5	0.0851	0.011	1	0.01	0
A1_SH	2811	2811	420	0.01	0.001	0.0765	0.011	1	0.01	0
A1_LM	2848	2848	432.5	0.01	0.023	0.0729	0.011	1	0.01	0
B1_SH	2865	2865	420	0.01	0.002	0.0867	0.011	1	0.01	0
B1_LM	2880	2880	410	0.01	0.123	0.0654	0.011	1	0.01	0
B2_SH	2888.5	2888.5	420	0.01	0.004	0.0772	0.011	1	0.01	0
B2_LM	2902	2902	308	0.01	10.2	0.0959	0.011	1	0.01	0
B3_SH	2914.5	2914.5	420	0.01	0.002	0.0865	0.011	1	0.01	0
B3_LM	2918.5	2918.5	415	0.01	0.047	0.0837	0.011	1	0.01	0
B4_SH	2932	2932	420	0.01	0.001	0.1009	0.011	1	0.01	0
B4_LM	2938.5	2938.5	347.5	0.0098	3.2	0.1155	0.011	1	0.01	0
B5_SH	2943.5	2943.5	420	0.01	0.002	0.129	0.011	1	0.01	0
B5_LM	2964	2964	322.5	0.01	72.1	0.0975	0.011	1	0.01	0
C_SH	2985.5	2985.5	423	0.01	0.002	0.07	0.011	1	0.01	0

Table 8.5.11 Model properties by layer, Council Grove hydraulic-fracture simulation, 1969.

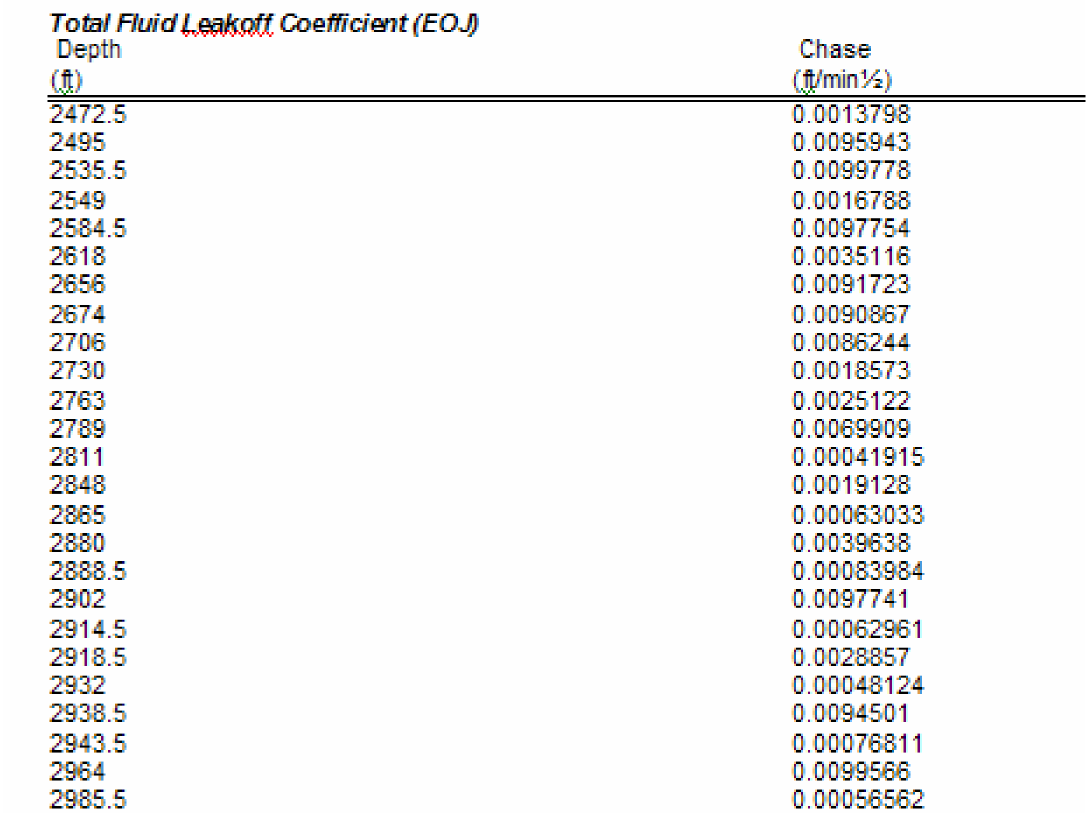

Total Fluid Leakoff Coefficient (EOJ)

Depth (ft)	Chase (ft/min½)
2472.5	0.0013798
2495	0.0095943
2535.5	0.0099778
2549	0.0016788
2584.5	0.0097754
2618	0.0035116
2656	0.0091723
2674	0.0090867
2706	0.0086244
2730	0.0018573
2763	0.0025122
2789	0.0069909
2811	0.00041915
2848	0.0019128
2865	0.00063033
2880	0.0039638
2888.5	0.00083984
2902	0.0097741
2914.5	0.00062961
2918.5	0.0028857
2932	0.00048124
2938.5	0.0094501
2943.5	0.00076811
2964	0.0099566
2985.5	0.00056562

Table 8.5.12 Model properties by layer, leak-off coefficients, Council Grove hydraulic-fracture simulation, 1969.

INPUT SURFACE TREATMENT SCHEDULE

Schedule Type	Surface	
Wellbore Fluid Type	KCL2	
Fraction of Well Filled	1	
Recirculation Volume	0	(U.S. gal)

Stage No. (-)	Slurry Rate (bpm)	Stage Liquid Volume (U.S. gal)	Stage Time (min)	Stage Type (-)	Fluid Type (-)	Prop Type (-)	Prop Conc. (lbm/gal)
1	150	61000	9.6825	Pad	D029	0000	0
2	150	5000	0.81161	Prop	D029	0001	0.5
3	150	9500	1.5762	Prop	D029	0001	1
4	150	16000	2.7121	Prop	D029	0001	1.5
5	150	32000	5.5391	Prop	D029	0001	2
6	150	2500	0.39683	Flush	D029	0001	0
7	0	0	15	Shut-in	D029	0001	0

Fluid Type: KCL2 - 2% KCl
Fluid Type: D029 - WF230, 2% KCl without breaker
Proppant Type: 0000 - No Prop, Slug, ...
Proppant Type: 0001 - 20/40 Jordan Sand

Table 8.5.13 Model treatment schedule assumptions. Council Grove hydraulic-fracture simulation, 1969.

Simulation Pass-1990 Pressures
Original Pressure 422

Model Layer	Zone	Top Depth	Layer h	Layer K*	Layer Kh	Reservoir Pressure	Compress-ibility	Porosity
1a	HOLLENBRG	2450	22.5	0.01	0.225	140	0.0107	0.0691
1	HRNGTN	2472.5	22.5	5.668	128	108	0.0118	0.0815
2	KRIDER	2495	40.5	90.30	3657	400	0.0146	0.1593
3	ODELL	2535.5	13.5	0.017	0.230	141	0.0107	0.0742
4	WINF	2549	35.5	7.60	270	400	0.0146	0.1192
5	GAGE	2584.5	33.5	0.064	2.14	207	0.0098	0.0959
6	TWND	2618	38	1.666	63.3	400	0.0146	0.1280
7	B/TWND	2656	18	1.859	33.5	249	0.0100	0.1188
8	FTRLY	2674	32	0.948	30.3	400	0.0146	0.1242
9	L_FTRLY	2706	24	0.019	0.456	400	0.0146	0.0818
10	B/FTRLY	2730	33	0.039	1.287	382	0.0138	0.0752
11	WREFORD	2763	26	0.5	13.0	400	0.0146	0.0851
12	A1_SH	2789	22	0.001	0.022	400	0.0146	0.0765
13	A1_LM	2811	37	0.023	0.851	400	0.0146	0.0729
14	B1_SH	2848	17	0.002	0.034	355	0.0128	0.0867
15	B1_LM	2865	15	0.123	1.845	400	0.0146	0.0654
16	B2_SH	2880	8.5	0.004	0.034	151	0.0105	0.0772
17	B2_LM	2888.5	13.5	10.2	137.7	400	0.0146	0.0959
18	B3_SH	2902	12.5	0.002	0.025	365	0.0131	0.0865
19	B3_LM	2914.5	4	0.047	0.188	400	0.0146	0.0837
20	B4_SH	2918.5	13.5	0.001	0.014	230	0.0098	0.1009
21	B4_LM	2932	6.5	3.2	20.80	400	0.0146	0.1155
22	B5_SH	2938.5	5	0.002	0.010	180	0.0100	0.1290
23	B5_LM	2943.5	20.5	72.1	1478.1	322.5	0.0116	0.0975
24	C_SH	2964	21.5	0.002	0.043	423	0.0156	0.0700
25	C_LM	2985.5	46	0.089	4.094	425	0.0157	0.07

Table 8.5.14 Model properties by layer, Chase (infill) hydraulic-fracture simulations, 1987. Most pressures are from 24-hour SIP on DST for Flower A1 well in 1990.

FLUID LOSS DATA

Zone Name (-)	TVD at Bottom (ft)	MD at Bottom (ft)	Reservoir Pressure (psi)	Reservoir Comp (1/psi)	Reservoir Perm (md)	Porosity (fraction)	Reservoir Viscosity (cp)	Filtrate Viscosity (cp)	CW (CIII) (ft/min^1/2)	Spu (gal/ ft^2)
Hollenberg	2472.5	2472.5	140	0.01	0.01	0.0691	1	1	0.003	0
HRNGTN	2495	2495	140	0.01	5.668	0.0815	1	1	0.003	0
KRIDER	2535.5	2535.5	108	0.01	90.3	0.1593	1	1	0.003	0
ODELL	2549	2549	400	0.01	0.017	0.0742	1	1	0.003	0
WINF	2584.5	2584.5	141	0.01	7.6	0.1192	1	1	0.003	0
GAGE	2618	2618	400	0.0098	0.064	0.0959	1	1	0.003	0
TWND	2656	2656	207	0.0099	1.666	0.128	1	1	0.003	0
B/TWND	2674	2674	400	0.0098	1.859	0.1188	1	1	0.003	0
FTRLY	2706	2706	249	0.0098	0.948	0.1242	1	1	0.003	0
L_FTRLY	2730	2730	400	0.01	0.019	0.0818	1	1	0.003	0
B/FTRLY	2763	2763	400	0.01	0.039	0.0752	1	1	0.003	0
WREFORD	2789	2789	382	0.01	0.5	0.0851	1	1	0.003	0
A1_SH	2811	2811	400	0.01	0.001	0.0765	1	1	0.003	0
A1_LM	2848	2848	400	0.01	0.023	0.0729	1	1	0.003	0
B1_SH	2865	2865	400	0.01	0.002	0.0867	1	1	0.003	0
B1_LM	2880	2880	355	0.01	0.123	0.0654	1	1	0.003	0
B2_SH	2888.5	2888.5	400	0.01	0.004	0.0772	1	1	0.003	0
B2_LM	2902	2902	151	0.01	10.2	0.0959	1	1	0.003	0
B3_SH	2914.5	2914.5	400	0.01	0.002	0.0865	1	1	0.003	0
B3_LM	2918.5	2918.5	365	0.01	0.047	0.0837	1	1	0.003	0
B4_SH	2932	2932	400	0.01	0.001	0.1009	1	1	0.003	0
B4_LM	2938.5	2938.5	230	0.0098	3.2	0.1155	1	1	0.003	0
B5_SH	2943.5	2943.5	400	0.01	0.002	0.129	1	1	0.003	0
B5_LM	2964	2964	180	0.01	72.1	0.0975	1	1	0.003	0
C_SH	2985.5	2985.5	321	0.01	0.002	0.07	1	1	0.003	0

Table 8.5.15 Model properties by layer, Chase (infill) hydraulic-fracture simulations, 1987.

Total Fluid Leakoff Coefficient (EOJ)

Depth (ft)	Herrington (ft/min^1/2)	U.Krider (ft/min^1/2)	Winfield (ft/min^1/2)	Winfield C (ft/min^1/2)	Towanda (ft/min^1/2)	U. Ft. Riley (ft/min^1/2)	L. Ft. Riley (ft/min^1/2)	Florence Flint (ft/min^1/2)	Wreford (ft/min^1/
2472.5	0.0023905	0.0024807	0.0024861	0.0024645	0.0025103	0.0022335	0.002528	0.0025425	0.002497
2495	0.0029735	0.0029779	0.0029782	0.0029771	0.0029793	0.0029655	0.0029801	0.0029808	0.002978
2535.5	0.0029953	0.0029961	0.0029961	0.0029959	0.0029963	0.0029939	0.0029965	0.0029966	0.002996
2549	0.0024753	0.0025637	0.0025689	0.0025482	0.0025918	0.0023104	0.0026084	0.0026219	0.002579
2584.5	0.0029811	0.0029842	0.0029844	0.0029836	0.0029852	0.0029753	0.0029858	0.0029863	0.002984
2618	0.002746	0.002791	0.0027936	0.0027832	0.0028051	0.002659	0.0028134	0.0028201	0.002798
2656	0.0029597	0.0029665	0.0029669	0.0029653	0.0029686	0.0029469	0.0029699	0.0029709	0.002967
2674	0.002956	0.0029641	0.0029645	0.0029627	0.0029666	0.0029401	0.002968	0.0029692	0.002965
2706	0.0029444	0.002954	0.0029545	0.0029523	0.002957	0.0029264	0.0029587	0.0029602	0.002955
2730	0.0025224	0.0026037	0.0026084	0.0025895	0.0026294	0.0023698	0.0026446	0.0026569	0.002618
2763	0.0026435	0.0027056	0.0027092	0.0026948	0.0027251	0.002525	0.0027366	0.0027459	0.002716
2789	0.0029027	0.0029202	0.0029212	0.0029172	0.0029257	0.0028684	0.0029289	0.0029315	0.002923
2811	0.0014584	0.0016408	0.0016523	0.0016069	0.0017044	0.0011815	0.0017433	0.0017758	0.001675
2848	0.0025386	0.0026174	0.002622	0.0026036	0.0026423	0.0023904	0.002657	0.0026689	0.002631
2865	0.0018186	0.0019836	0.0019937	0.0019537	0.0020389	0.0015461	0.0020722	0.0020996	0.002014
2880	0.002784	0.0028218	0.002824	0.0028153	0.0028337	0.0027116	0.0028406	0.0028463	0.002828
2888.5	0.0020483	0.0021921	0.0022007	0.0021664	0.0022393	0.0017991	0.0022674	0.0022905	0.002218
2902	0.0029817	0.0029847	0.0029849	0.0029842	0.0029857	0.0029761	0.0029863	0.0029867	0.002985
2914.5	0.0018176	0.0019827	0.0019928	0.0019528	0.002038	0.0015451	0.0020713	0.0020988	0.002013
2918.5	0.0026948	0.0027476	0.0027507	0.0027384	0.0027643	0.0025943	0.002774	0.002782	0.002756
2932	0.0015827	0.0017616	0.0017727	0.0017286	0.001823	0.001303	0.0018604	0.0018915	0.001795
2938.5	0.0029688	0.0029741	0.0029744	0.0029732	0.0029758	0.0029587	0.0029768	0.0029776	0.002975
2943.5	0.0019798	0.0021306	0.0021397	0.0021036	0.0021804	0.001722	0.0022102	0.0022347	0.002158
2964	0.0029931	0.0029942	0.0029943	0.002994	0.0029946	0.0029909	0.0029948	0.002995	0.002994
2985.5	0.0017633	0.0019263	0.0019363	0.0018965	0.0019816	0.001501	0.002015	0.0020428	0.001956

Table 8.5.16 Model properties by layer, leak-off coefficients, Chase (infill) hydraulic-fracture simulations, 1987. Lower leak-off coefficients are from increased wall building (0.003).

INPUT SURFACE TREATMENT SCHEDULE

Schedule Type	Surface	
Wellbore Fluid Type	KCL2	
Fraction of Well Filled	1	
Recirculation Volume	0	(U.S. gal)

Stage No. (-)	Slurry Rate (bpm)	Stage Liquid Volume (U.S. gal)	Stage Time (min)	Stage Type (-)	Fluid Type (-)	Prop Type (-)	Prop Conc. (lbm/gal)	Prop Dama Factor (-)
1	60	30000	11.905	Pad	KCL2	0000	0	0
2	60	10000	4.1478	Prop	H535	0003	1	0.9
3	60	10000	4.3274	Prop	H535	0003	2	0.9
4	60	10000	4.507	Prop	H535	0003	3	0.9
5	60	10000	4.6866	Prop	H535	0003	4	0.9
6	60	10000	4.8661	Prop	H535	0003	5	0.9
7	60	10000	5.0457	Prop	H535	0003	6	0.9
8	60	5000	2.7024	Prop	H535	0003	8	0.9
9	60	5000	2.882	Prop	H535	0003	10	0.9
10	60	2300	0.9127	Flush	D003	0000	0	0
11	0	0	15	Shut-in	D003	0000	0	0

Fluid Type: KCL2 - 2% KCl
Fluid Type: H535 - Hybor H 30 lb/Mgal WG-11 12 pH
Fluid Type: D003 - WF130, 2% KCl w/ No Breaker
Proppant Type: 0000 - No Prop, Slug, ...
Proppant Type: 0003 - 12/20 Jordan Sand

Table 8.5.17 Model treatment schedule assumptions. Chase (infill) hydraulic-fracture simulations, 1987.

Figures:

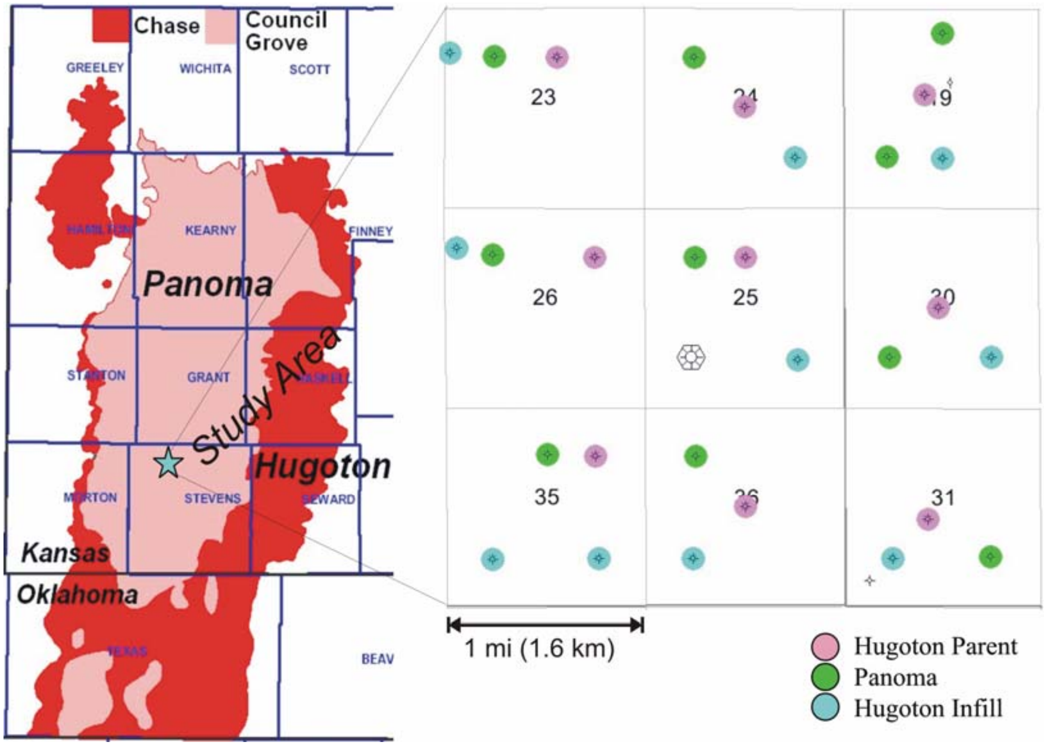

Figure 8.5.1 Study area is near the center of the Hugoton and Panoma fields in T. 31 S., R. 38 W., Stevens County, Kansas. The Flower A1 well is a well with substantial core and pressure-test information that is central to the study.

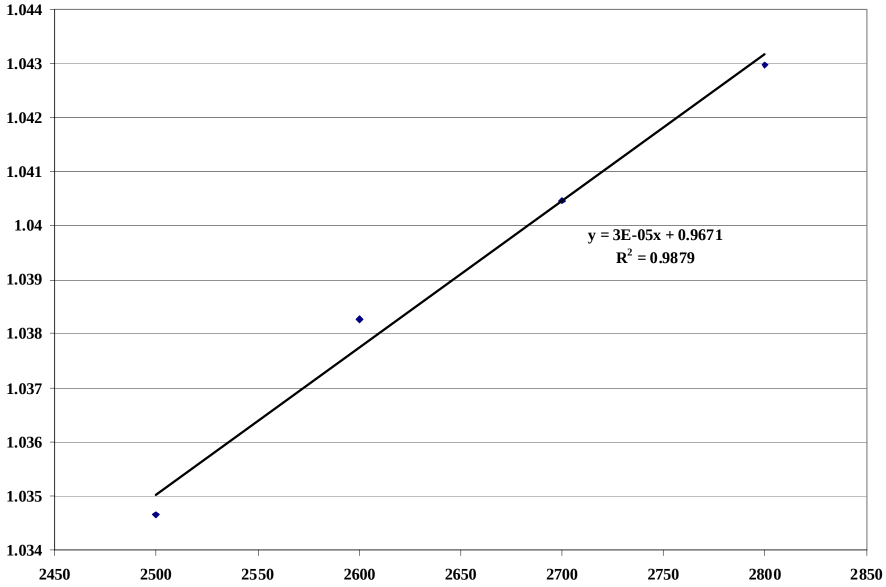

Figure 8.5.2 Overburden gradient versus depth.

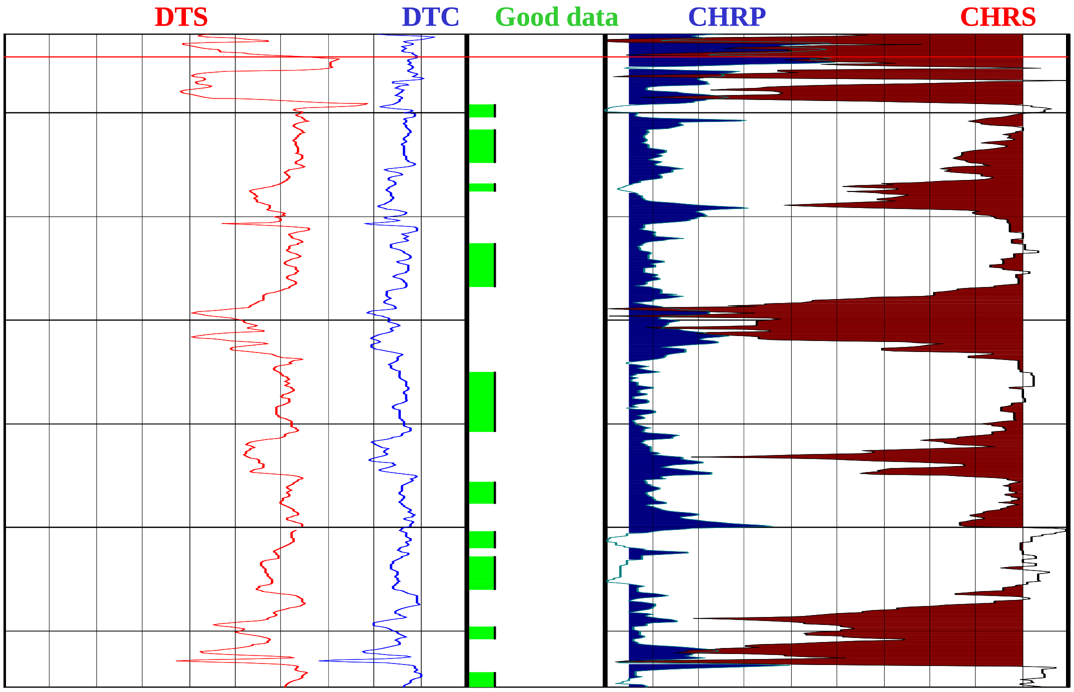

Figure 8.5.3 Dipole sonic quality check for Chase Group, Flower A1 well.

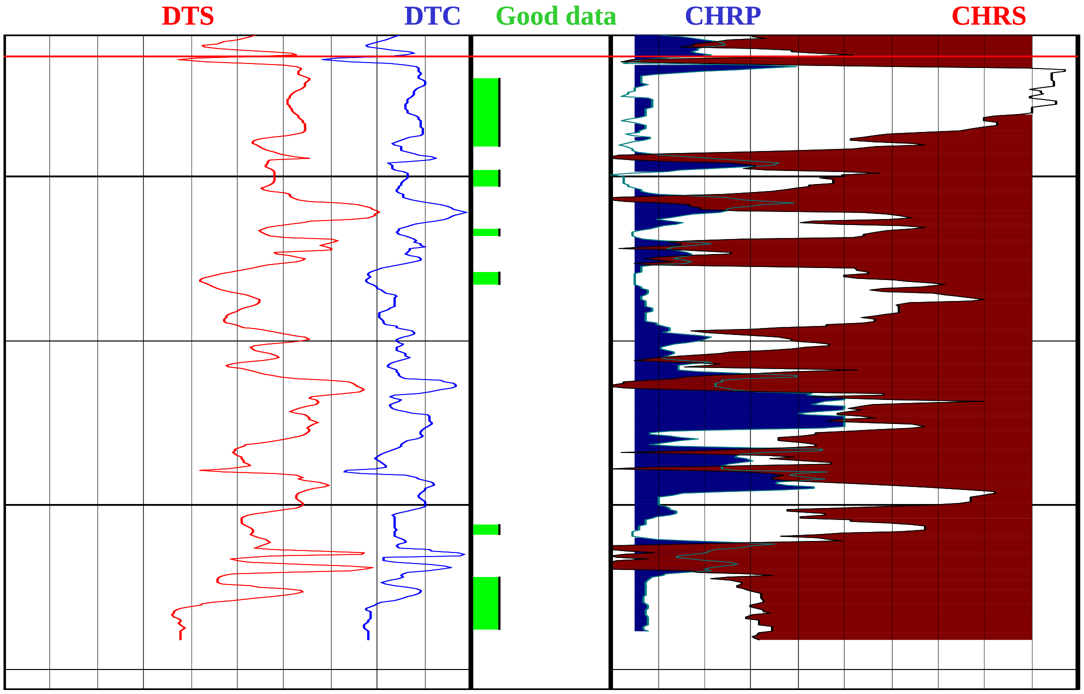

Figure 8.5.4 Dipole sonic quality check for Council Grove Group, Flower A1 well.

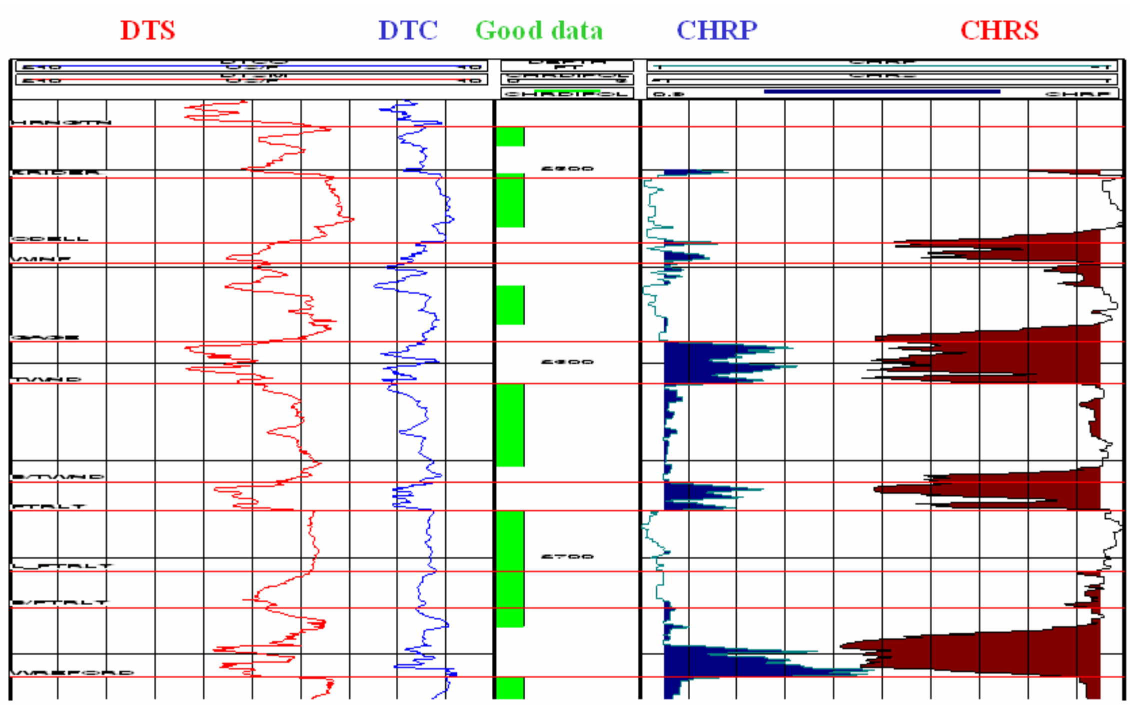

Figure 8.5.5 Dipole sonic quality check for Chase Group, Youngren #1 well.

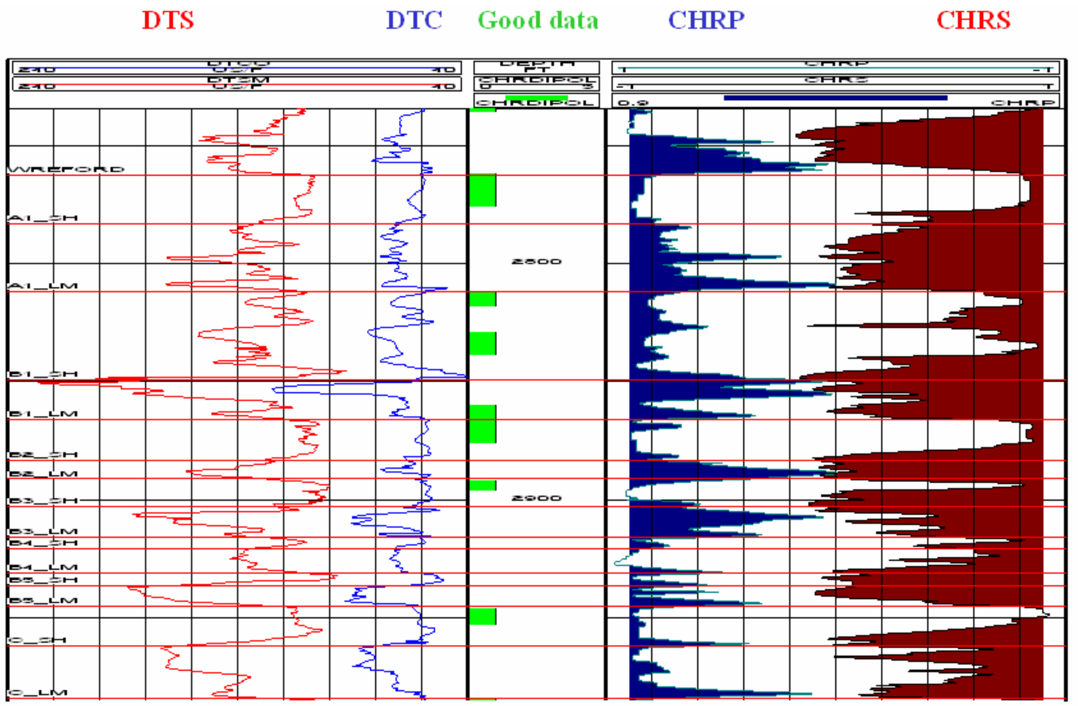

Figure 8.5.6 Dipole sonic quality check for Council Grove Group, Youngren #1 well.

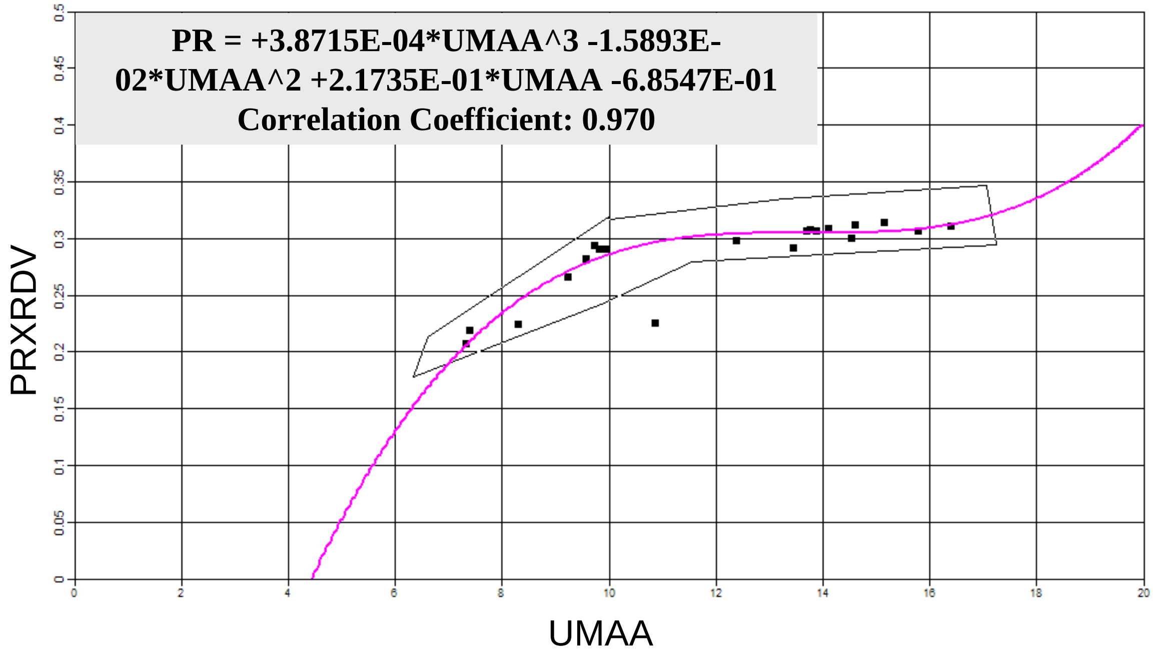

Figure 8.5.7 U matrix apparent from core-derived grain densities.

Figure 8.5.8 Formation- and member-level stratigraphy correlated to wireline well log in the Flower A1 well, Stevens County, Kansas. Commonly used formation/member letter-number combinations are shown for the Council Grove. Twelve of the13 marine-continental (carbonate-siliciclastic) sedimentary cycles that are gas productive are shown (Grenola Limestone, C_LM is not logged). Color-coded lithofacies are derived from core. Three were deposited in a continental setting, L0- sandstone, L1- coarse siltstone, and L2- shaly siltstone, and eight in a marine environment, L3- siltstone, L4- carbonate mudstone, L5- wackestone, L6- very fine crystalline dolomite, L7- packstone, L8- grainstone and phylloid algal bafflestone, L9- fine-medium crystalline moldic dolomite, and L10- sandstone. Wireline log abbreviations are caliper (CALI), gamma ray (GR), corrected porosity (PHI_GM3), photoelectric effect (PEF), density porosity (DPHI), neutron porosity (NPHI), core permeability (K_MAX), and core porosity (CORE_POR). Logged interval is 520 ft (160 m) (after Dubois et al., *in press*).

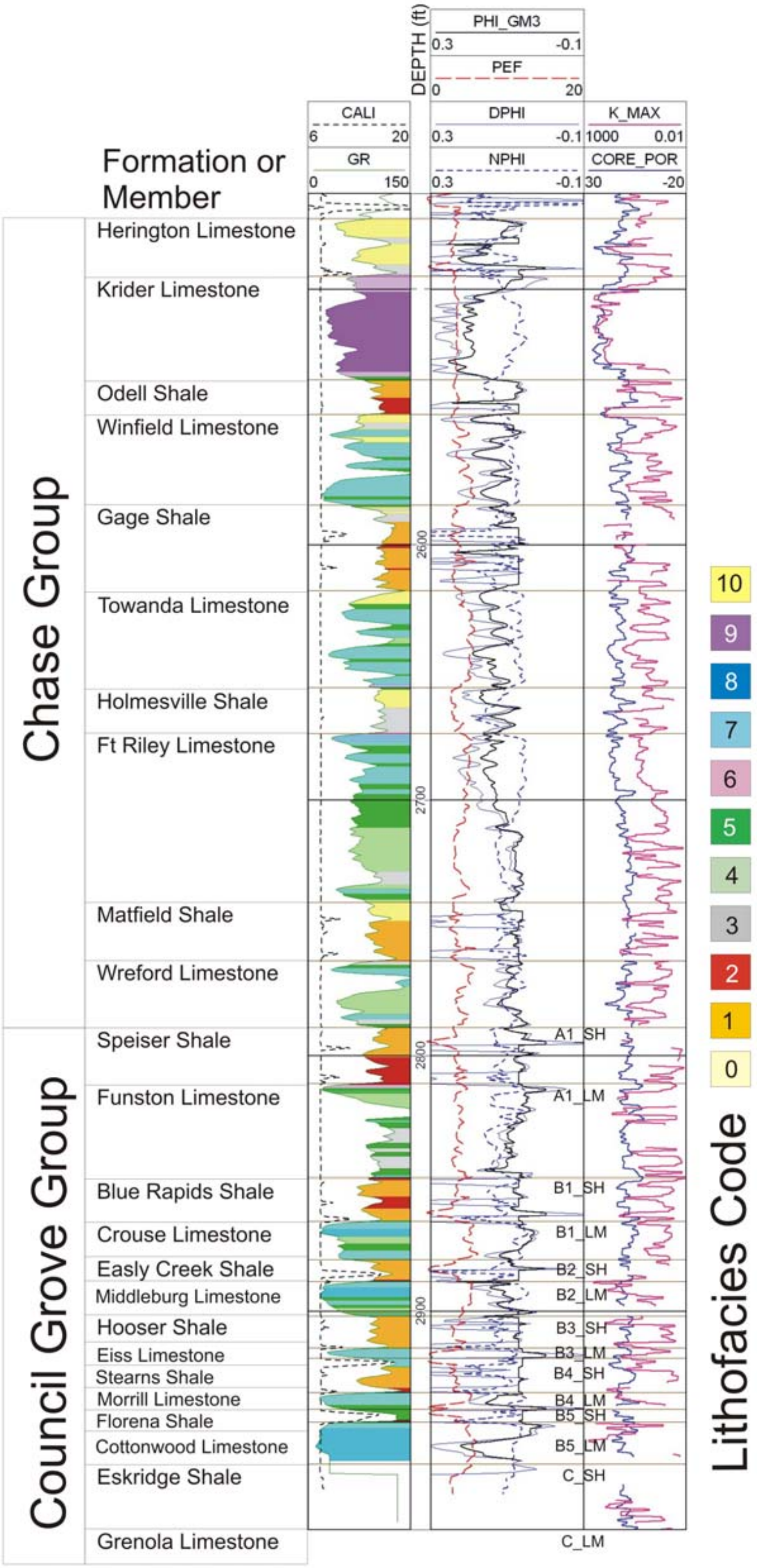

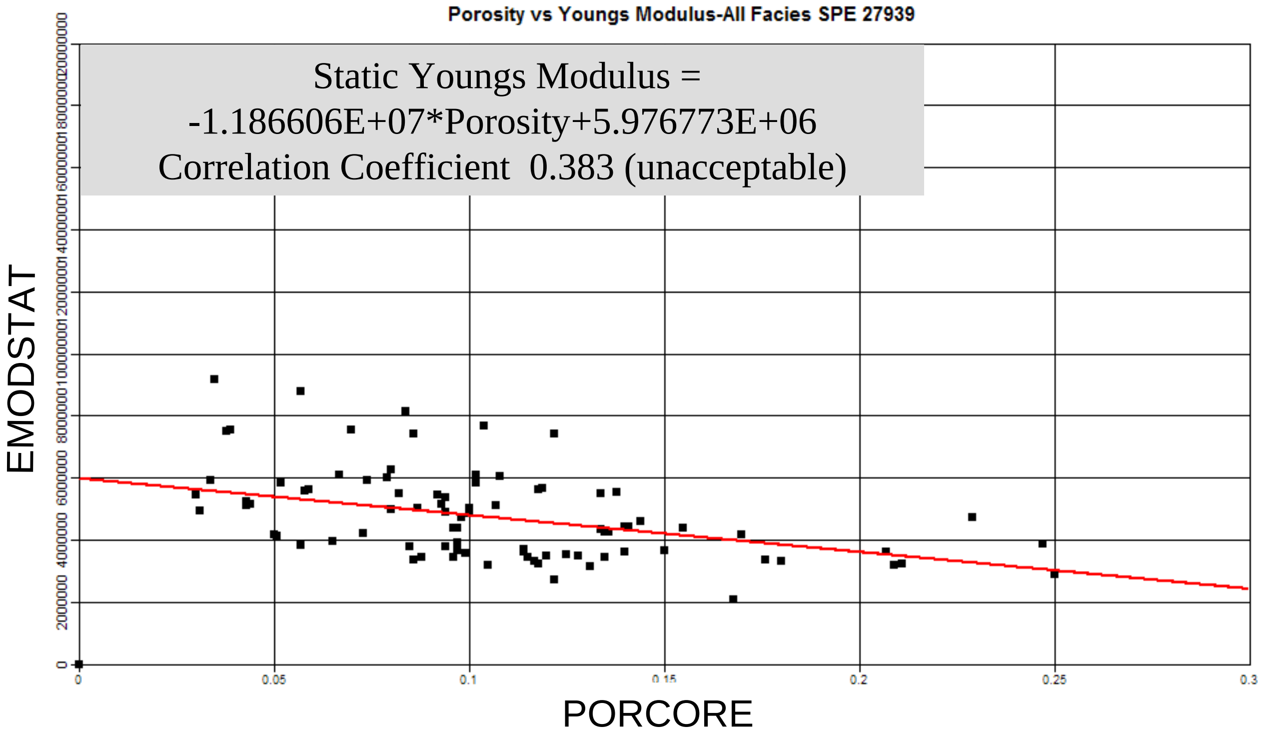

Figure 8.5.9 Porosity vs. Young's modulus (Yale and Jamieson, 1994), has a high correlation coefficient.

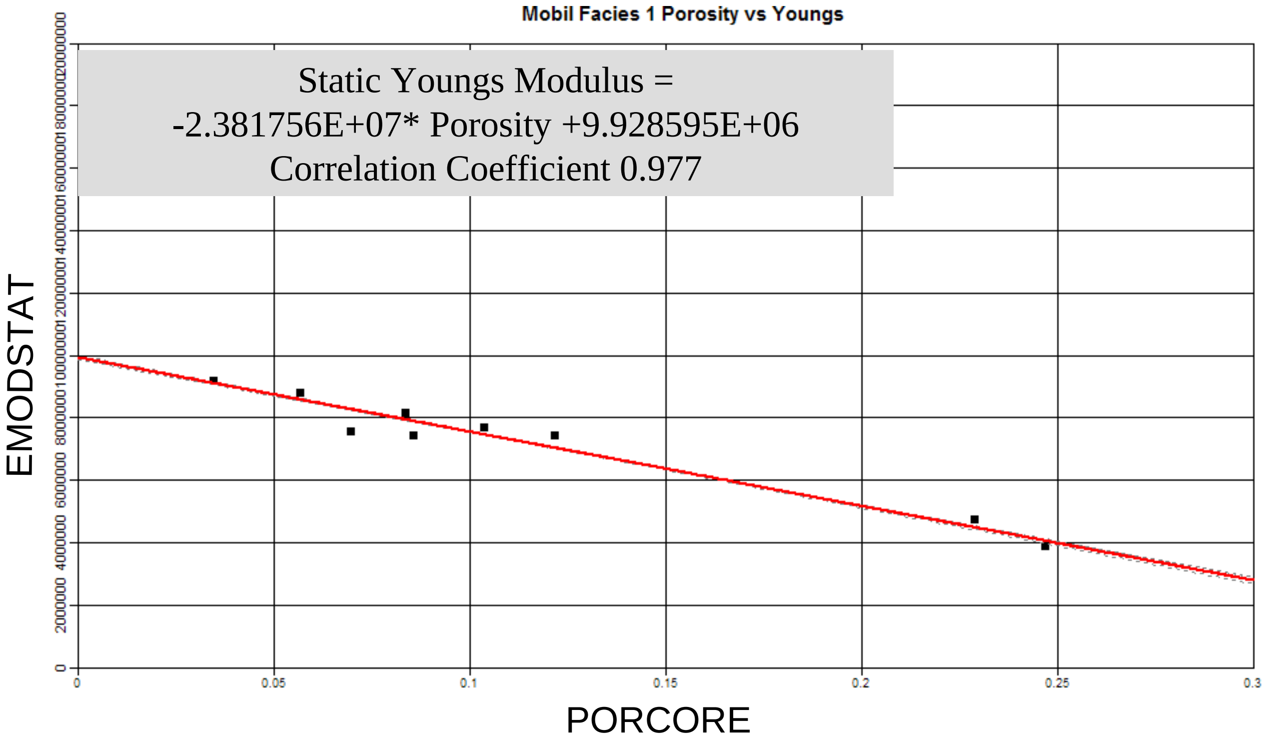

Figure 8.5.10 Porosity vs.Young's modulus (Yale and Jamieson, 1994) rock-mechanical facies 1.

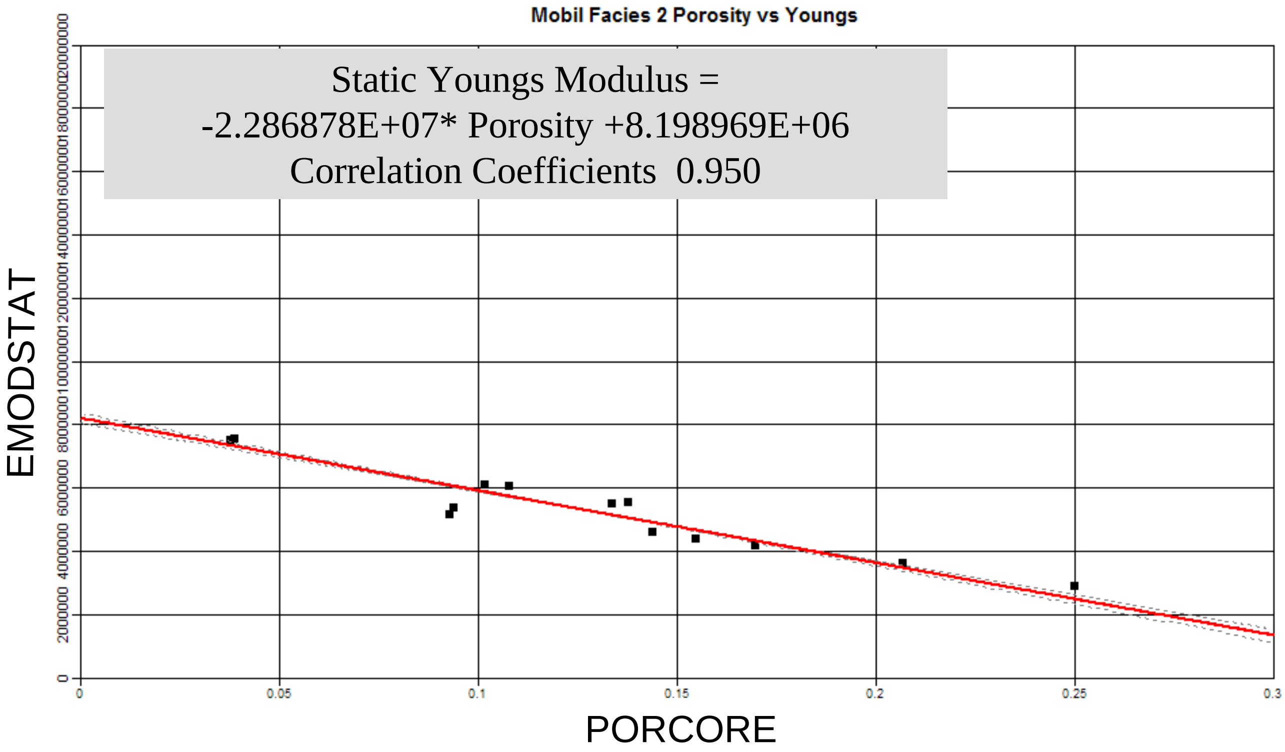

Figure 8.5.11 Porosity vs.Young's modulus (Yale and Jamieson, 1994) rock-mechanical facies 2.

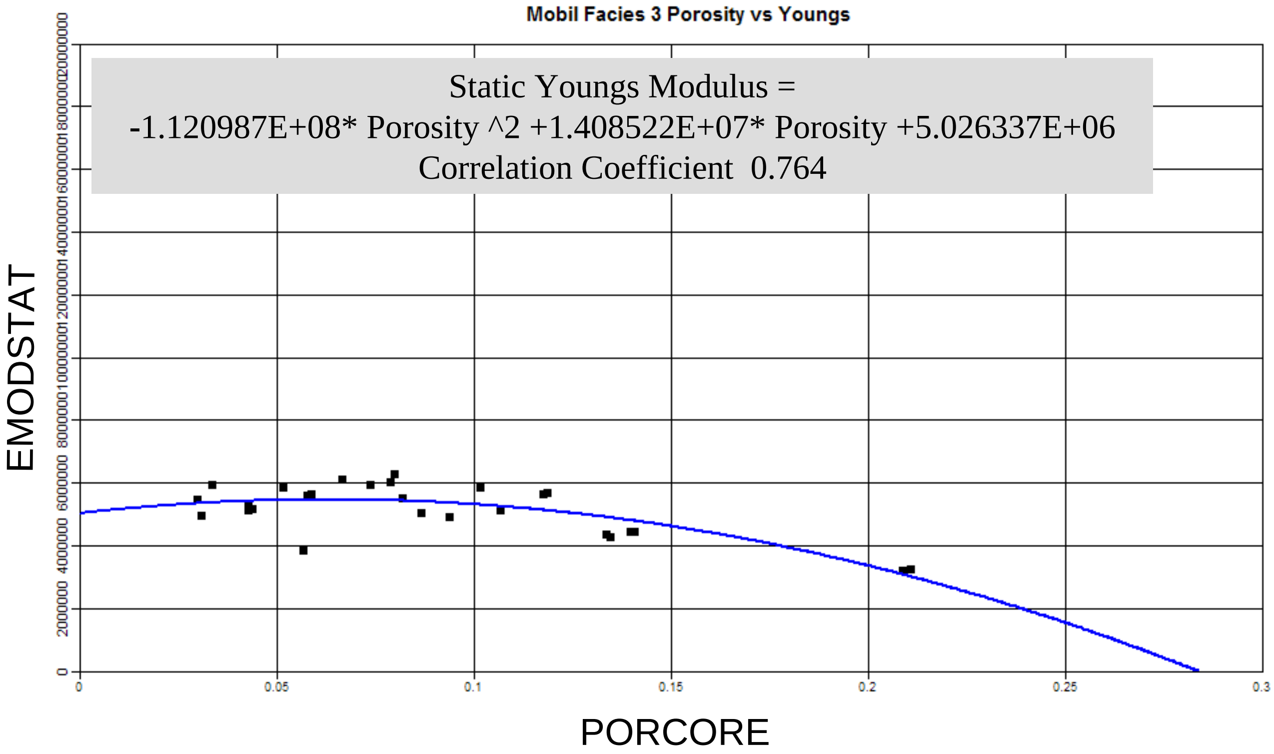

Figure 8.5.12 Porosity vs.Young's modulus (Yale and Jamieson, 1994) rock mechanical facies 3.

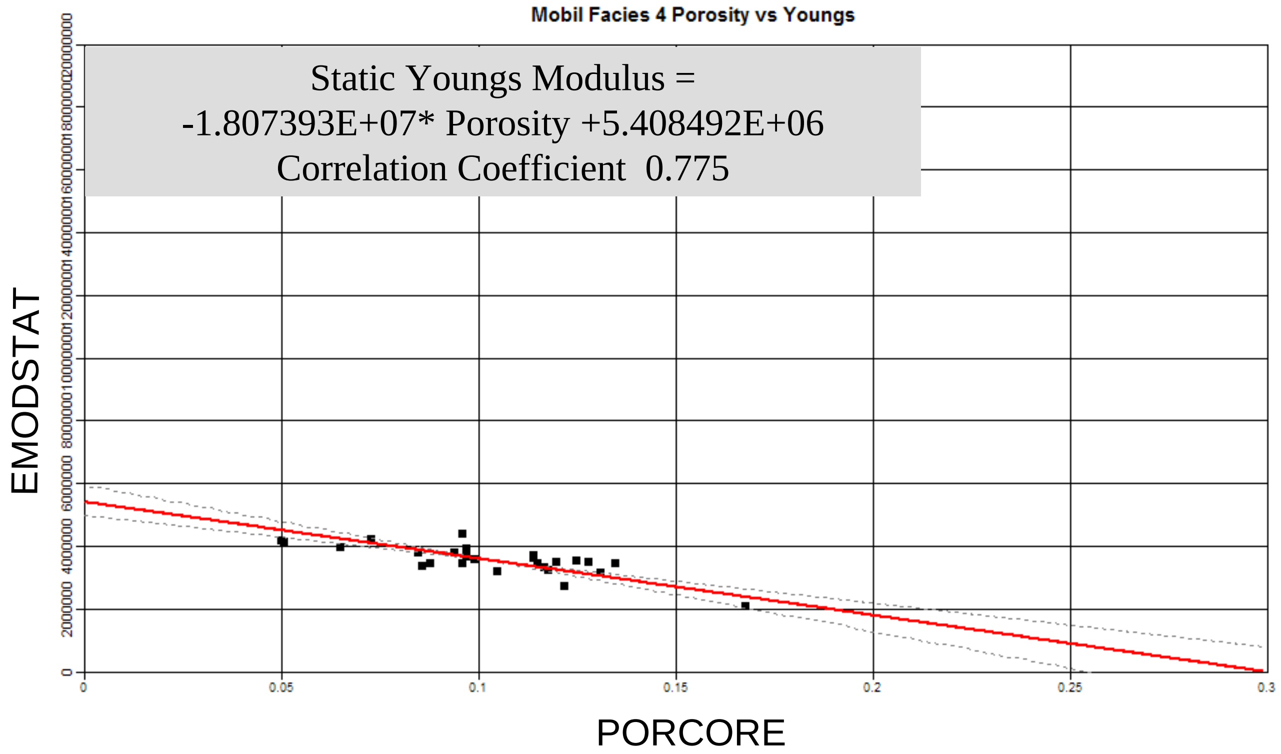

Figure 8.5.13 Porosity vs.Young's modulus (Yale and Jamieson, 1994) rock-mechanical facies 4.

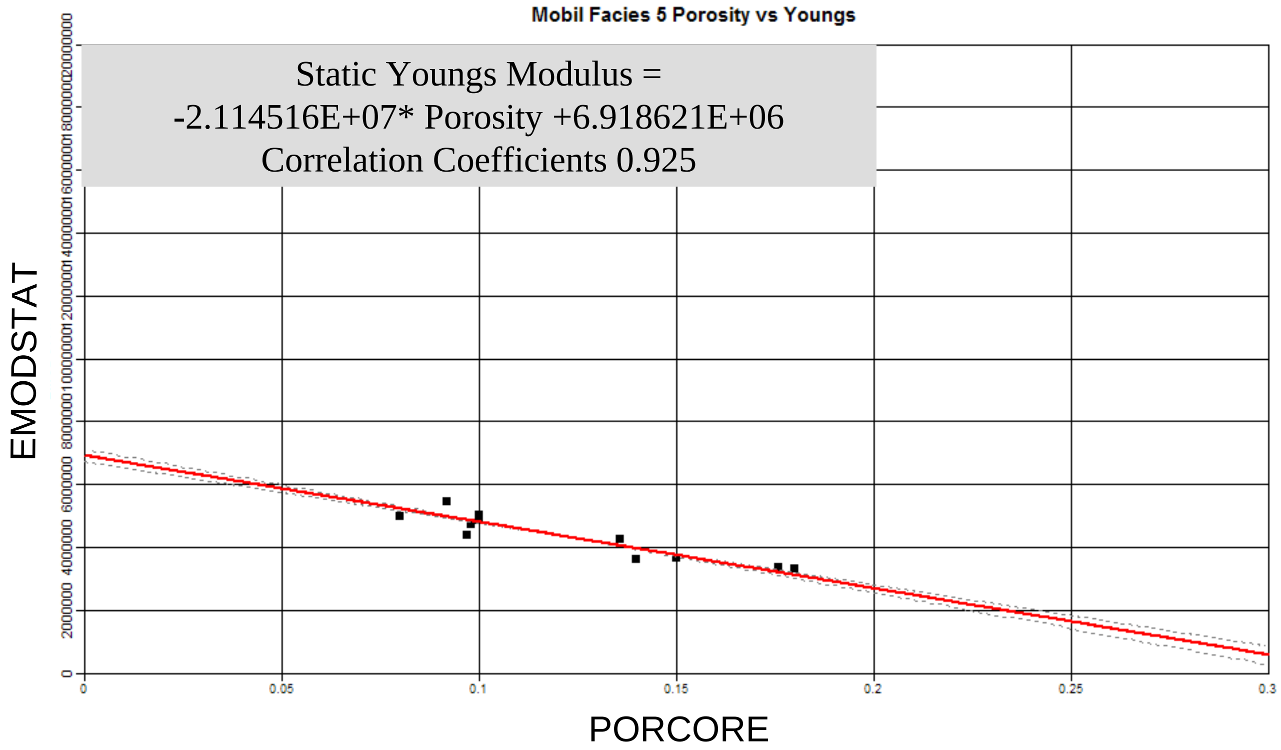

Figure 8.5.14 Porosity vs.Young's modulus (Yale and Jamieson, 1994) rock-mechanical facies 5.

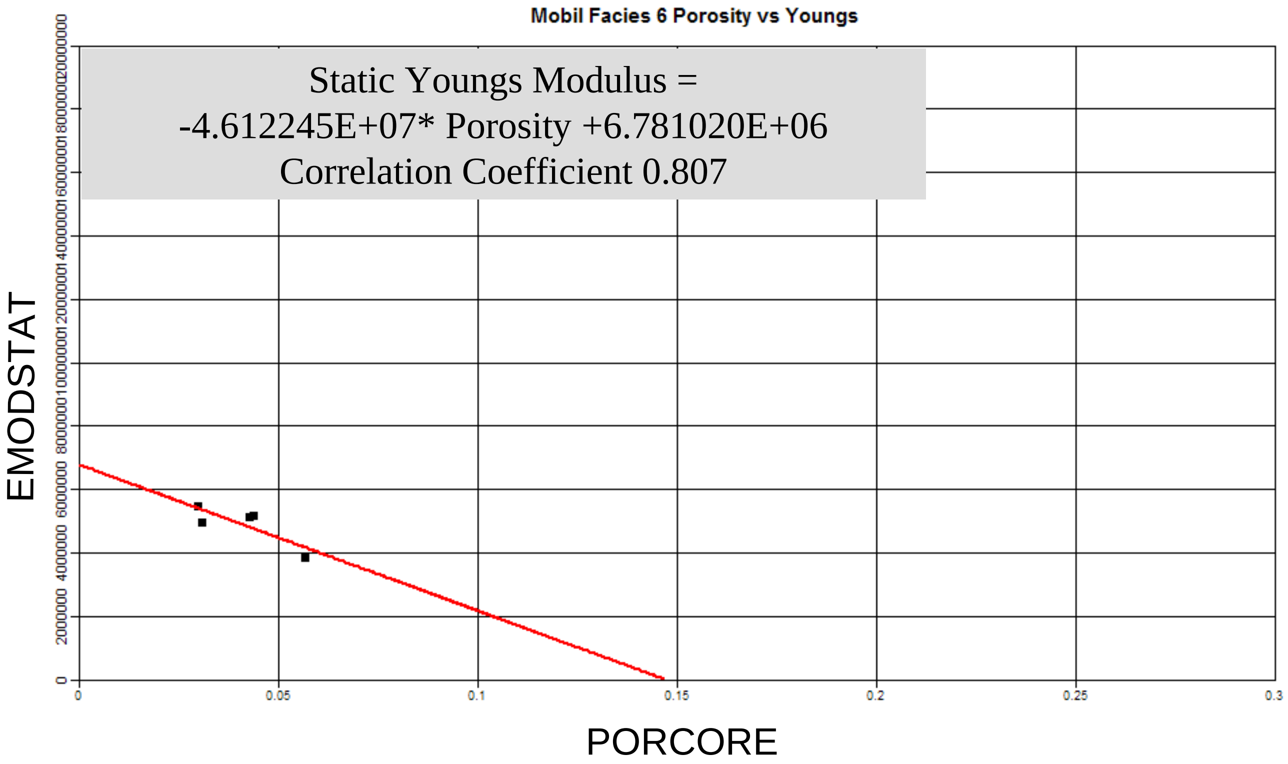

Figure 8.5.15 Porosity vs.Young's modulus (Yale and Jamieson, 1994) rock-mechanical facies 6.

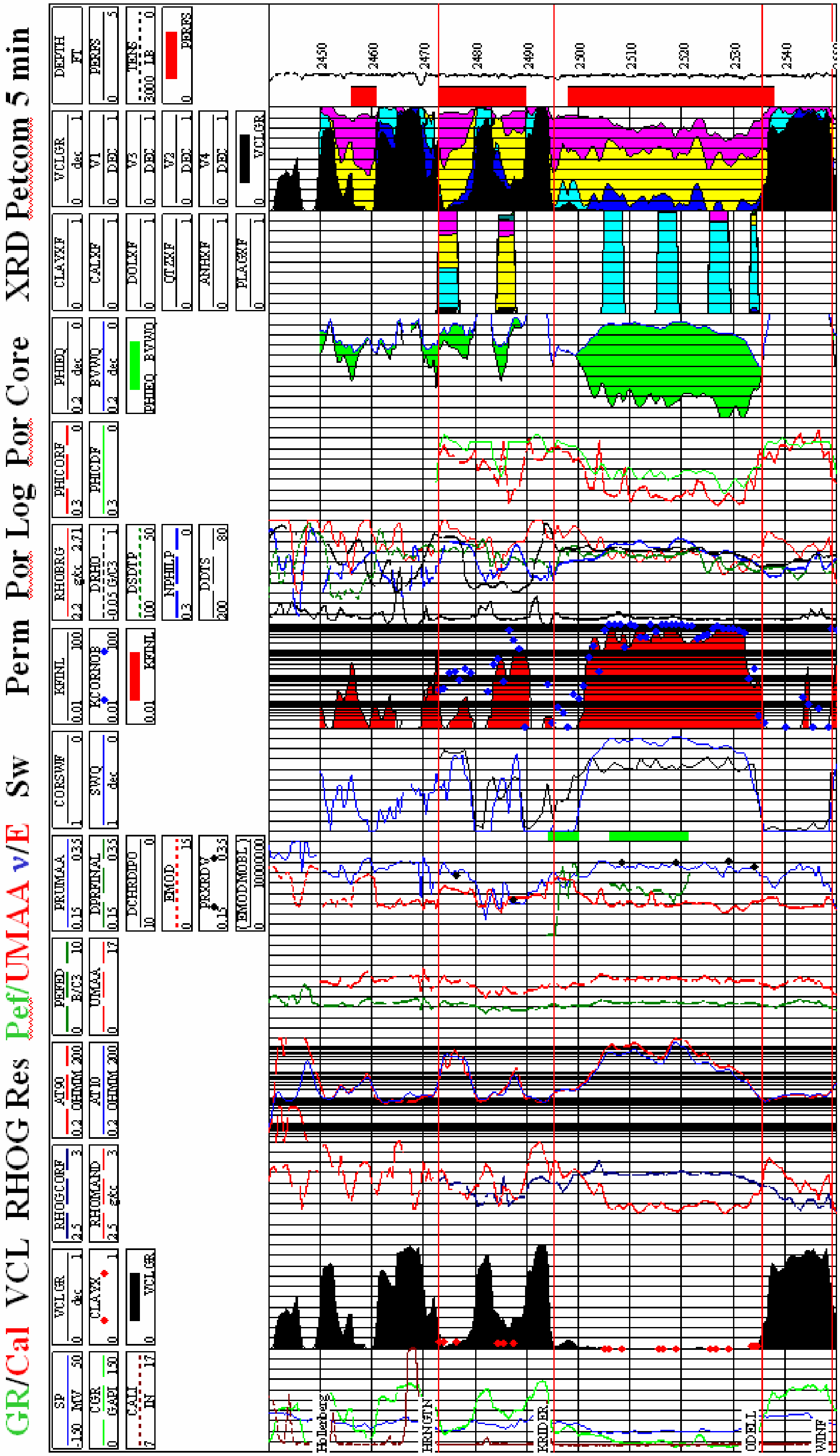

Figure 8.5.16 Plot of model properties for upper Chase Group, Flower A1 well.

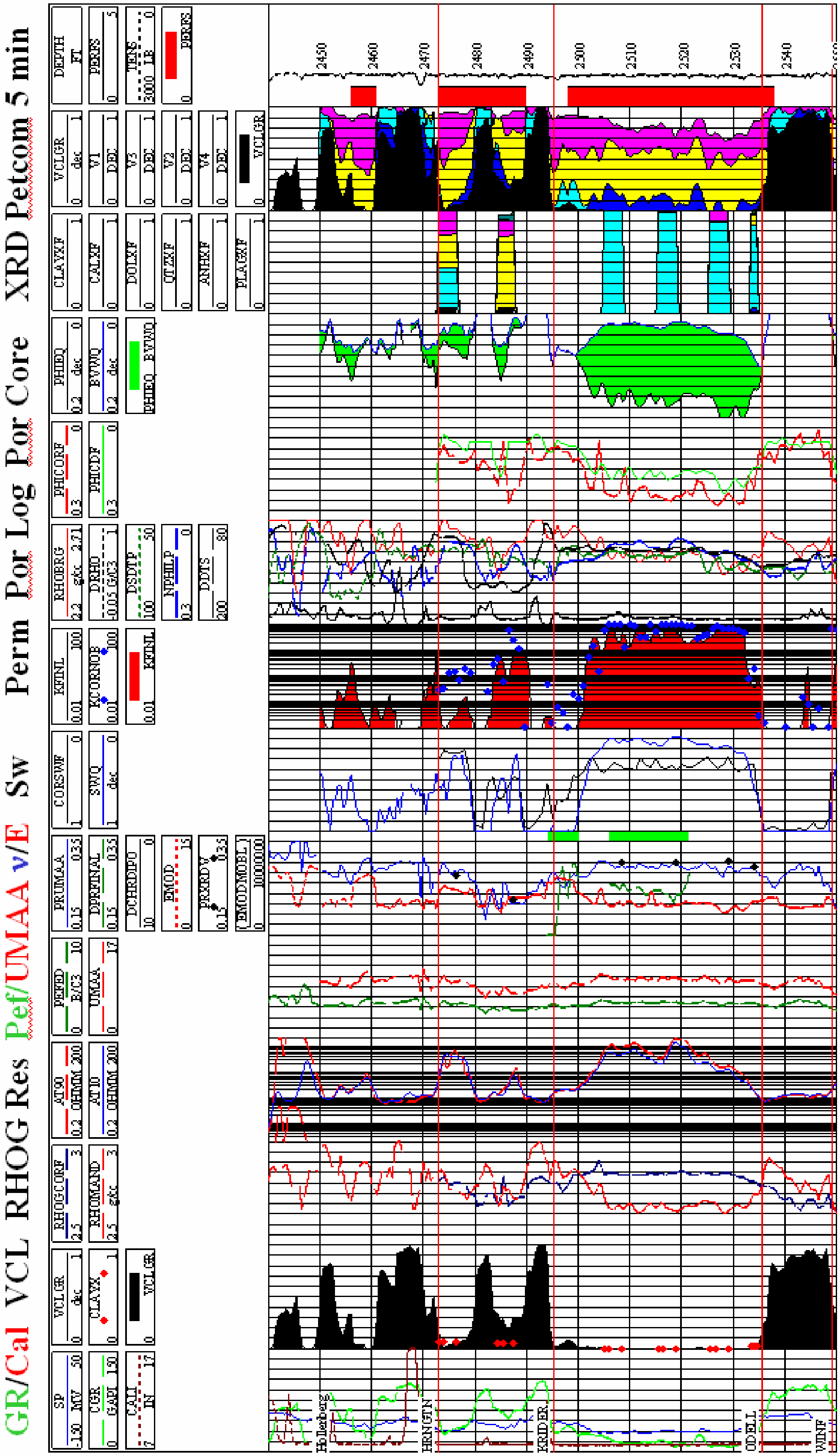

Figure 8.5.17 Plot of model properties for middle Chase Group, Flower A1 well.

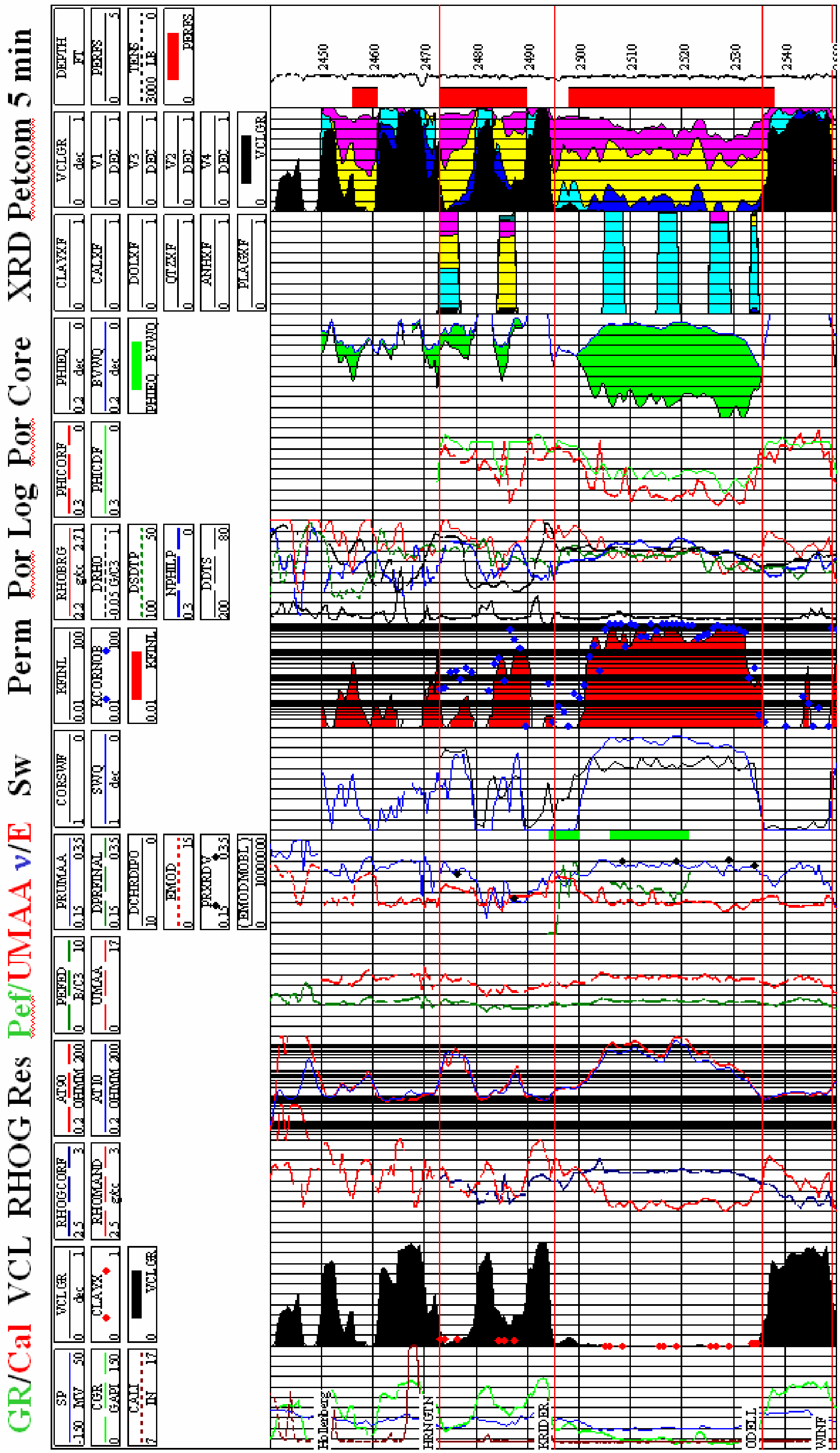

Figure 8.5.18 Plot of model properties for lower Chase Group, Flower A1 well.

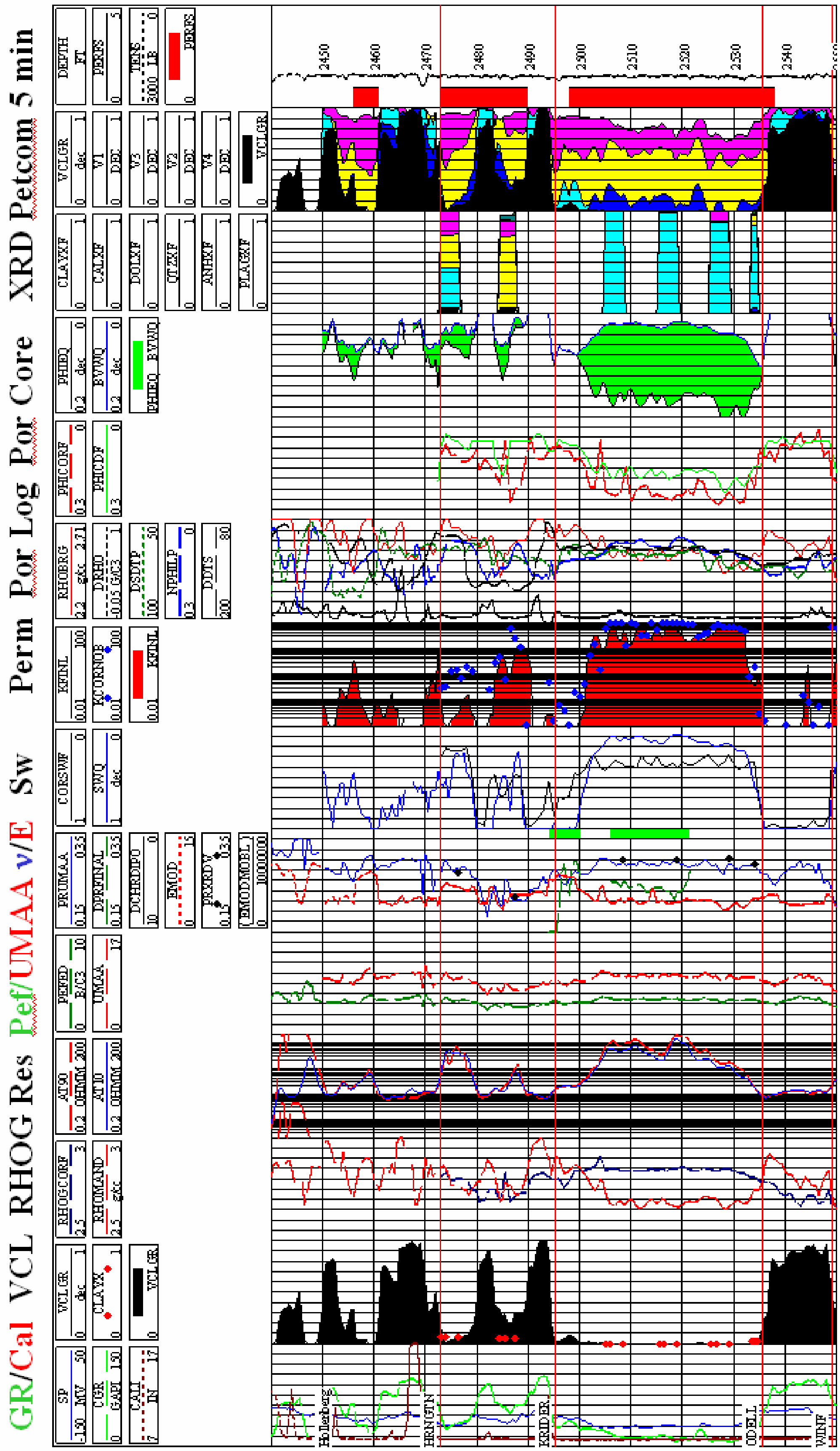

Figure 8.5.19 Plot of model properties for upper Council Grove Group, Flower A1 well.

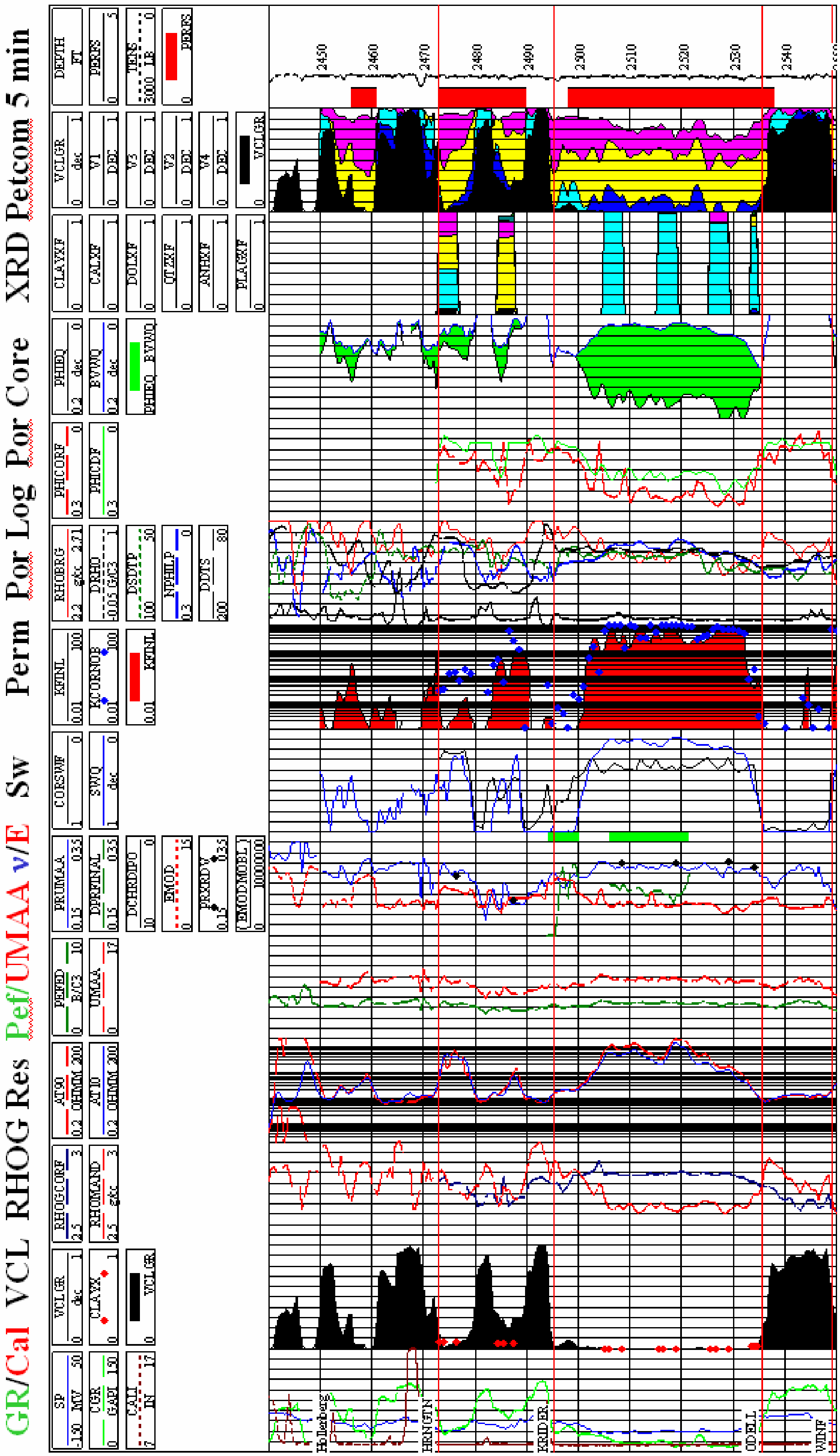

Figure 8.5.20 Plot of model properties for lower Council Grove Group, Flower A1 well.

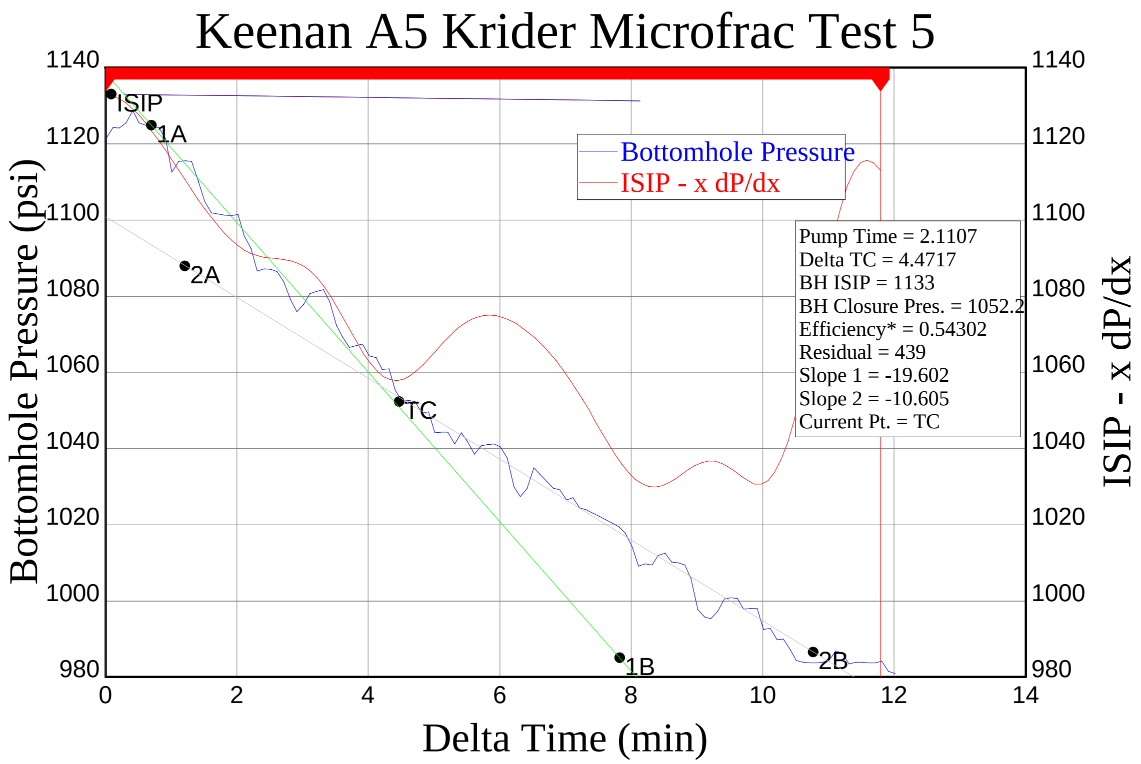

Pump Time = 2.1107
Delta TC = 4.4717
BH ISIP = 1133
BH Closure Pres. = 1052.2
Efficiency* = 0.54302
Residual = 439
Slope 1 = -19.602
Slope 2 = -10.605
Current Pt. = TC

Figure 8.5.21 Closure-analysis plot for microfrac test, rate = 8.73 bbl at 5 BPM.

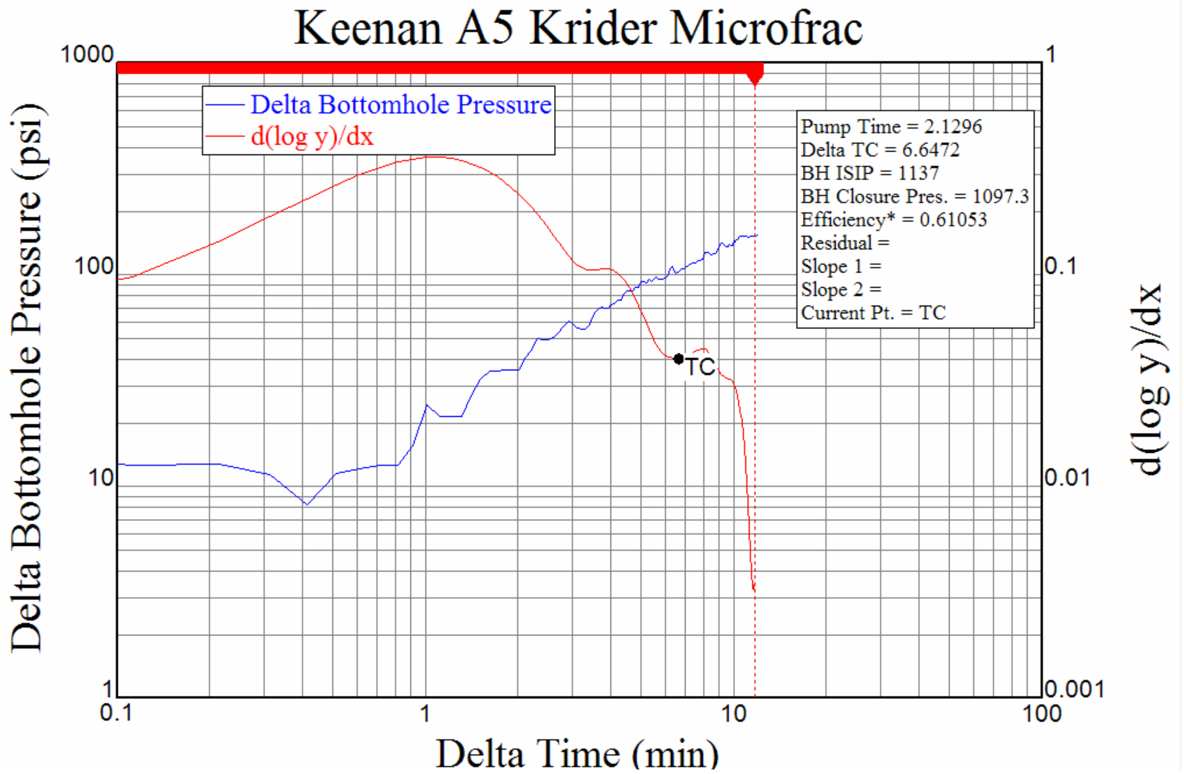

Pump Time = 2.1296
Delta TC = 6.6472
BH ISIP = 1137
BH Closure Pres. = 1097.3
Efficiency* = 0.61053
Residual =
Slope 1 =
Slope 2 =
Current Pt. = TC

Figure 8.5.22 Unit slope-wellbore storage plot. No usable data.

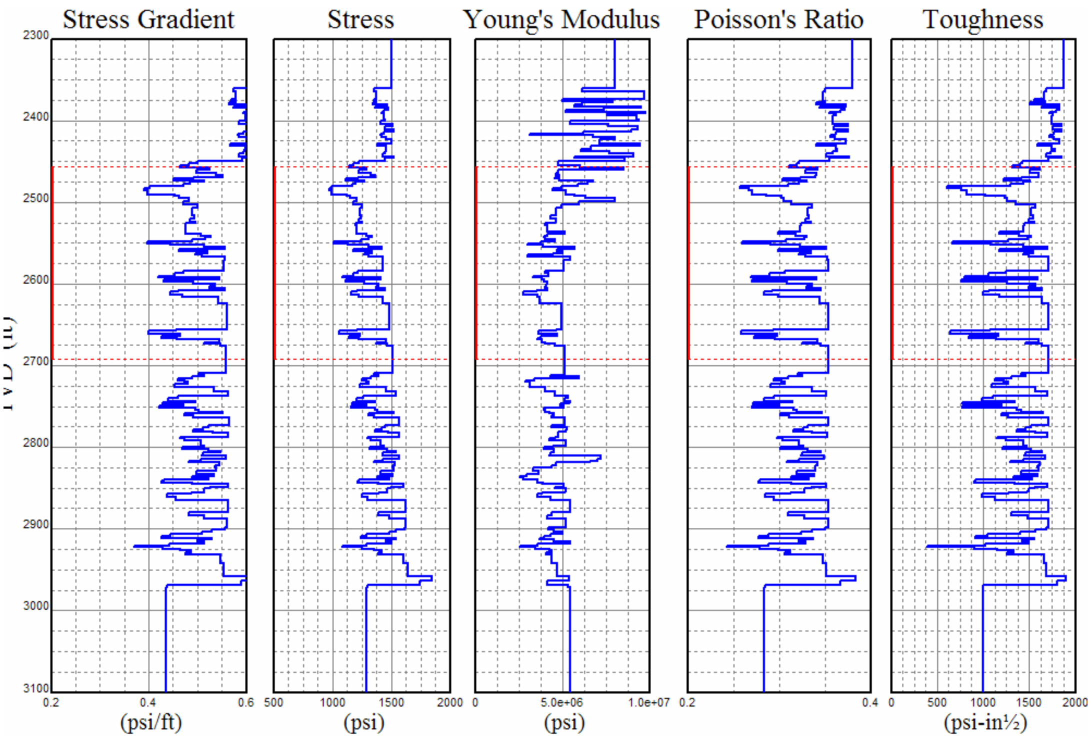

Figure 8.5.23 1960 Chase Group rock-mechanical properties

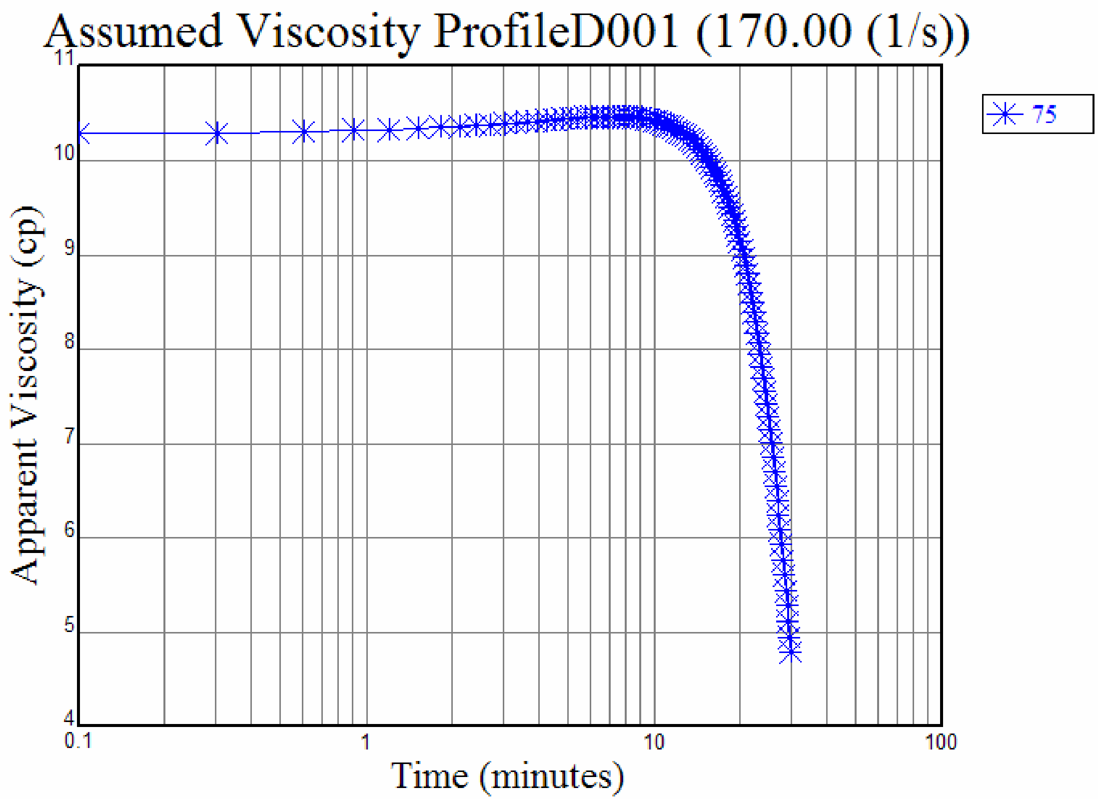

Figure 8.5.24 Fracture-simulation model fluid-viscosity profile.

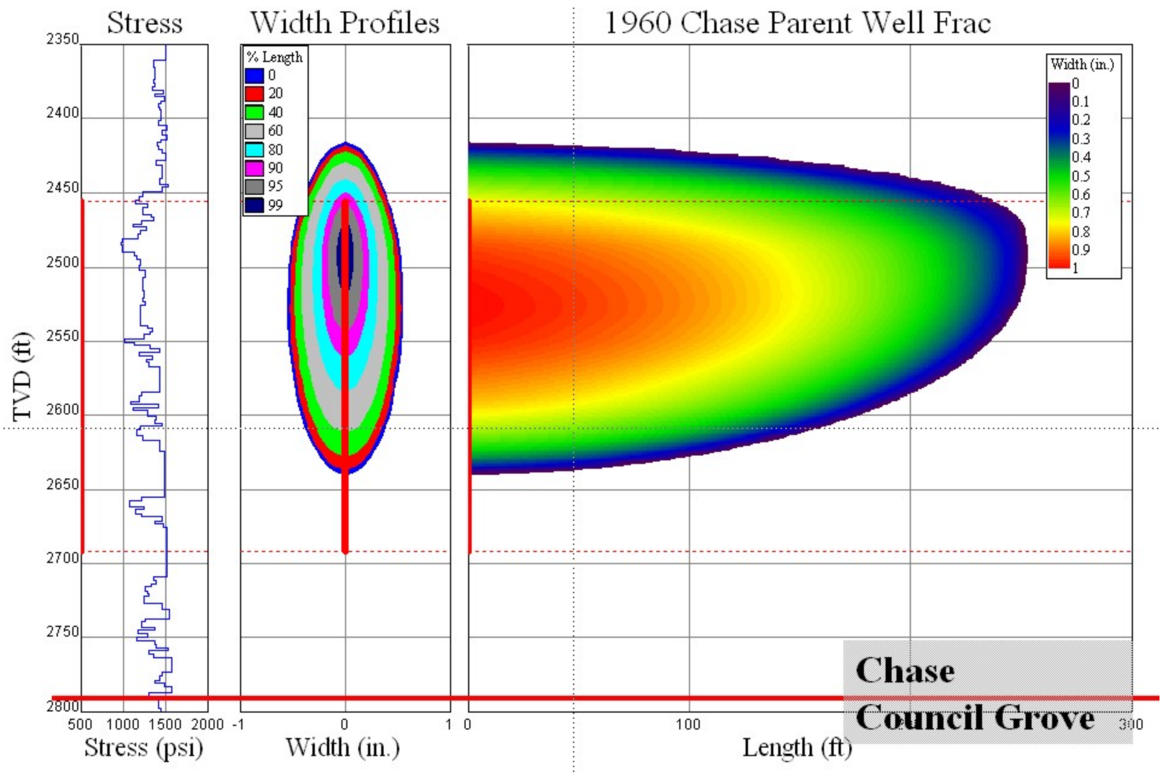

Figure 8.5.25 Simulated hydraulic-fracture dimensions, Chase parent well, rate = 150 BPM.

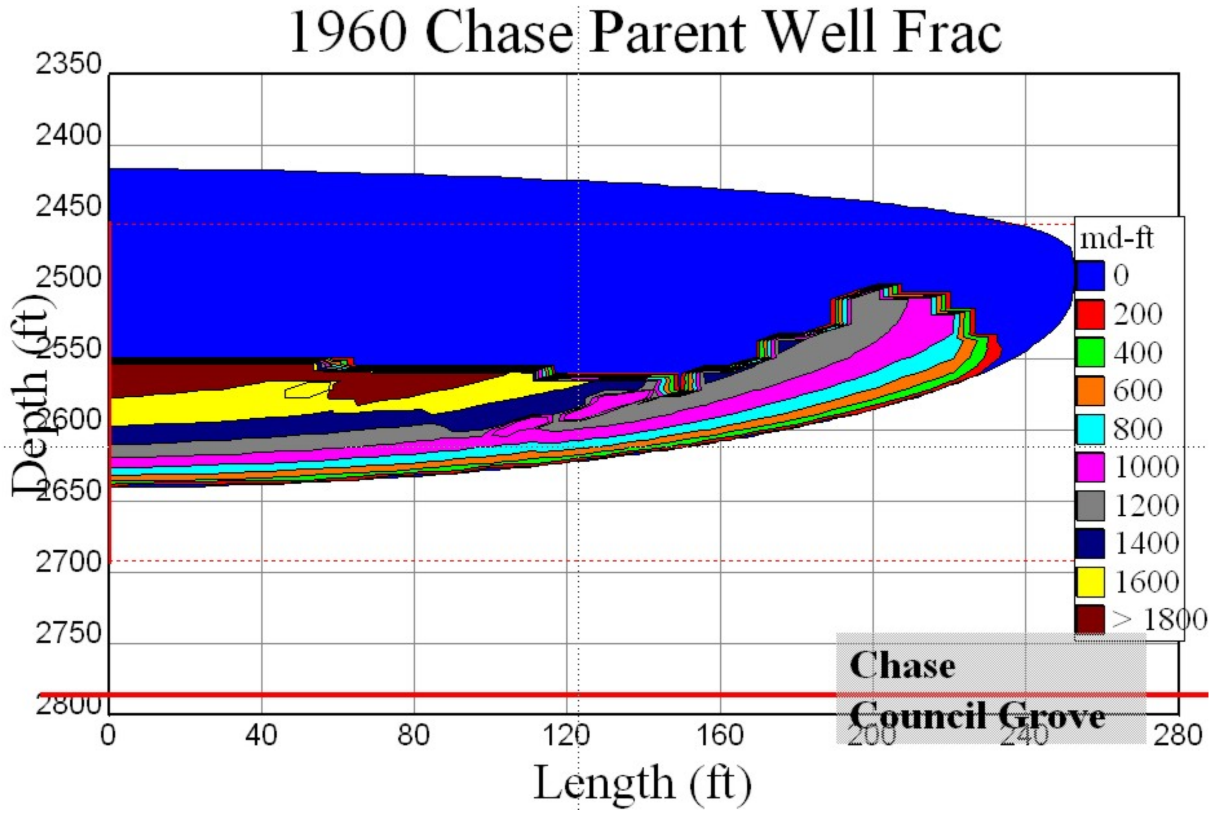

Figure 8.5.26 Simulated hydraulic-fracture permeability, Chase parent well, rate = 150 BPM.

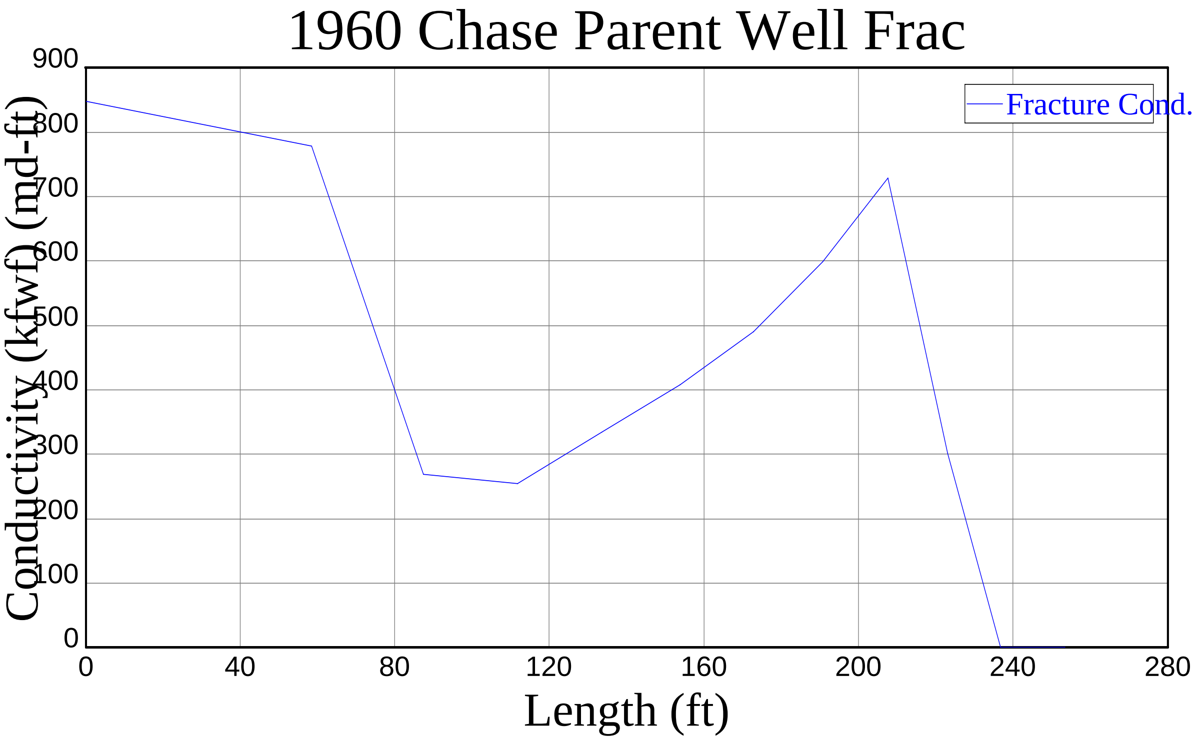

Figure 8.5.27 Simulated hydraulic-fracture conductivity, Chase parent well, rate = 150 BPM.

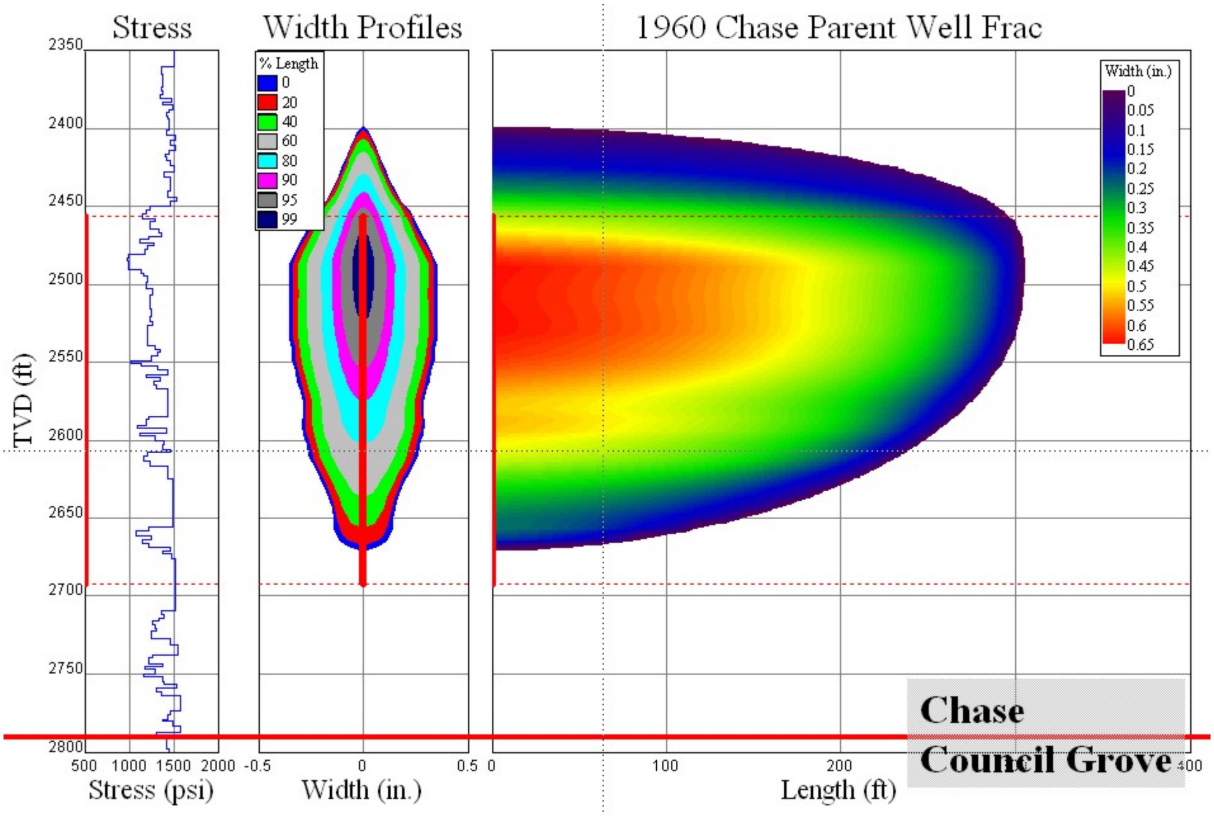

Figure 8.5.28 Simulated hydraulic-fracture dimensions, Chase parent well, rate = 300 BPM.

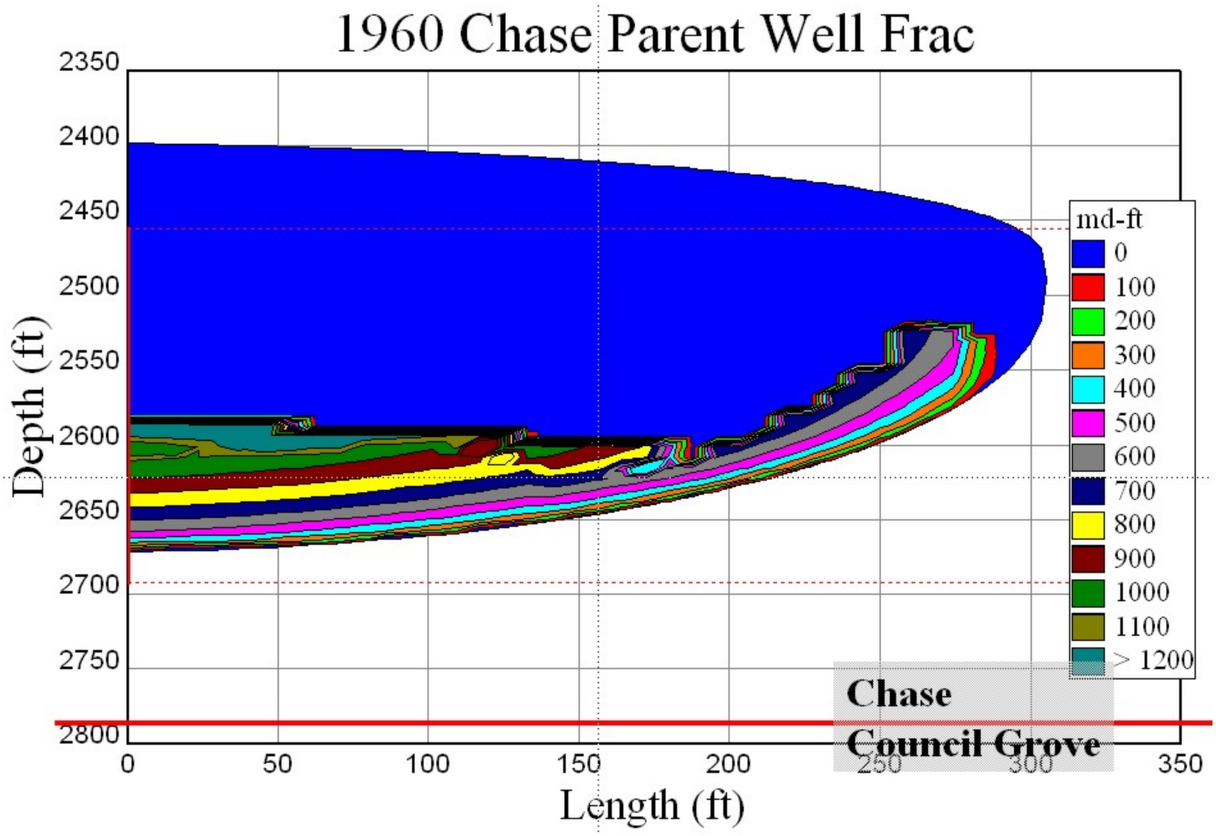

Figure 8.5.29 Simulated hydraulic-fracture permeability, Chase parent well, rate = 300 BPM.

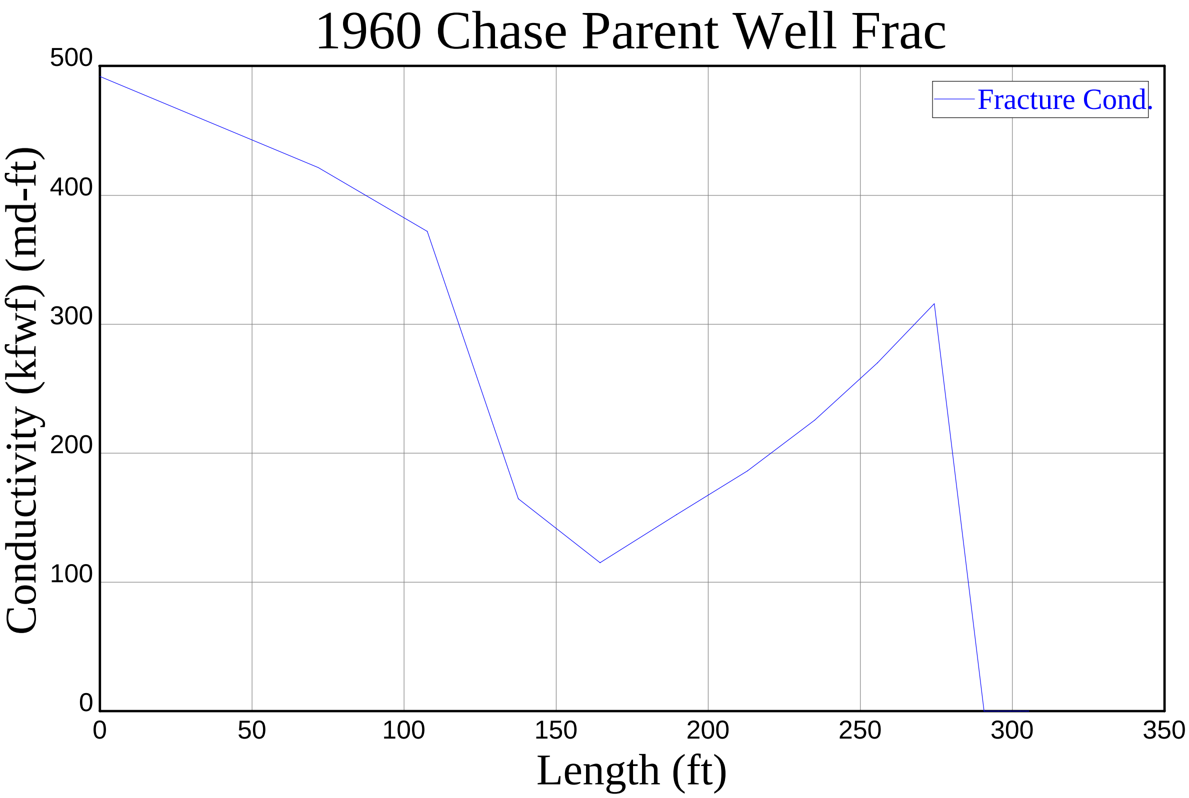

Figure 8.5.30 Simulated hydraulic-fracture conductivity, Chase parent well, rate = 300 BPM.

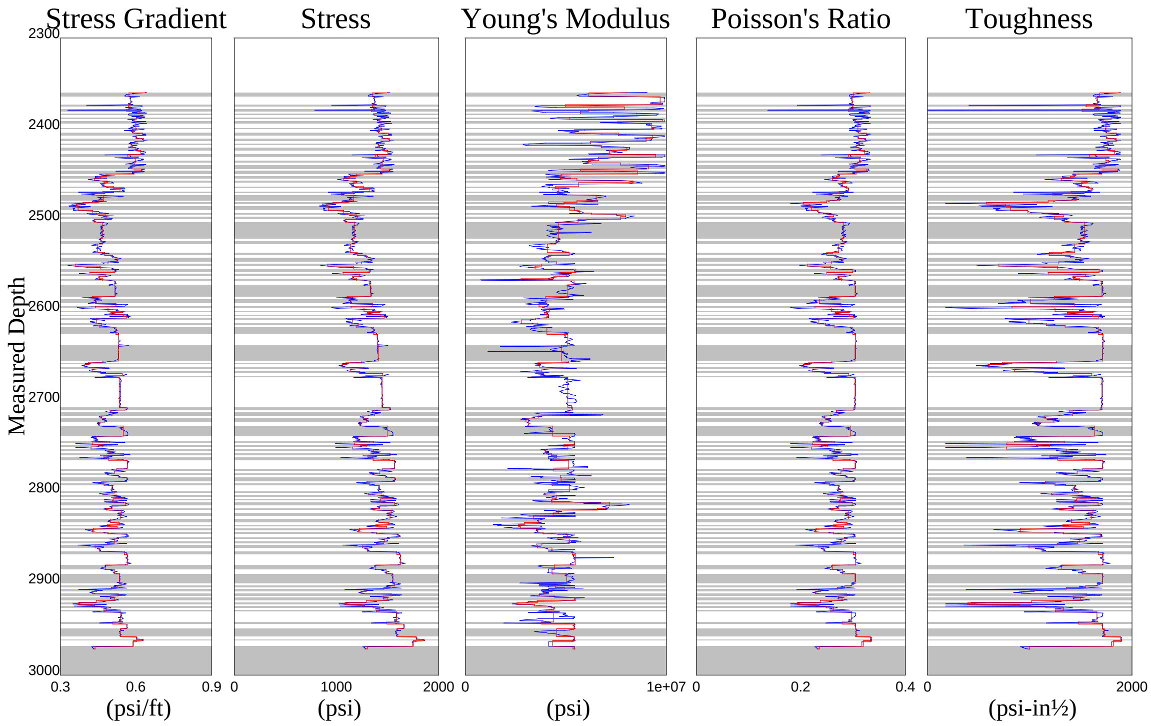

Figure 8.5.31 Static mechanical-properties plot, Chase parent well, 1960.

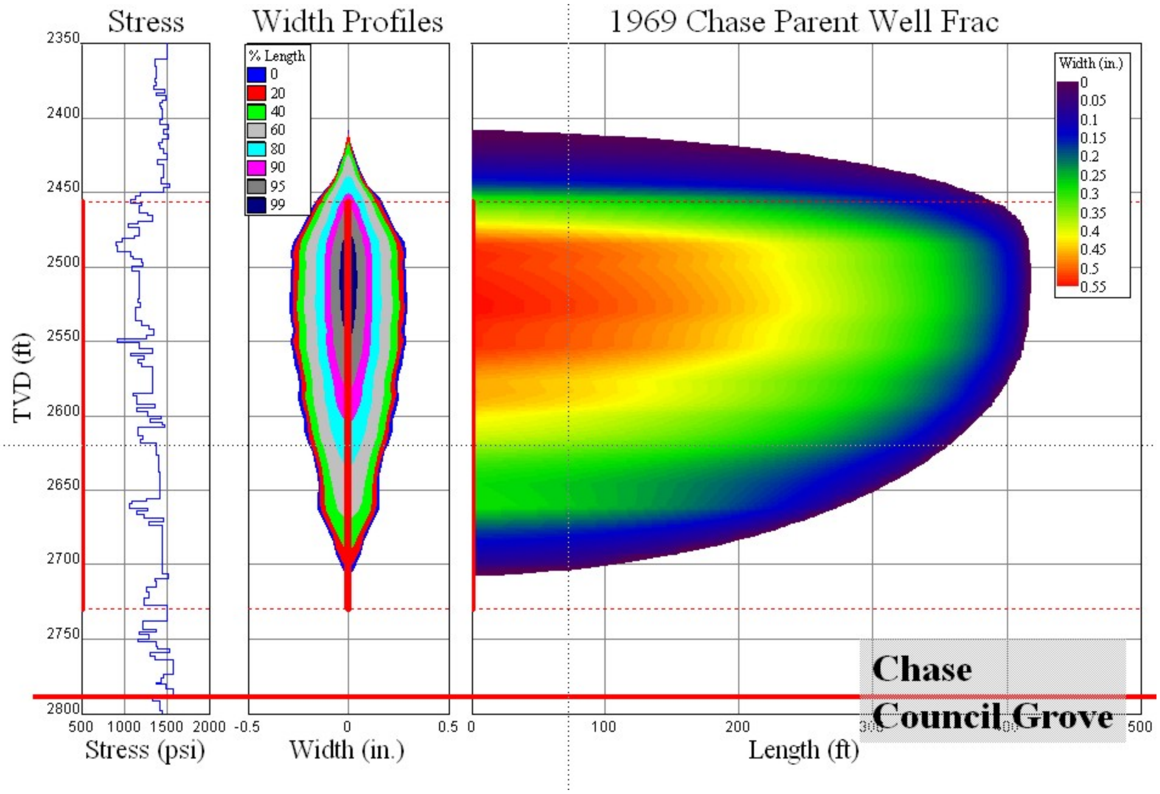

Figure 8.5.32 Simulated hydraulic-fracture dimensions, Chase parent well (1969), rate = 300 BPM.

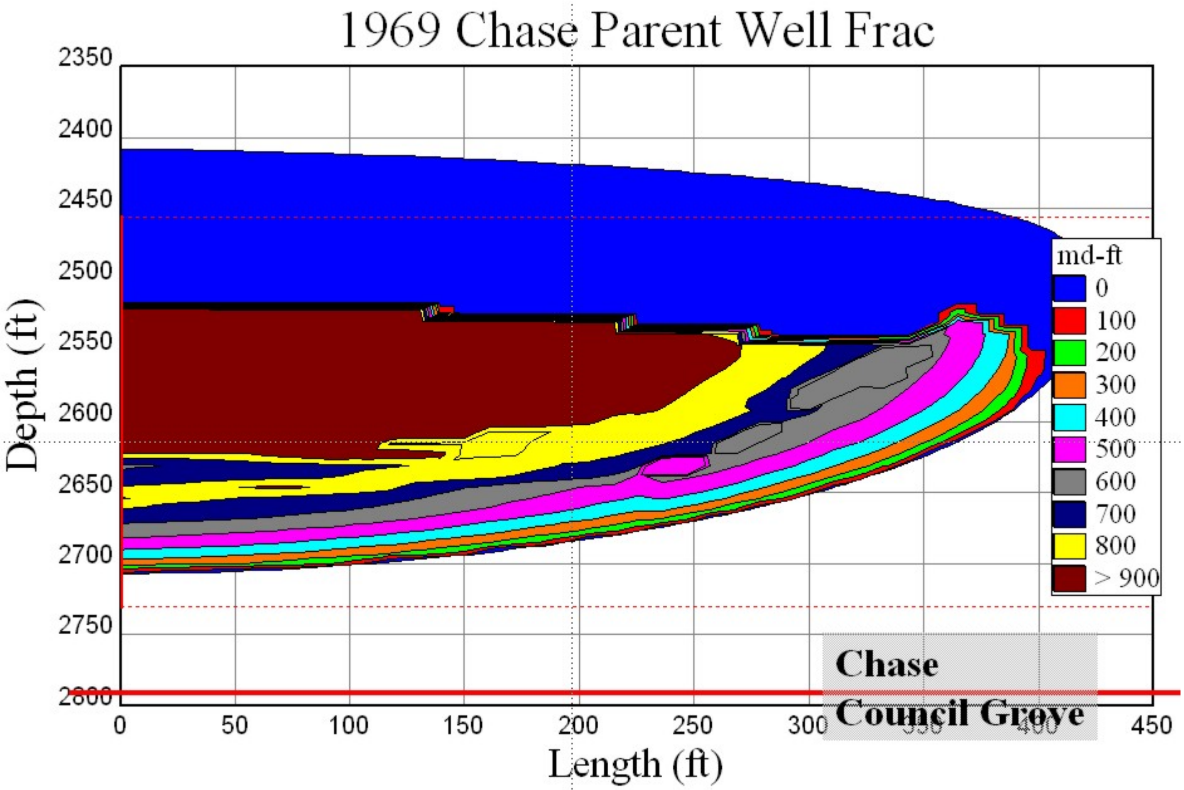

Figure 8.5.33 Simulated hydraulic-fracture permeability, Chase parent well (1969), rate = 300 BPM.

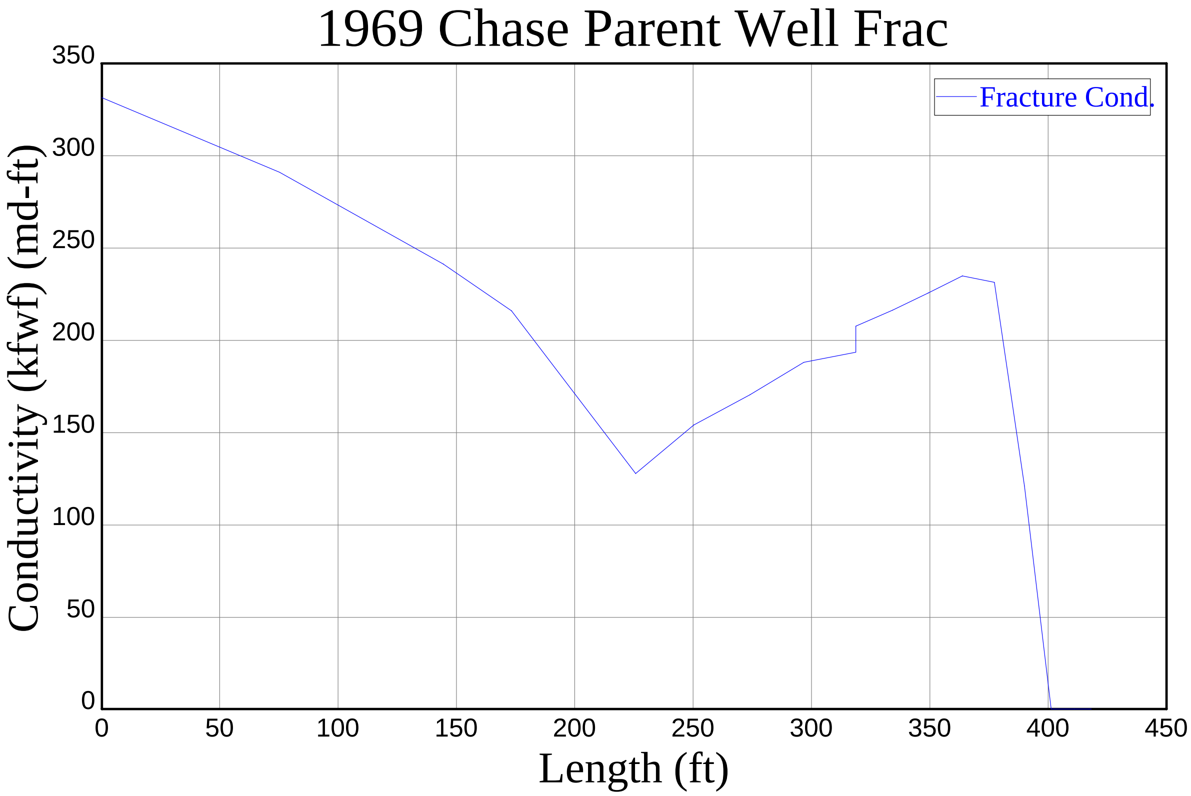

Figure 8.5.34 Simulated hydraulic-fracture conductivity, Chase parent well (1969), rate = 300 BPM.

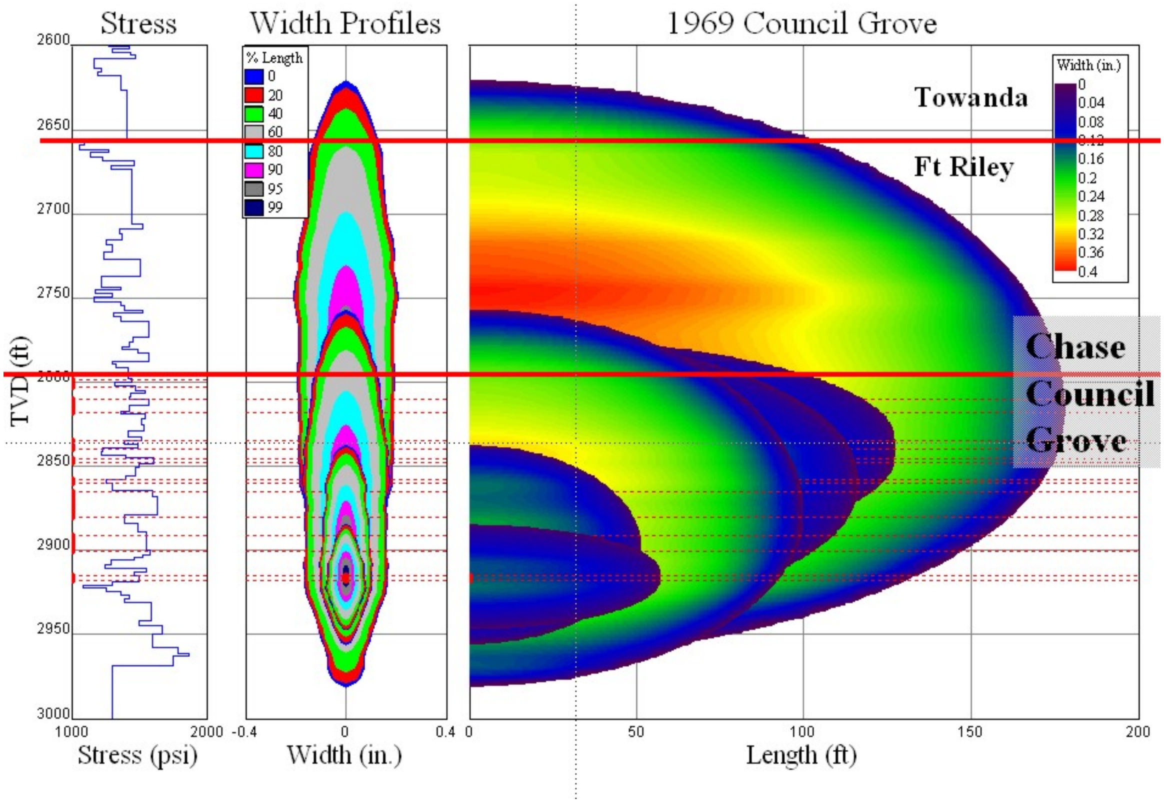

Figure 8.5.35 Simulated hydraulic-fracture dimensions, Council Grove (1969), rate = 162 BPM.

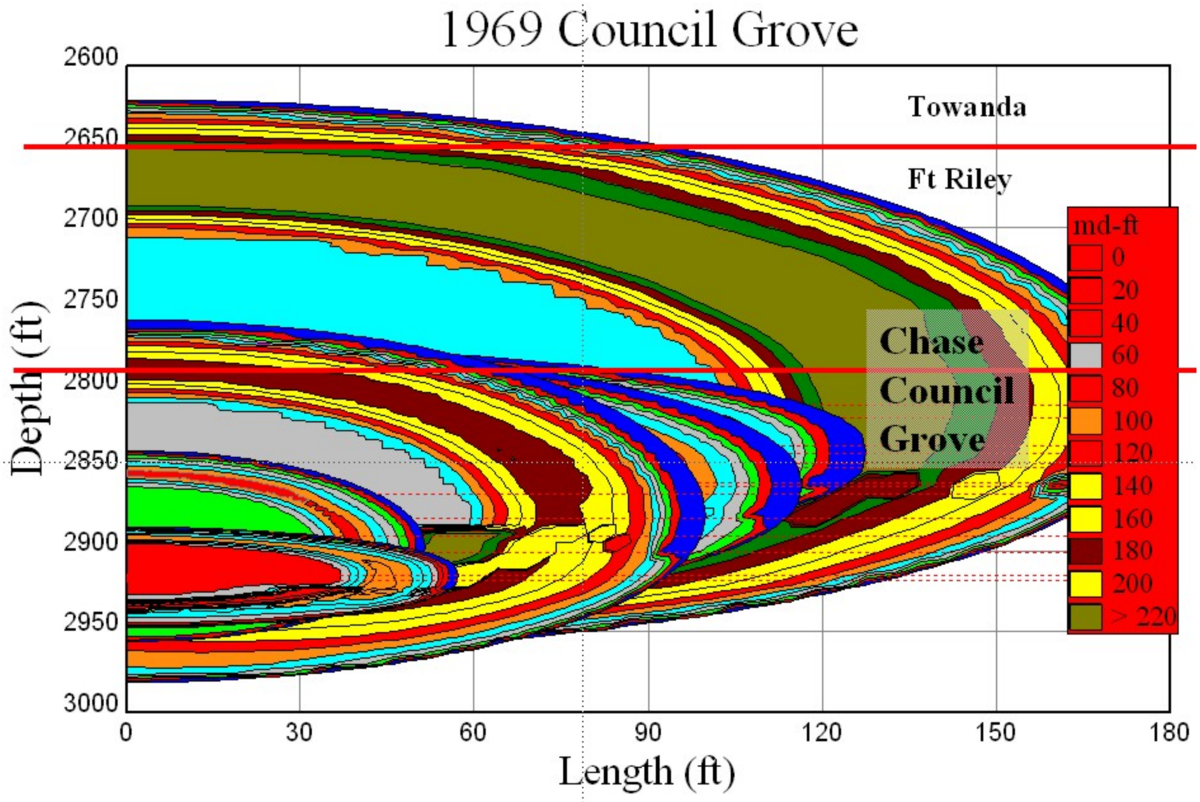

Figure 8.5.36 Simulated hydraulic-fracture permeability, Council Grove (1969), rate = 162 BPM.

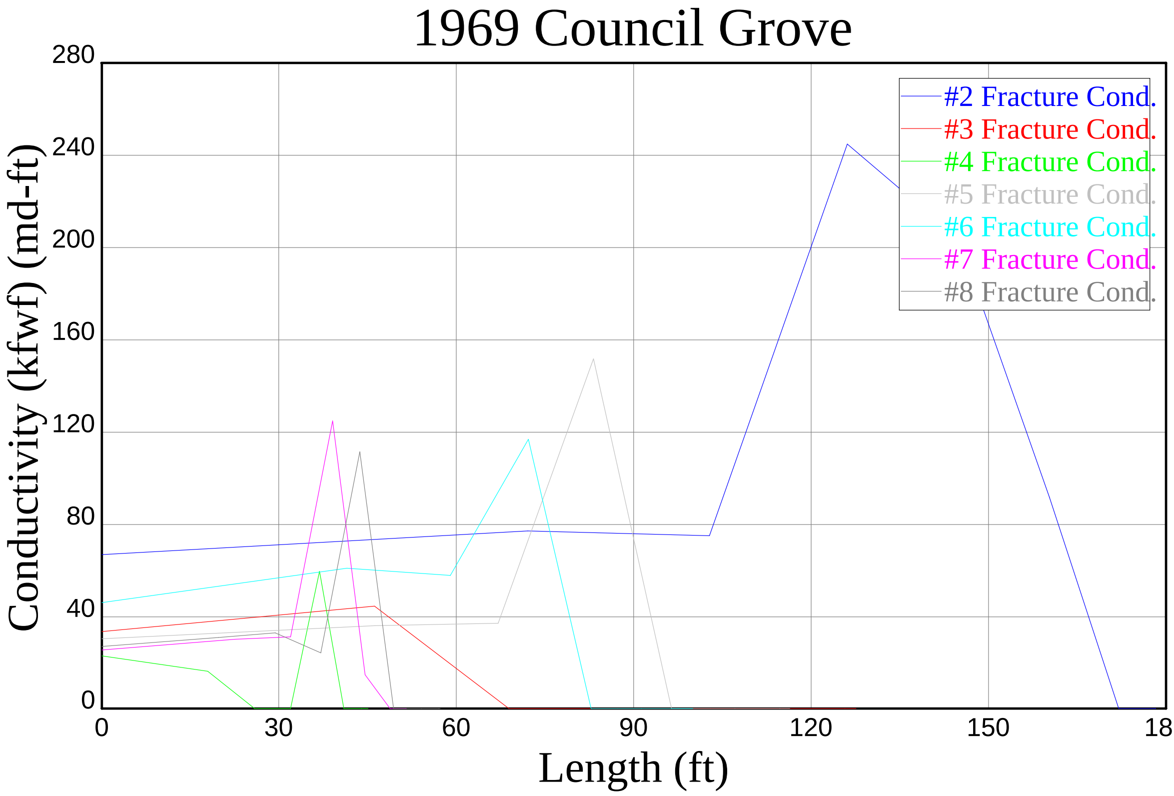

Figure 8.5.37 Simulated hydraulic-fracture conductivity, Council Grove (1969), rate = 162 BPM.

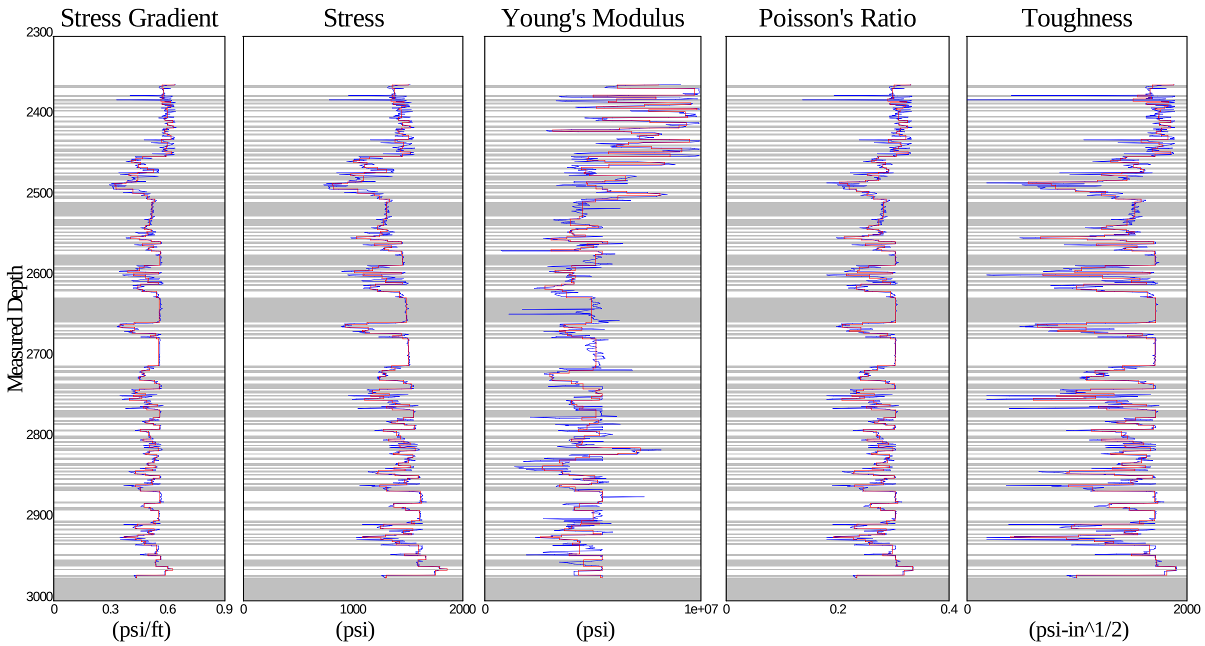

Figure 8.5.38 Static mechanical-properties plot, Chase infill well (1969).

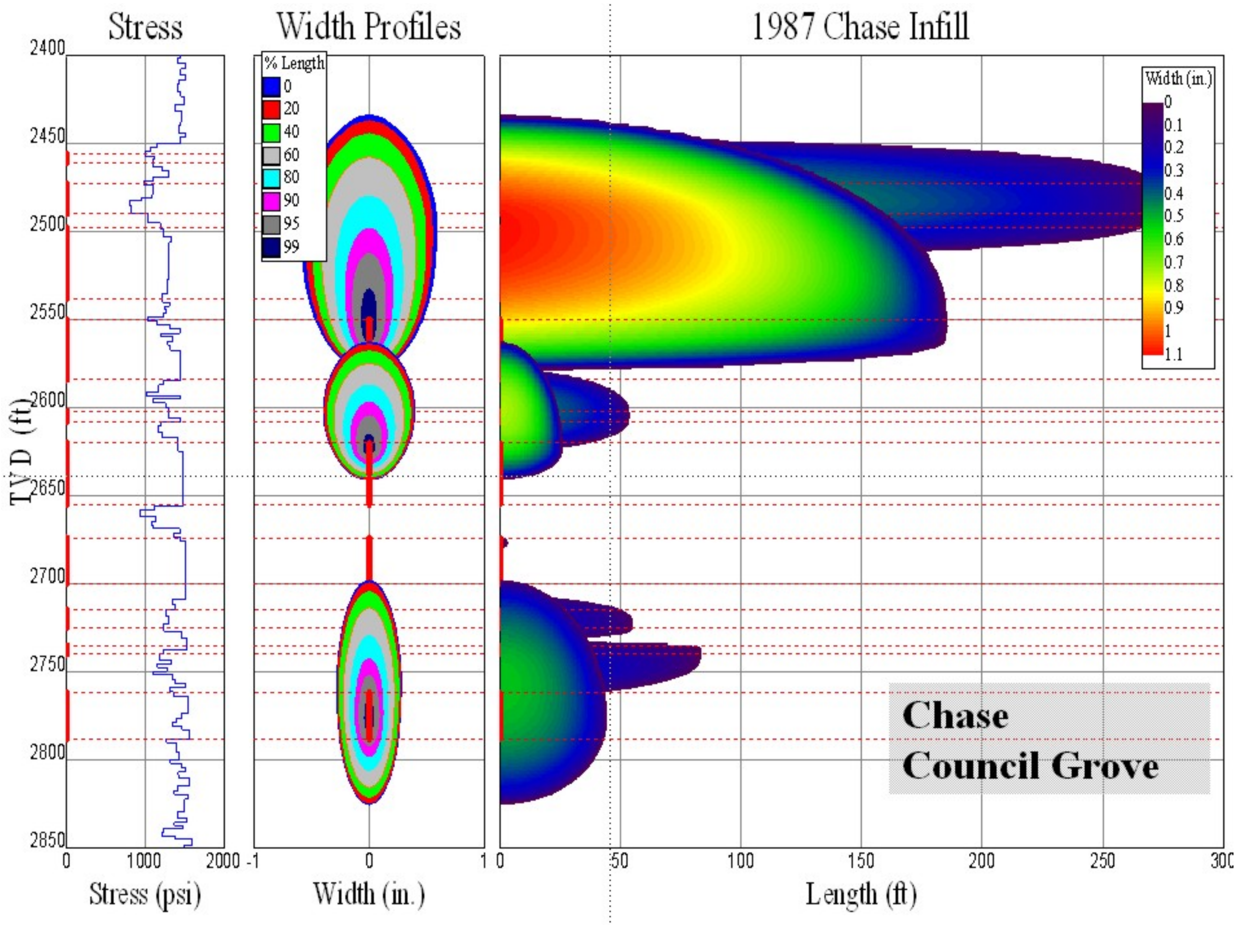

Figure 8.5.39 Simulated hydraulic-fracture dimensions, Chase infill (1987), rate = 60 BPM.

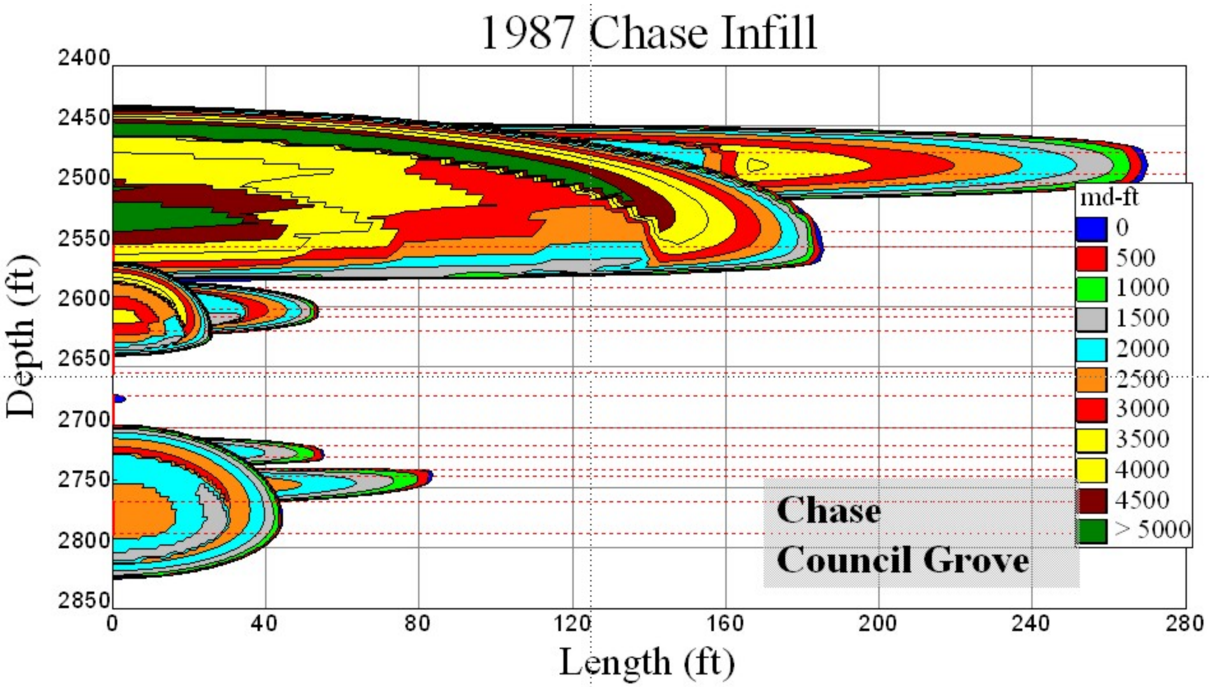

Figure 8.5.40 Simulated hydraulic-fracture permeability, Chase infill (1987), rate = 60 BPM.

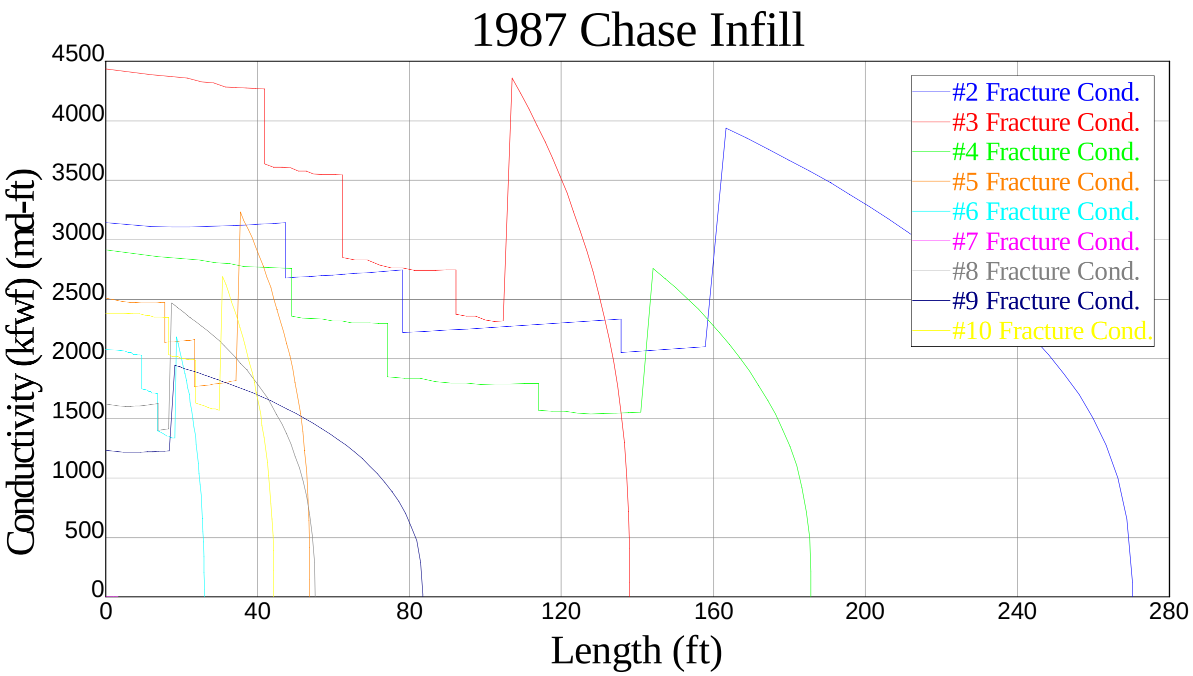

Figure 8.5.41 Simulated hydraulic-fracture conductivity, Chase infill (1987), rate = 60 BPM.